Ore Geology Reviews 186 (2025) 106892

Contents lists available at ScienceDirect

Ore Geology Reviews

journal homepage: www.elsevier.com/locate/oregeorev

Shear-zone related gold mineralisation in silicified *meta*-sediments: The Paleoproterozoic Overman deposit (Guiana Shield, Suriname)

Nicole M.E. Kioe-A-Sen [a,b,*], Manfred J. van Bergen [b], Gilian Alimoenadi [c], Leo M. Kriegsman [b,d], Helen E. King [b]

[a] *Department of Geosciences, Anton de Kom University of Suriname, Suriname*
[b] *Department of Earth Sciences, Utrecht University, the Netherlands*
[c] *Rosebel Goldmines N.V., Paramaribo, Suriname*
[d] *Research & Education Division, Naturalis Biodiversity Center, Leiden, the Netherlands*

ARTICLE INFO

Keywords:
Paleoproterozoic orogenic gold deposit
Silicified *meta*-sedimentary host
Shear-related metallogenesis
Trans-Amazonian Orogeny
Marowijne Greenstone Belt
Guiana Shield
Suriname

ABSTRACT

The Overman deposit, located near the well-endowed Rosebel gold-mining district in Suriname, is hosted by the Paleoproterozoic Marowijne Greenstone Belt in the north-eastern Guiana Shield. Gold enrichment is centred in a lensoid interval of pervasively silicified rock within a sequence of strongly deformed, predominantly phyllitic *meta*-sediments of the Armina Formation, considered to be turbiditic in origin. The auriferous silica-body is closely associated with a significant unit of carbonaceous phyllites. The entire sequence experienced greenschist-facies metamorphism with peak temperatures around 500 °C and a polyphase deformation history, comprising an initial phase of tight folding followed by an episode of brittle-ductile shearing. Field relationships and microtextural evidence point to a protracted period of sulphide mineralisation during major shearing, which post-dated peak metamorphism and the silicification event. Arsenic enrichment accompanied the ore forming stage.

Zircon U-Pb dating of host sediment and a crosscutting rhyolitic dyke, in combination with the chronological framework of regional geologic events, indicates that gold mineralisation occurred late in a 2.08–2.03 Ga interval, i.e. towards the end of the D2 stage of the Trans-Amazonian orogenetic cycle. The Overman anomaly is part of a larger sediment-hosted orogenic gold corridor, which coincides with a crustal-scale shear zone, marking the location of Paleoproterozoic oblique collision between crustal blocks. Comparable post-collisional geodynamic conditions were likely instrumental for the emplacement of orogenic gold in metasediments elsewhere in the Marowijne Greenstone Belt. Conspicuous similarities with the major Paleoproterozoic gold deposits hosted by shear zones in turbidites in the Ashanti belt of Ghana are indicative of common genetic controls.

1. Introduction

Orogenic gold formation in the early Precambrian surged globally in distinct Neoarchean and Paleoproterozoic episodes, which were broadly coeval with periods of significant expansion of continental masses (Goldfarb et al., 2001). Gold mineralisation in the Guiana Shield of north-eastern South America coincided with the 2.1–1.8 Ga Paleoproterozoic interval when significant deposits formed in greenstone-sedimentary rock sequences associated with cratonic regions worldwide. Primary orogenic gold metallogenesis occurred during a stage of crustal recycling and tectonic accretion relatively late in the geodynamic evolution of the 2.26–1.98 Ga Trans-Amazonian orogeny, when oblique convergence of north-Amazonian and west-African crustal blocks is thought to have activated transcurrent tectonics at regional scale (Vanderhaeghe et al., 1998; Delor et al., 2003a,b; Milési et al., 2003). Although orogenic gold ores are dominant in the Guiana Shield, a small number of volcanogenic massive sulphide (VMS)-type and porphyry-like deposits have been documented as well (e.g., Milési et al., 2003; Guiraud et al., 2020), attesting to a considerable diversity in mineralisation styles of individual occurrences intermittently emplaced during ca. 200 Ma of Trans-Amazonian orogenic history (Tedeschi et al., 2020).

Primary orogenic gold deposits across the Guiana Shield are generally related to major shear zones (Voicu et al., 2001; Milési et al., 2003) and are hosted in a large variety of igneous and sedimentary lithologies

* Corresponding author at: Department of Geosciences, Anton de Kom University of Suriname, Suriname.
E-mail address: nicole.kioe-a-sen@uvs.edu (N.M.E. Kioe-A-Sen).

https://doi.org/10.1016/j.oregeorev.2025.106892
Received 28 November 2024; Received in revised form 10 September 2025; Accepted 11 September 2025
Available online 17 September 2025

(e.g., Voicu et al., 1999; Daoust et al., 2011; Velásquez et al., 2011; Padoan et al., 2014; Tedeschi et al. 2018a; Combes et al., 2022; Lacroix et al., 2024; Soares et al., 2025). They show a similar diversity in Suriname where major gold mining areas currently in operation target orogenic deposits hosted in metamorphic supracrustal sedimentary sequences (Rosebel district, Merian) and basaltic rocks (Saramacca), whereas other deposits also occur in intrusive bodies such as a TTG-like batholith at the Brothers Project (Daoust et al., 2011; Kioe-A-Sen et al., 2016; Combes et al., 2024) or in contiguous volcanic-sedimentary and tonalitic lithologies as in the Antino gold system (Combes et al., 2025). All of these occurrences are spatially associated with the Rhyacian Marowijne greenstone belt (Kioe-A-Sen et al., 2016; Kroonenberg et al., 2016).

From an inventory in neighbouring French Guiana, Milési et al. (2003) noted the rarity of Au-As "Ghanaian-type" deposits among mesothermal orogenic gold ores as opposed to Au-Fe-Cu deposits related to brittle fault zones or small D_2 shear-zone granitoids. Despite the overall correspondence in geological architecture and accretionary-collisional geodynamic evolution between the north-eastern domains of the Guiana Shield and the richly endowed Birimian terrains of the southern West African Craton (e.g., Milési et al., 1992; Ledru et al., 1994; Mumin et al., 1994; Feybesse et al., 2006; Grenholm et al., 2019; Masurel et al., 2022), the only potentially corresponding example identified till date is the sparsely studied Camp Caïman prospect in north-eastern French Guiana (Milési et al., 2003; Bardoux et al., 2018).

This study presents an integrated overview of the geological setting, timing and conditions of gold mineralisation at the Overman prospect in Suriname, inferred here to be a shear-related deposit with genetic relationships to the nearby Rosebel-Saramacca and Merian mining areas (proven and probable reserves: 3–4 Moz each; Iamgold Corporation, 2022; Newmont, 2024). The results fit into a metallogenic scenario consistent with classical models for orogenic gold deposition in an

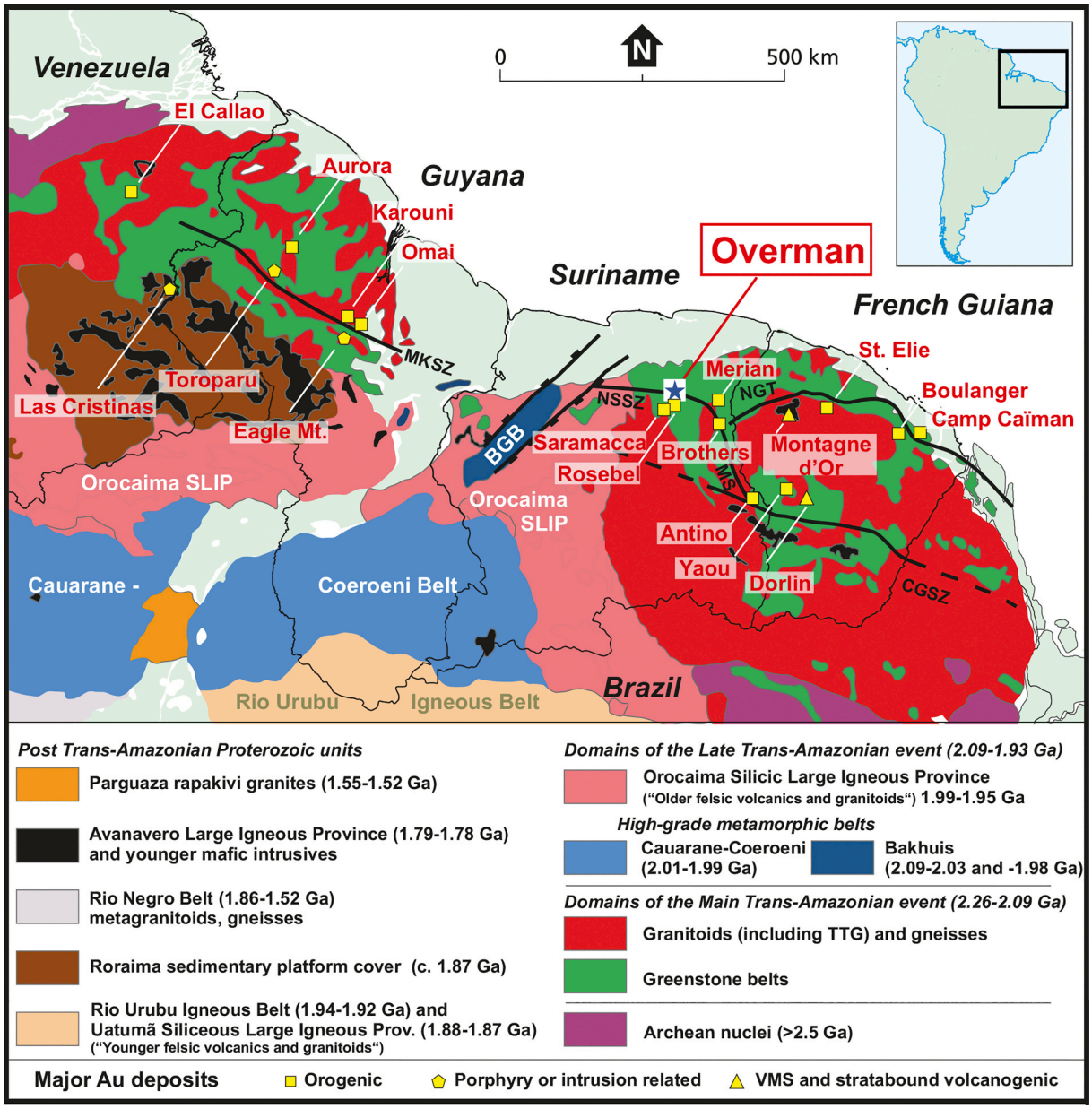

Fig. 1. Geological sketch map of the north-eastern part of the Guiana Shield showing the location of the Overman study area (blue star) and major gold deposits (modified after Kroonenberg et al., 2016; Tedeschi et al., 2018a; Guiraud et al., 2020). Abbreviations: BGB = Bakhuis Granulite Belt, CGSZ = Central Guiana Shear Zone, NSSZ = Northern Suriname Shear Zone; MKSZ = Makapa-Kuribrong Shear Zone, NGT = Northern Guiana Trough, MS = Marowijne Splay, TTG = Tonalite-Trondhjemite-Granodiorite, VMS = Volcanogenic Massive Sulphide.

accretionary-collisional setting. The local findings in combination with the regional framework suggests conspicuous similarities with Au-As deposits in the Ashanti gold belt in Ghana. These refer to the lithological character of the host sequence and affinity with As-rich sulphides, emplacement conditions and timing late in the tectono-metamorphic cycle of an orogenic belt, as well as a protracted deformation-controlled mineralisation history involving remobilisation of the gold.

2. Geological setting

.

2.1. Regional geological framework

The Guiana Shield covers an area of more than 900,000 km^2 between the Orinoco and Amazon rivers in north-eastern South America. Its present configuration was primarily shaped by a series of Proterozoic geodynamic events in a period when it formed a continuous crustal domain with the Man-Leo Shield of the (present-day) southern West African Craton (Ledru et al., 1994; Nomade et al., 2003; Johansson, 2009; Neves, 2011; Grenholm et al., 2019). Most of the rocks are Paleoproterozoic low-grade volcanic-sedimentary greenstones and granitoids, largely formed during the Trans-Amazonian orogeny. Remnants of Archean continental blocks have been identified on the western and eastern edges (Fig. 1). A wide granite-greenstone belt extends roughly parallel to the Atlantic coast from Venezuela to north-eastern Brazil. Voluminous granitoid intrusive complexes are surrounded by sizeable greenstone sequences. In Suriname, the greenstones constitute a virtually single territorial domain, which separates eastward into a northern and southern branch in French Guiana. The belt is interrupted by the NE-SW running Bakhuis horst, a prominent structural feature in western Suriname.

Four main episodes have been distinguished in the shield's geological evolution, broadly built on field-based research in the eastern part (Ledru et al., 1991; Milési et al., 1995; Vanderhaeghe et al., 1998; Delor et al., 2003a,b): *(1) Archean basement formation; (2) A main Trans-Amazonian stage* (Rhyacian; 2.26–2.08 Ga) marked by initial formation of juvenile oceanic crust, subsequent intrusion of tonalite-trondhjemite-granodiorite (TTG) and other granitoids in an arc-type setting. The first of two distinct tectono-metamorphic events (D_1 at 2.18–2.13 Ga) has been associated with collision of the North Amazonian and West African cratonic blocks upon south-verging subduction that was accompanied by the formation of the volcano-sedimentary greenstone belt in a volcanic-arc environment and by pulses of TTG intrusions. The second (D_2 at 2.11–2.05 Ga) is thought to have coincided with a period of crustal thickening, regional greenschist metamorphism and folding into synclines. It presumably followed a change from orthogonal N-S to oblique NE-SW convergence, resulting in sinistral shear, expressed as a branching system of major regional shear zones (e.g., the North Suriname Shear Zone, Fig. 1). These wrench-fault tectonics would have facilitated the opening of pull-apart basins, which were filled with a series of detrital sediments (Upper Detrital Unit, equivalent to the Rosebel Formation in Suriname). Simultaneous intrusion of a granitic suite and local migmatisation of greenstone and TTG further characterise the early part (2.11–2.08 Ga) of this D_2 event (referred to as D_{2a} by Delor et al., 2003a,b).

(3) A Late Trans-Amazonian stage (Late Rhyacian to Orosirian; 2.07–1.93 Ga), which, in the scheme of Delor et al. (2003b), started with an interval (D_{2b}; 2.07–2.05 Ga) when continuing oblique plate convergence was accommodated by dextral strike-slip movement along WNW-ESE trending corridors as inferred in northern French Guiana. Accompanying closure of the pull-apart basins, concurrent emplacement of monzogranitic intrusions and low-grade metamorphism of the detrital sediment package further mark this event. Timing of the D_{2b} interval falls within the first period of ultrahigh-temperature (UHT) metamorphism in the Bakhuis granulite belt (2.09–2.03 Ga; Klaver et al., 2015a; De Roever et al., 2019), where *meta*-pelitic granulites record peak temperatures in excess of 1000 °C and a pressure of ca. 0.9–1.1 GPa (De Roever et al., 2023; Nanne et al., 2020).

A counterclockwise P-T path has been inferred for metamorphism both in the Bakhuis granulites and in the lower-grade greenstone *meta*-sediments of northern French Guiana (Vanderhaeghe et al., 1998; De Roever et al., 2003). Delor et al. (2003a) attributed this metamorphic evolution to crustal thinning and mantle upwelling, enhanced by sinistral shearing, which would have produced an anomalously high thermal gradient and intrusive activity of the granitoids, followed by isobaric cooling at a continent-wide scale. Recent studies of the Bakhuis Belt prefer a model whereby UHT metamorphism was caused by asthenospheric heat advection, following collision with the passive West African continental margin, tearing or breakoff of the subducted oceanic slab, and removal of the continental lithosphere from the overriding Guiana plate (Klaver et al., 2015a; Beunk et al., 2021).

Different views have been proposed as to whether the Bakhuis granulites share a common genetic history with other high-grade belts further to the south (Gibbs and Barron, 1993; Delor et al., 2003b; Fraga et al., 2008; Kroonenberg et al., 2016). A zone of early Orosirian amphibolite to granulite facies metamorphic supracrustal rocks (Cauarane-Coeroeni Belt – CCB; Fraga et al., 2009, 2024), encompassing the Coeroeni Gneiss Belt in SW Suriname, the adjacent Kanuku Group in southern Guyana and the Cauarane Group further to the west in the Roraima State of Brazil, separates the northern Rhyacian units from the Late Rhyacian – Orosirian igneous domains further south in the Guiana Shield. Available zircon ages from CCB gneisses and migmatites show various populations between 2.98 and 1.92 Ga with ambiguous interpretations (Santos et al., 2003; De Roever et al., 2015; Kroonenberg et al., 2016; Fraga et al., 2017; Fraga and Cordani, 2019). The main high-grade metamorphic event presumably occurred between 2025 and 2000 Ma and thus post-dates UHT metamorphism of the Bakhuis granulites, which argues against a common evolution of these belts (Fraga et al., 2024). These authors attributed the tectono-metamorphic CCB event to basin closure during accretion of magmatic arcs onto older crustal blocks and envisaged this "Akawai Orogeny" to represent a second collisional phase late in the Trans-Amazonian cycle. Subsequent perturbations associated with massive igneous activity in the neighbouring Rio Urubu – Uatumã and Orocaima domains were probably responsible for younger zircon ages. Earlier hypotheses related the CCB to active subduction in an orogenic setting (Santos et al., 2003) or to intracontinental rift-type basin formation (Kroonenberg et al., 2016).

Felsic to intermediate *meta*-volcanics of the Dalbana Formation and associated subvolcanic granites cover large parts of west and south Suriname (Bosma et al., 1983, 1984; Kroonenberg et al., 2016) as part of a continental-scale volcanic–plutonic belt extending westward via northern Brazil and Guyana to Venezuela, and variously referred to as "Older felsic volcanic and granitoïd belt" (Kroonenberg et al., 2016), Caicara-Dalbana belt (Anandbahadoer-Mahabier and De Roever, 2019), an intracontinental siliceous large igneous province (Orocaima SLIP; Reis et al., 2021) and Orocaima Igneous Belt (Fraga et al., 2024). Zircon dating yielded 1.99–1.95 Ga for ages of these igneous rocks in Suriname, which unconformably overlie folded and metamorphosed rocks of the greenstone belt, and 1.98–1.96 Ga for a second high-grade metamorphic event in the region (De Roever et al., 2015; Kroonenberg et al., 2016). These ages coincide with the emplacement of charnockite and associated mafic intrusions in the Bakhuis belt, dated at 1.99–1.98 Ga, thus significantly post-dating UHT metamorphism in this area (Klaver et al., 2015a,b).

The geodynamic setting of this latest Trans-Amazonian episode (cf. D_{2c} of Delor et al., 2003b) in the southern realm remains under discussion, in contrast to a broad consensus on the main Trans-Amazonian events in terms of southward subduction, accompanying magmatism, subsequent (partly oblique) collision of the West African passive continental margin with the northern boundary of the Guiana plate, and associated tectonic reorganisation.

(4) Post Trans-Amazonian events (Orosirian) include formation of granitoïds and orthogneisses of the Rio Urubu (Igneous) Belt (ca. 1.94–1.92 Ga; Fraga et al., 2017, 2024) and felsic volcanics and granites of the Uatumã SLIP (ca. 1.88–1.87 Ga; Reis et al., 2021), bordering the Guiana Shield in the south and collectively labelled "Younger volcanic and granitoid belt" in Fig. 1, as well as the deposition of an older platform cover (sandstones of the Paleoproterozoic Roraima Formation) and subsequent emplacement of the Avanavero mafic intrusions (Santos et al., 2003). In central-south Guyana and Suriname, the Trans-Amazonian units were intruded by Mesoproterozoic alkaline magma bodies (Gibbs and Barron, 1993), and Mesoproterozoic dykes with alkaline affinity (Käyser dolerite; De Roever et al., 2003). Mesozoic Apatoe dyke swarms, dissect the entire Guiana Shield and are associated with the onset of Phanerozoic continental breakup and opening of the Atlantic Ocean (Deckart et al., 1997; Nomade et al., 2000, 2002).

Based on a compilation of zircon ages, Kroonenberg et al. (2016) proposed a slightly modified subdivision of Trans-Amazonian orogenic stages for Suriname. The lithological units of the *Marowijne Greenstone Belt* record a first phase between 2.18 and 2.09 Ga, when initial production of juvenile crust in an oceanic environment was followed by island-arc volcanism and diapiric intrusive activity, low to medium-grade metamorphism, isoclinal folding and deposition of detrital sediments after a period of uplift and erosion. Voluminous granites and gneisses in the south-eastern quadrant of the country overlap in age with the youngest greenstone units. The timing and geological evolution of this first phase largely correspond to the D_1 and D_{2a} events of Delor et al. (2003b). Kroonenberg et al. (2016) combined the high-grade metamorphism of granulites, gneisses and pegmatites in the Bakhuis Granulite belt, with that of the Coeroeni and Kanuku rocks to represent a second phase, corresponding to the 2.07–2.05 Ga D_{2b} interval of Delor et al. (2003b). In their view, the 1.99–1.95 Ga felsic intrusive and *meta*-volcanics of west and south Suriname, together with charnockitic, gabbroic and anorthositic rocks in the Bakhuis belt define a third phase, falling within D_{2c} of Delor et al. (2003b).

2.2. Marowijne Greenstone Belt

The Marowijne Greenstone belt in the north-eastern part of Suriname is made up of metamorphosed sedimentary, volcanic and intrusive rocks that include tonalite-trondhjemite-granodiorite (TTG), granitic and (ultra-)mafic varieties. Preliminary zircon U-Pb and Pb-Pb dating provided ages roughly between 2150 and 2100 Ma for the greenstone belt rocks (see summary in Kroonenberg et al., 2016). Largely *meta*-volcanic rocks of the *Paramaka Formation* comprise basalts (locally pillow-shaped), andesites and rhyolites, together with thin layers of volcaniclastic sediments and cherts. The overlying *Armina Formation* consists of tightly folded *meta*-greywackes and phyllites, representing metamorphosed turbiditic sequences, as well as minor conglomerates, intermediate volcanic rocks and volcaniclastics (Bosma et al., 1984; Gibbs and Barron, 1993; Naipal and Kroonenberg, 2016; Kioe-A-Sen et al., 2016). Both formations are thought to be unconformably overlain by the metasedimentary *Rosebel Formation* (Bosma et al., 1983), which mainly consists of arkosic and quartz-rich sandstones, siltstones, conglomerates and minor amounts of volcanic rocks. Most of its terrigenous material was probably eroded from the Paramaka volcanics and deposited in a typical fluvial molasse sequence (Gibbs and Barron, 1993). All formations experienced greenschist facies and locally amphibolite facies metamorphism. Various diapiric TTG intrusions and younger biotite and muscovite granite plutons are present in the greenstone belt (Bosma et al., 1983). Migmatitic gneisses adjoin its southwestern and northern margins (Kroonenberg et al., 2016).

2.3. Overman gold deposit – Exploration history and local geology

The Overman gold deposit studied here is a prospect area in Northeast Suriname, some 80 km south of the capital city of Paramaribo. It is situated 11 km north of the Rosebel gold-mine concession, which hosts eight identified orogenic gold deposits (Fig. 2) and six mines with an average grade of 1–1.9 g/t currently in operation, and is surrounded by an additional seven exploration target areas (Iamgold Corporation, 2017). The Rosebel deposits are distributed along WNW-ESE running northern trends (Koolhoven-JZone and Pay Caro-East Pay Caro) and E-W directed central (Rosebel) and southern (Mayo-Roma-Royal Hill) trends (Fig. 2). Gold is generally associated with quartz-carbonate veins in *meta*-sediments (turbiditic sequence of the Armina Fmt, arenitic sequence of the Rosebel Fmt) and *meta*-volcanics (Paramaka Fmt), often at lithological transitions or fault contacts (Daoust et al., 2011; Daoust, 2016). In contrast, in the more recently opened Saramacca mine, 25 km south-west of the Rosebel area, gold is hosted in an extensive fault zone within mafic volcanics of the Paramaka Fmt (Beek, 2019).

Until 2011 the Overman project was referred to as the Charmagne project, being part of a concession carrying that name. In the 1950 s, when Charmagne "quartzite" was prospected and exploited for quarry stone/road split in small-scale workings by the Geological Mining Department (Geological Mining Service of Suriname, 1955), weak gold anomalies were discovered in silica-rich hills. Multiple exploration campaigns (field mapping, stream sediments, various geochemical and geophysical airborne and ground surveys, auger and diamond drilling, satellite imaging) carried out since then (Van Maastrigt, 2009a,b; Iamgold Corporation, 2017) have exposed first-order features of the deposit and its contrasting setting compared to the neighbouring deposits. The economic resource of the Overman deposit has been estimated at 248,000 oz based on a gold price of $1500/oz in 2017 (Iamgold Corporation, 2017).

The central part of the deposit is the quartz-rich Overman Hill (Fig. 3), approximately 10 m wide and 300 m long with a WNW-ESE strike (Geological Mining Service of Suriname, 1955), roughly parallel to the alignment of the northernmost Rosebel gold deposits. Standing out several tens of metres above the local topography, it is the surface expression of a larger, 10–50 m thick, 55°-70° south-dipping sheet-like rigid silica body that extends up to 3 km to the ESE (Iamgold Corporation, 2017).

This auriferous silica body forms part of a low-grade metamorphic rock sequence predominantly made up of various fine-grained sediments (mudstones, siltstones, greywackes) consistent with the turbiditic lithologies of the Armina Fmt. The entire section is intercalated in an area where steeply dipping, WNW-ESE trending *meta*-sedimentary (turbiditic) and *meta*-volcanic units alternate (Fig. 2), possibly representing repetitions of up to several kilometres thick tectonic flakes separated by thrusts (Daoust, 2016). These units are equivalent to (parts of) the Armina Fmt and the unconformly underlying Paramaka Fmt, respectively.

In terms of structural and stratigraphic make-up, the Overman area can be taken as the northward continuation of the northernmost gold-bearing zone of the Rosebel District (hosting the Koolhoven and Jzone deposits). This is marked by a sub-vertical orientation of stratigraphic units, tight folding, penetrative schistosity sub-parallel to the bedding and regional foliation, and the presence of shear zones of variable intensity and style (Daoust et al., 2011; Daoust, 2016). Aeromagnetic mapping results highlight the predominant WNW-ESE tendency of the structural-stratigraphic framework (Fig. 2).

The entire rock sequence in the Overman area is strongly deformed, marked by intense foliation and isoclinal folding, but its 3D structural architecture is somewhat ambiguous due to the scarcity of surface outcrops, deep tropical weathering, absence of clear stratigraphic markers, lateral and vertical discontinuities of silicified layers and strong competence differences with interbedded *meta*-sediments. Hence, the map view and cross section depicted in Figs. 4 and 5 are schematic, as they largely rely on logging interpretations of > 150 diamond drill cores (average length ~ 130 m., maximum 375 m; mostly steeply inclined to the NE) collected during multiple exploration programs (2009–2017; Iamgold Corporation, 2017), and on airborne magnetic mapping. The

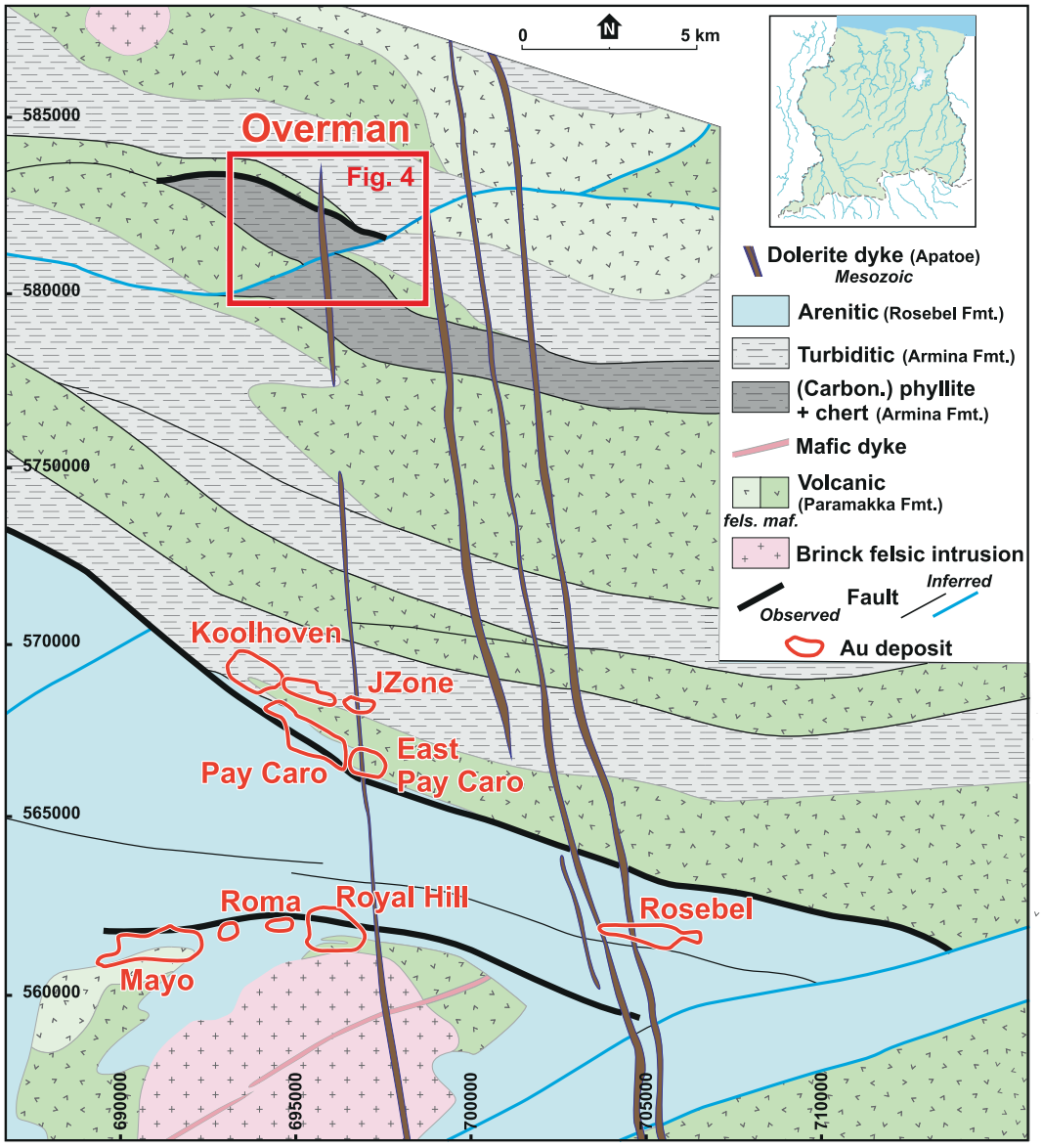

Fig. 2. Schematic distribution of lithological units from aeromagnetic mapping, illustrating the geological setting of the Overman gold deposit relative to deposits in the Rosebel Gold District (after Daoust et al., 2011; Kioe-A-Sen et al., 2016). Formation labels are based on main lithological characteristics only. All units are Early Proterozoic in age, except for the crosscutting dolerite dykes (Apatoe), which belong to the Early Mesozoic swarm marking the opening of the Atlantic Ocean (Deckart et al., 1997; Nomade et al., 2000, 2002).

following lithological units in the overall mostly steeply SSW dipping sequence of layered and tectonised *meta*-sediments are distinguished here (see Supplementary Figs. S2 and 3 for field images):

Chert Unit (silica body; ChU). This tabular auriferous unit locally shows weak layering or foliation, consistent with a sedimentary rock as precursor of extensive silicification. Rigid chert alternates with more weathered parts that apparently produced much of the sandy material spread around the hill. Late quartz veining add to the silica-dominant nature of the unit. Weathering-induced iron enrichment locally gives the rock a rusty reddish appearance, either along fissures or pervasively. In map view (Fig. 4) the silica body extends some 3 km to the ESE, where it is offset by an ENE-WSW running fault with an apparent dextral component as inferred from aeromagnetic data (Iamgold Corporation, 2017). The geometry of the Chert Unit shows spatial discontinuities, presumably resulting from tectonic deformation and incomplete silicification of precursor rock.

Carbonaceous Phyllite Unit (CPhU). Fine-grained carbon-rich phyllites, strongly affected by multiple deformation phases, are juxtaposed mainly against the northern margin of the Chert Unit. Irregular boundaries and transitional fabrics suggest that carbonaceous phyllites were a precursor lithology of chert and most susceptible to processes. A sharp, near-vertical contact on the south-west face of the Overman Hill shows indications of late shearing, apparently facilitated by a strong competence contrast with the chert.

Phyllite Unit (PhU). Consisting of fine-grained phyllites and subordinate intervals of coarser material (*meta*-greywacke) and other undifferentiated clastic *meta*-sediments, this unit represents the dominant lithology in the Overman area and is the principal host of the auriferous silica body (Fig. 4). It is locally interbedded with dark, carbonaceous phyllite along sharp contacts. In surface outcrops the rocks are strongly weathered, with light to medium-grey colorations revealing original heterogeneous bedding in mostly fine-grained sediment, locally enriched in carbonaceous components. Variations in ferruginous weathering of individual layers also contributes to colour diversity. Pervasive foliation dominates widespread textural imprints of complex deformation (see below) and is largely due to late shearing, often sub-

Fig. 3. The Overman Hill looking northwest. The prominent body of whitish silicified rock (chert) is surrounded by fine-grained *meta*-sediments with reddish appearance from intense lateritic weathering.

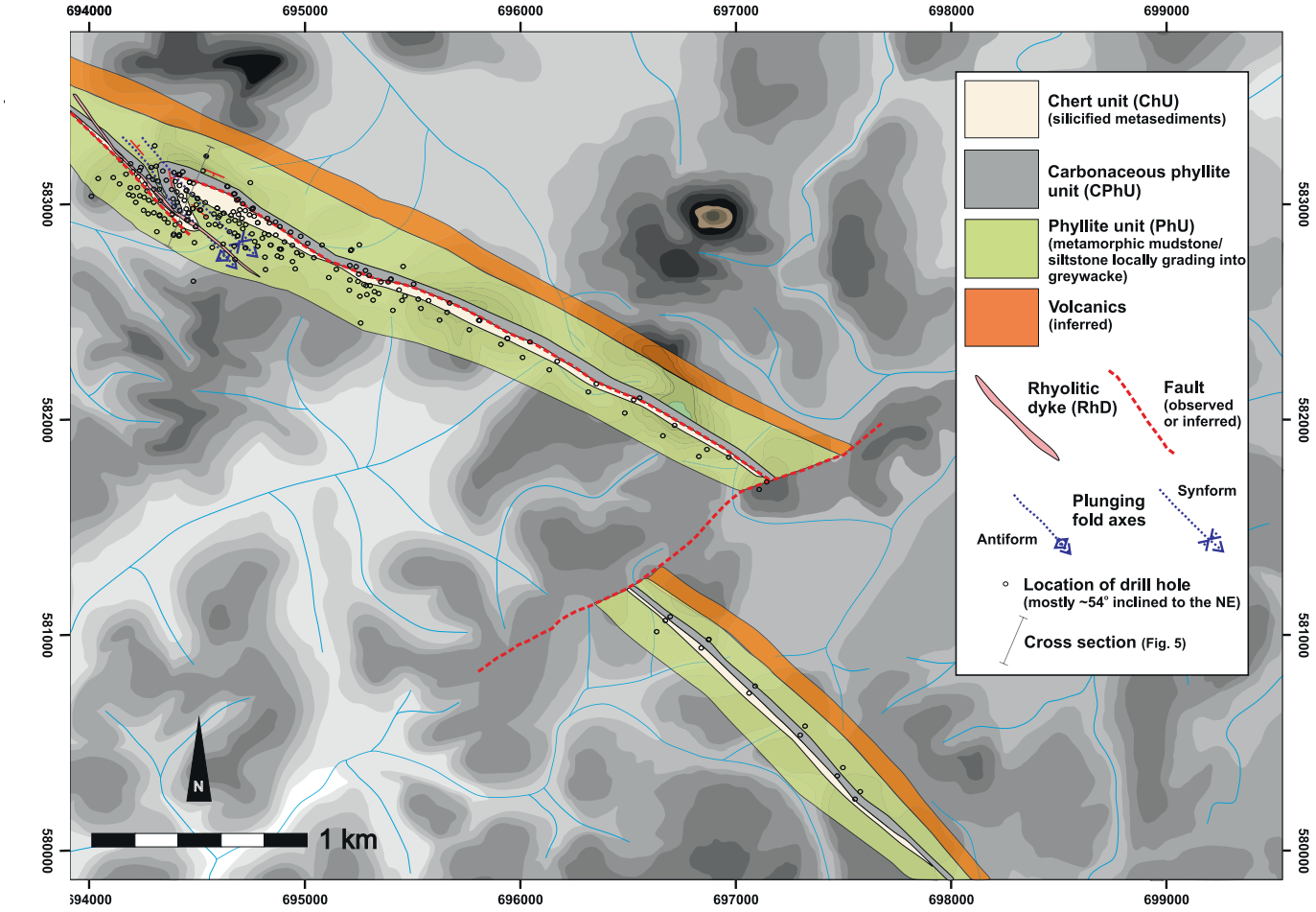

Fig. 4. Schematic geological map of the Overman gold deposit showing the spatial distribution of auriferous chert and associated lithological units as interpreted from logging of drill cores (dots), field-based surveys and aeromagnetic exploration data (see text). Structural features are largely inferred from indirect evidence and only locally supported by field observations. The presence of volcanics on the northern margin of the sequence is indicative only and remains to be confirmed in surface outcrops.

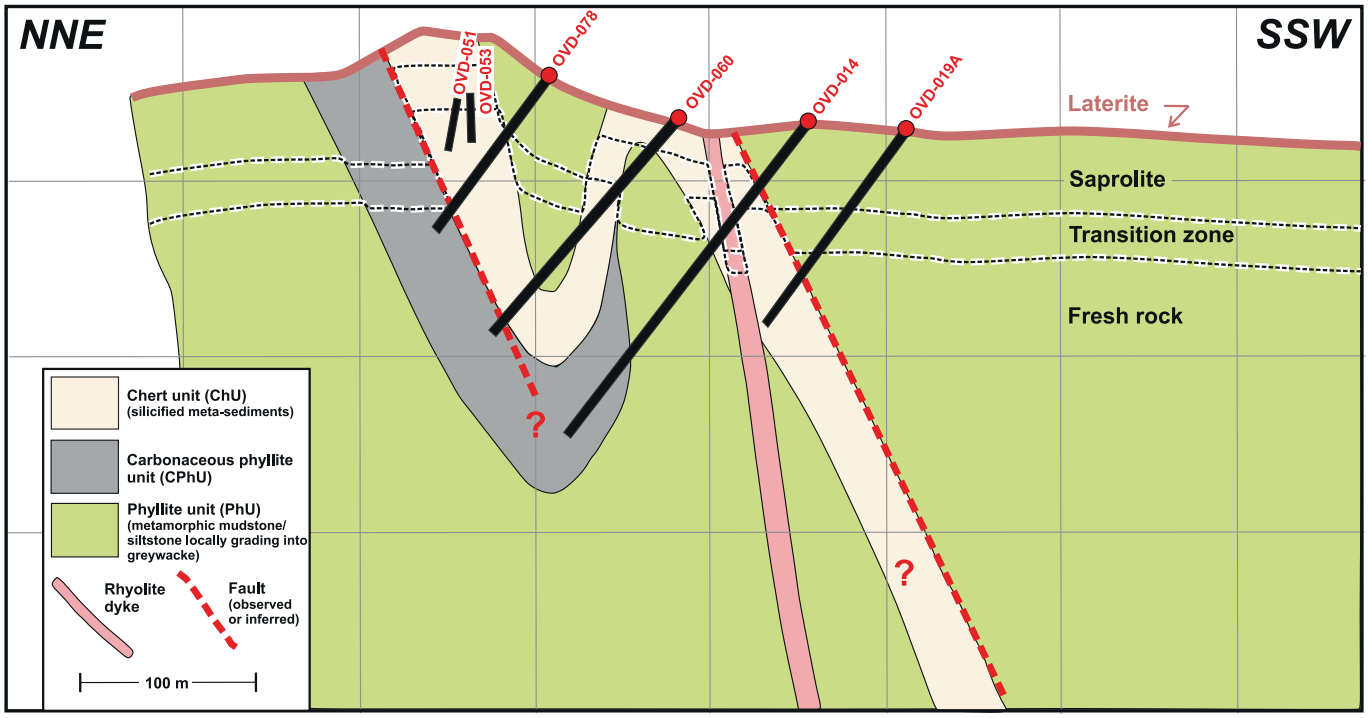

Fig. 5. Section across the Overman gold deposit (location in Fig. 4), with preferred structural interpretation based on drill core logging and surface exposures. Although the entire sequence tends to dip steeply to the SSW, linear symbols of lithological units are not meant to indicate bedding orientations in detail. Weathering profile (laterite-saprolite-transition zone-fresh rock) is based on average depths of the respective boundaries deduced from core descriptions. Grid quadrangles are 100x100m.

parallel to the bedding plane. Collectively, the macroscopic observations are consistent with a generally steep SSW-directed dip of the unit.

Volcanics. The presence of (meta-)volcanics fringing the northern flank of the sequence (Fig. 4) has been suggested from the aeromagnetic survey. This interpretation would fit with the intercalation of Paramaka volcanics in the tectonically stacked sequence envisaged for the region at large (Fig. 2), but volcanic rocks have not been encountered in surface outcrops along the Overman deposit, nor have they been convincingly identified in drill cores. They will therefore not be treated here.

Rhyolitic dyke (RhD). A sheet-like, up to 10 m thick felsic dyke with a sub-vertical orientation and NW-SE trending strike dissects the stratigraphy in the Overman Hill area (Figs. 4 and 5). Evidence for significant deformation is lacking. The dyke thus represents a late intrusion event that post-dates gold mineralisation. A porphyritic appearance is discernible in local surface exposures despite strong weathering. The heavily altered, sometimes clayish rock contains disseminated grains of bluish oxidised pyrite and veinlets of smoky quartz.

Thin dark grey to smoky-purple *quartz veins* are present in every lithology but are most abundant in the chert rock where they often occur in extension fractures. These tension and shear veins with thicknesses between 1 and 5 cm, locally up to 25 cm, run parallel to or crosscut the bedding. Intersections and the presence of undeformed as well as folded generations point to a protracted veining history. The exposed veins, apparently emplaced late in the sequence of geological events, show no signs of mineralisation and are gold-barren.

Other structural features visible at outcrop scale are limited, which hampers an unambiguous analysis of the deformation history. Minor folds in relatively competent siliceous layers suggest the presence of at least two phases of deformation. Folding is also inferred from bedding planes measured in the phyllitic units on different sides of the central silica body, showing steep dips in opposite directions. This suggests a synform structure with a near-vertically inclined axial plane, striking almost parallel to the main WNW-ESE orientation of the silica body. A penetrative set of at least two foliations, occasionally visible in phyllite, is also sub-parallel to the bedding. The chert body shows evidence of localised brittle deformation in the form of networks of fractures and more randomly brecciated intervals. Flattening of breccia clasts tends to suggest a steeply SW dipping to sub-vertical, ESE striking foliation. The top of the chert body is marked by multiple sets of sub-vertical joints and fissures.

The preferred interpretation for the geometry of the silica body is that it is folded and represents a synform-antiform pair with south-eastward plunging axes near the Overman Hill (Figs. 4 and 5). Shearing, largely sub-parallel to the contact between the chert and the phyllites, is inferred to have affected the structure. Further to the south-east, where the silica-body is intercalated in the same *meta*-sediment units, the steeply dipping sequence tends to be less disturbed.

Superimposed on this primary lithological framework, extensive tropical weathering has produced deep profiles until fresh rock is reached (mostly 50–80 m, locally down to > 100 m), made up of a laterite top with a duricrust, a saprolite zone and a transition zone (Supplementary Fig. S4). Depths of the boundaries between these zones are highly variable and often diffuse, apparently controlled by local permeability differences associated with lithological composition and the presence of sub-vertical faults.

3. Results

.

3.1. Petrographic characteristics of the ore host and associated units

.

3.1.1. Silica-rich body (Chert Unit, ChU)

.

3.1.1.1. General features and textural varieties. The Chert Unit is

composed of siliceous rock, generally consisting of more than 90 % quartz, and minor amounts of up to ca. 5 m thick interbedded layers of non-silicified *meta*-sediments. It has a variable thickness between some 20 m in the south-west and 70 m near the Overman hill, and is the principal host of the gold ore and associated sulphide minerals. Dark quartz veins add to the siliceous character of the unit, but these are barren in gold and sulphides. Due to the often intense and pervasive silicification, original rock textures are difficult to discern, making it a challenge to determine the lithological nature of the precursor from macroscopic observations. Generally sharp contacts between the chert body and the stratigraphically underlying carbonaceous phyllites show evidence of faulting and shearing. Locally the transition is gradual and more akin to a silicification front that is occasionally tectonised, sometimes oblique to the original bedding.

Macroscopically the siliceous rocks show a wide diversity of textures and colours in drill core samples. Broadly, three main texture groups, with gradual transitions, can be distinguished: (1) brecciated, (2) massive with (a) vitreous and (b) whitish quartz-vein-like varieties, and (3) vuggy/spotted. The massive and brecciated groups are most abundant and contain vuggy intervals. Colours vary from white to light-medium grey and greenish grey-black with sharp or gradual transitions at scales ranging from several metres to decimetres. Absence of systematic texture changes with depth precludes unequivocal stratigraphic correlations between drill holes. Obvious relationships between texture type, degree of sulphide mineralisation or presence of visible gold are lacking. A wide variety of chert types can be found in individual drill holes (e.g., OVD-053, containing an interval with the highest gold contents; see Supplementary Fig. S1 and Supplementary Table S1a and 1b for drill core locations and origin of samples mentioned further on). Key features are as follows:

Rocks with the *brecciated texture* are marked by an abundance of dark fractures separating whitish, in-situ fragmented clasts of silicified rock with angular to sub-angular jigsaw-fitting outlines (Fig. 6). The fractures are largely filled with sulphide and/or (secondary) Fe-oxide and are often unevenly distributed within individual drill cores and at hand specimen scale, showing random orientations as well as alignments in single or multiple intersecting sets. Microscopic observations reveal that the enclosed domains consist of equigranular microcrystalline quartz (microquartz, <100 μm) with irregular outlines but grainsizes may locally vary in the vicinity of fractures (<20 μm) or veinlets (ca. 250 μm). In some samples the microquartz grains are elongated, forming a fabric with a preferred orientation, apparently a result of shear-related deformation. Fine-grained opaque minerals (sulphides and/or Fe-oxides) are not only disseminated in the microquartz matrix but are often aligned in straight trails or along tortuously curved boundaries between larger domains (Figs. 6d,e,f). They also form coatings on the inside of voids that were apparently left after dissolution of a precursor mineral.

Chert with a *massive crystalline texture* can be distinguished into:

Varieties of dense, strongly silicified rock with a vitreous appearance, greenish-grey and medium-dark grey to black colour with local whitish selvages and little structure (Fig. 7a-h); they commonly contain abundant sulphides. In the greenish-grey variety these are usually evenly dispersed throughout the rock. Elsewhere, sulphide-rich and poor domains are separated by sharp boundaries. Visible gold grains were observed in samples with this texture (see Fig. 9b below). Microscopic inspection reveals the strong predominance of small quartz crystals (usually < 200 μm). The micro-quartz grains have boundaries ranging in shape from (near-) polygonal to strongly serrate and often show patchy undulose extinction. In some samples they exhibit a shape-preferred orientation, defining a continuous foliation. More pronounced grain elongation and size reduction are seen in domains of thin sections with clear evidence of shearing. All of these textural features are consistent with dynamic recrystallisation of quartz-rich rock fabrics. The presence of small flakes of white mica is rare. Opaque minerals are small and typically fill voids, either interstitially between the quartz grains (shapes are elongated in cases of a foliated fabric), or in thin curved to straight fissures with sub-parallel or near-random orientation.

Whitish-light grey quartz-vein-like types, often containing a network of dark veins with dendritic outlines, mostly consisting of Fe-oxide and/or sulphide. Fractures are generally less abundant than in the brecciated type and are locally filled with a reddish brown Fe-oxide (probably hematite) (Fig. 7i-o). The textures vary from compact to sugary-porous (presumably due to weathering) and locally suggestive of foliation.

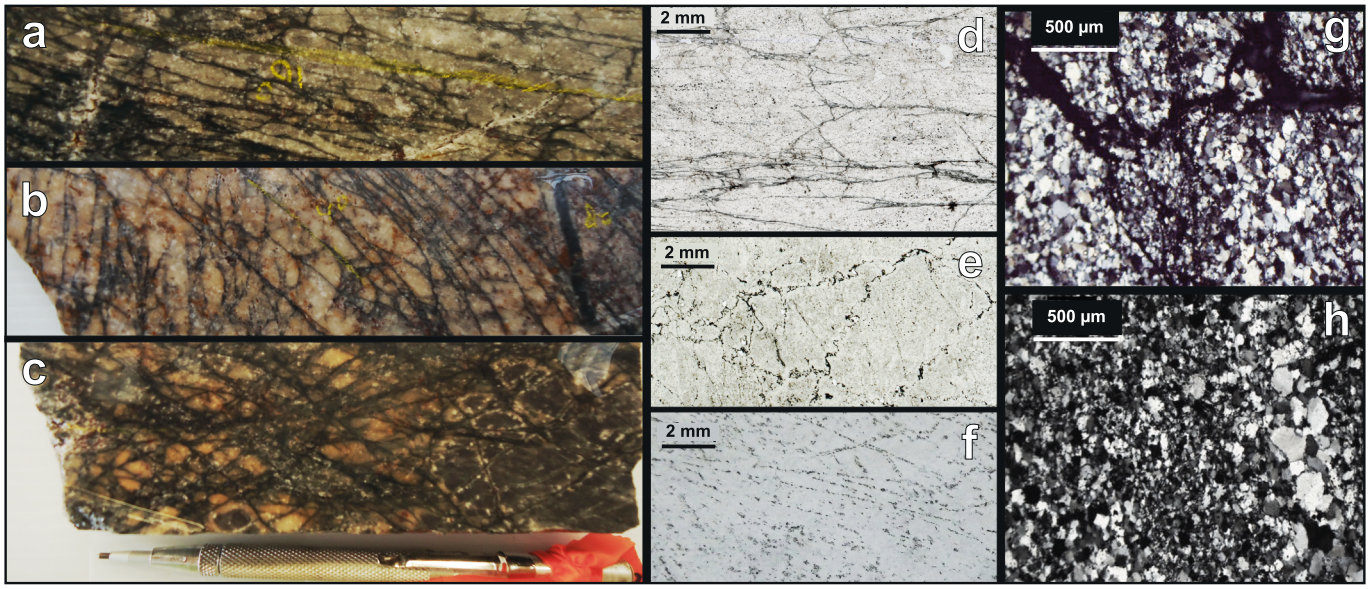

Fig. 6. Textures in brecciated intervals of the ChU shown in core samples (a-c), thin-section scans in PPL (d-f), and microphotographs in XPL (g-h); (a) elongated domains of micro-quartz separated by largely parallel fractures; (b and c) angular domains of micro-quartz separated by intersecting sets of fractures in (b), and by more randomly oriented sets of fractures and roundish grains with spotted outlines in (c); (d) micro-quartz with anastomosing shear-induced micro-fractures lined by small sulphide grains and other opaque material; (e) domains of micro- quartz bordered by multiple sets of stylolites, which are lined by small sulphide grains and other opaque material; (f) micro-quartz with intersecting sets of shear-induced micro-fractures lined by small sulphide grains and other opaque material; (g) and (h) equigranular domains (g) and size variability (h) of micro-quartz.

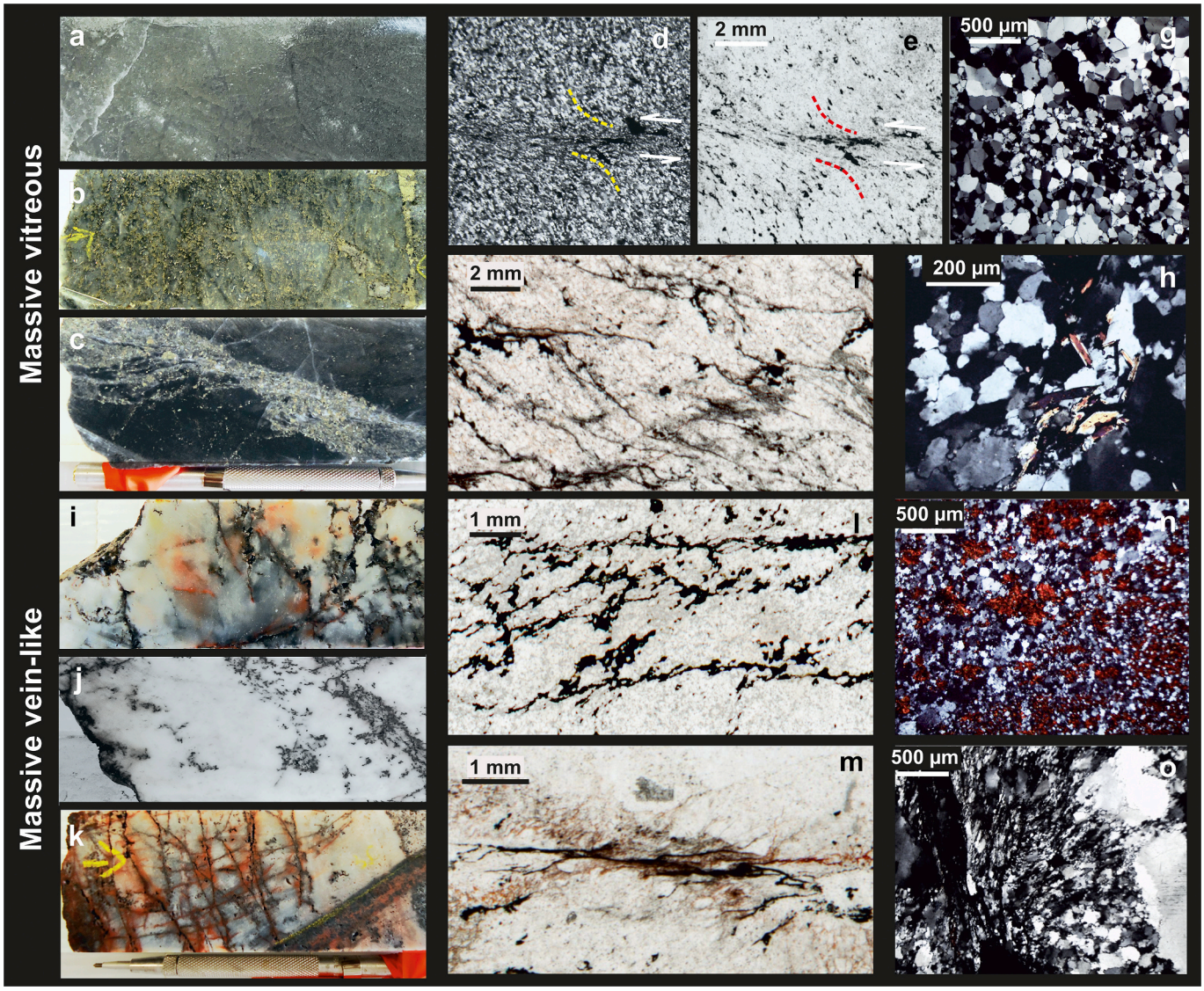

Fig. 7. Textures of vitreous and vein-like varieties of massive ChU intervals shown in core samples (a-c, i-k), thin-section scans in PPL (e-f, l-m) and XPL (d), and microphotographs in XPL (g-h, n-o); (a) greenish-grey chert containing fine to medium-grained sulphides; (b) dark-grey to black chert containing abundant pyrite (disseminated and in vein) and coarse subhedral arsenopyrite; (c) dark- grey to black chert with coarse sulphide crystals (mostly pyrite) concentrated in vein-like structure, along micro-fractures and dispersed; (d) foliated fabric of micro-quartz grains with variable degrees of elongation, inferred to be the result of shear-induced dynamic recrystallisation; note that orientation of sulphides (anhedral pyrite and euhedral arsenopyrite) in trails and fractures largely follows the foliation trend; (e) PPL equivalent of (d); (f) matrix of micro-quartz dissected by shear fractures lined by small sulphide grains; (g) micro-quartz grains with undulose extinction and size variation; (h) micro-quartz with irregular grain boundaries suggestive of bulging recrystallisation; yellowish and brownish grains are flakes of white mica; (i-k) milky white quartz with dendritic trails of sulphide (dark) and reddish stains and fractures filled with Fe-oxide (l) micro-quartz with shear fractures lined with small grains of sulphide; (m) shear fracture in micro-quartz; reddish linings due to secondary Fe-oxide; (n) micro-quartz and interstitial Fe-oxide (red); (o) heterogeneous grain sizes of quartz, irregular boundaries suggesting bulging recrystallisation and hematite-filled fracture (blackish domains).

Contacts with the other types are mostly sharp but, in some cases gradual. These quartz-vein like intervals are often associated with an up to a few metres thick layer of light-medium grey, fine-grained silicified rock, probably of sedimentary origin, with fractures mostly filled with reddish brown material (e.g., Fig. 7k). Fracture density tends to be lower than in cherts of the brecciated type. Grain sizes of the microquartz are generally similar to those in the previous type but tend to be more variable as a result of bulging recrystallisation, incomplete recrystallisation of larger quartz porphyroclasts or original textural heterogeneity in the precursor rock prior to silicification. Mineral shapes and lithological features of the original rock are locally still discernible in thin sections, despite pervasive replacement by quartz. The overall observations suggest that this chert type experienced less pronounced (shear) deformation and accompanying recrystallisation than the massive vitreous chert. Opaque minerals are distributed as fillings of small interstitial pores often connected to form sets of curvy anastomosing veinlets or straighter arrays, sometimes suggestive of following boundaries of former minerals or distinct domains that existed prior to silicification. In fresh parts the opaques consist of sulphides, whereas reddish colours signal partial or complete replacement by hematite, which also occurs as filling of thin secondary veinlets.

Domains of silicified rock with the *vuggy/spotted texture* have a dark matrix with sub-circular concentrations of whitish quartz around voids that may contain remnants of sulphides and/or secondary Fe-oxides, giving the chert a granular appearance (Fig. 8). Whitish quartz also occurs as annular rims around relatively large dark clots, presumably ghosts of coarse clasts present in the protolith prior to silicification. In other cases, vugs are present alone. The occurrence of vuggy/spotted

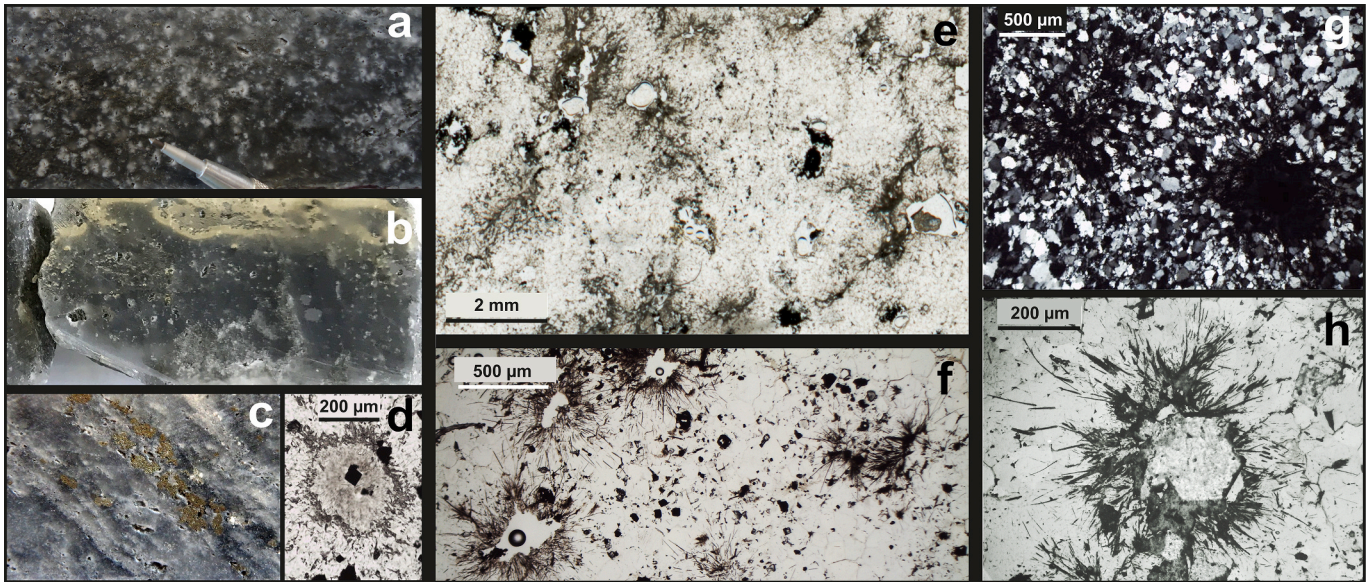

Fig. 8. Textures of vuggy/spotted intervals in the ChU illustrated in core samples (a-c), thin-section scan in PPL (e) and microphotographs in PPL (d, f, h) and XPL (g); (a) granular microcrystalline chert with pale spots and voids; (b) massive vitreous chert with voids; (c) massive microcrystalline chert with voids and abundant pyrite parallel to colour banding; (d) ghost of a precursor mineral outlined by tiny needles of an unidentified secondary mineral in matrix of micro-quartz with euhedral sulphide grains; (e-f) vuggy microcrystalline quartz, relic sulphides and a dusty secondary mineral (Fe-oxide?) radiating outward from voids with euhedral outlines of a precursor mineral, presumably pyrite; (g) detail of (e); opaque areas are secondary Fe-oxide; (h) detail of (f) showing feathery mineral (Fe-oxide?) radiating outward from altered mineral with euhedral shape, probably arsenopyrite.

features is not unique to specific intervals but may be superimposed on other texture types. Under the microscope, microquartz (<200 µm) is again ubiquitous, showing serrate grain shapes in variable sizes, which points to localised heterogeneity induced during progressive recrystallisation. Preserved ghost textures from precursor rock indicate relatively modest deformation at least on micro-scale. Opaque minerals (mostly subhedral sulphides) are either disseminated in the quartz matrix or (partly) fill voids. Radial textural patterns suggest that pore spaces acted as centres from which fluid infiltrated further into the surrounding quartz along grains boundaries, either during the mineralisation event or during recent secondary weathering. In other cases, bundles of bladed or acicular crystals, presumably Fe-(hydr)oxide, radiate outward from a void, sulphide crystal or Fe-rich alteration product.

3.1.1.2. Mineralisation: Sulphides and gold. Sulphides represent the main mineral phase after quartz in the most silicified and unaltered parts of the chert body and have been found throughout the deposit in variable abundances. At thin-section scale, the sulphides not only tend to be disseminated within the rock but also form trails and clusters in spaces between quartz grains (Figs. 6-8). Assemblages are heterogeneous and

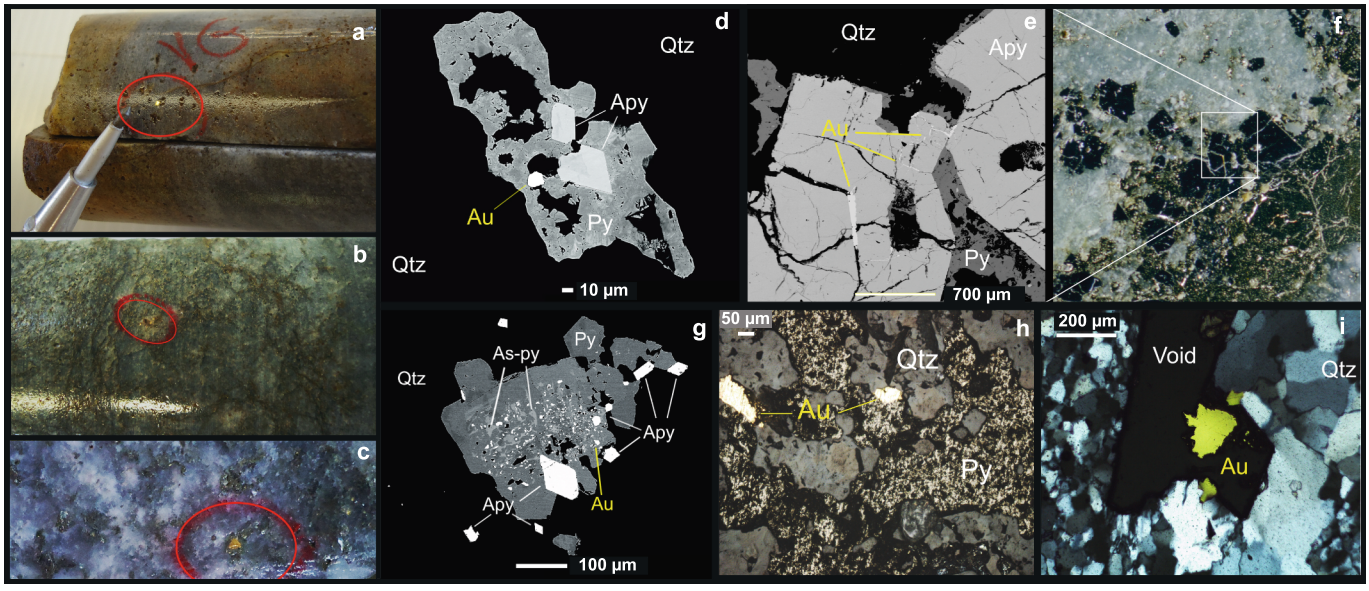

Fig. 9. Examples of visible gold in the ChU in core samples (a-b-c), BSE images (d, e, g), slab of polished rock (f), and optical microscope images in RL (h) and combined RL-XPL (i); (a-b-c) macroscopically visible gold specs; (d) gold grain in anhedral cluster of pyrite (Py) associated with euhedral arsenopyrite (Apy); (e) detail of cluster of dark and yellow sulphides in (f) showing gold-filled fractures in arsenopyrite fringed by pyrite; (g) sulphide cluster of pyrite, arsenian pyrite (As-py) and arsenopyrite containing small inclusion of gold; (h) association of gold grains with pyrite aggregate; (i) gold in vug left after dissolution of sulphide host; quartz veinlet in sample of microcrystalline chert from the core shown in (a).

mostly made up by microcrystalline aggregates of pyrite and euhedral arsenopyrite, whereas pyrrhotite is less common, and small grains of chalcopyrite, galena, sphalerite and unidentified Fe-(Sb)-Pb and As-Sb-Fe-Cu phases are rare.

Macroscopically visible gold is locally present in the form of tiny specs (Fig. 9a-c), which are usually associated with the sulphides. Its presence is not connected to a specific texture type of the chert, although it was mostly observed in the massive glassy variety. Microscopically visible gold appears in different forms and associations (Fig. 9d-i). Small grains occur as inclusions and in contact with pyrite, as inclusions or fracture fill in arsenopyrite, and as isolated grains in quartz-rich domains.

3.1.2. *Carbonaceous phyllite Unit (CPhU)*

This unit consists predominantly of dark grey to black, strongly deformed, phyllitic *meta*-sediments rich in carbonaceous matter (Fig. 10a-d). White mica, chlorite and quartz are the main silicate phase, occurring in variable proportions that tend to replicate original fine-scale compositional layering. Albite is locally present as porphyroblasts or subordinate matrix phase. Primary accessory minerals include

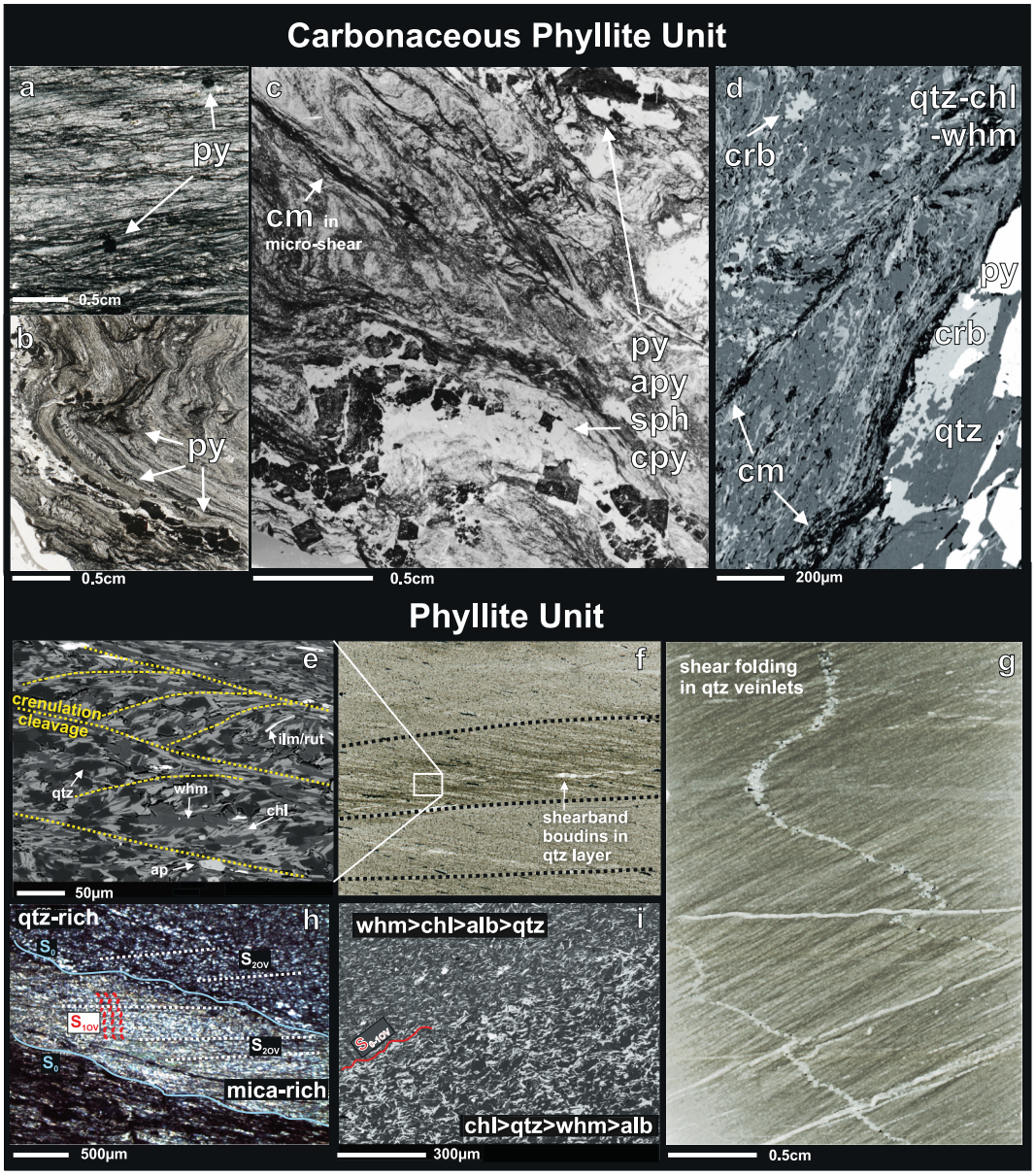

Fig. 10. Micro-textures of multiple phases of deformation (micro-folding, –shearing) and veining in CPhU (a-d) and PhU (e-g) samples, illustrated in PPL thin-section scans (a-c, f, g), BSE images (d, e, i) and an XPL optical microscope image (h); (a-c) micro-folds in mica-rich domains and anastomosing shear planes lined with carbonaceous matter; note sigmoid mica fishes between irregularly spaced shear foliation (dark) and isolated late-/post-deformation pyrite grains in (a), the association of pyrite crystals with folded quartz veins in (b), and the association of euhedral pyrite crystals, minor arsenopyrite, chalcopyrite and sphalerite with folded veins in (c); (d) same thin section as (c), highlighting complexly folded matrix of chlorite, white mica, quartz and carbonaceous matter (dark), as well as a quartz-carbonate vein with pyrite; (e-f) multiple deformation phases expressed in S-C fabric with shear banding and micro-boudinage in chlorite-white mica-quartz PhU sample; note that elongated ilmenite grains (white in e, black in f) tend to be aligned parallel to the C-foliation; (g) penetrative planar shear foliation and multiple generations of quartz veinlets affected by different degrees of shear-induced micro-folding; (h-i) variations in the proportions of metamorphic minerals due to fine-scale compositional layering in the original sediments; primary layering (S_{0OV}), micro-folded S_{1OV} and crenulation cleavage (S_{2OV}) in a mica-rich band are visible in (h), and compositional layering with micro-folding in (i). Abbreviations: py = pyrite, apy = arsenopyrite, cpy = chalcopyrite, sph-sphalerite, qtz = quartz, chl = chlorite, whm = white mica, crb = carbonate, alb = albite, ilm = ilmenite, ru = rutile, ap = apatite.

apatite, monazite and rutile. Carbonate and relatively undeformed pockets of chlorite crystallised late in the tectono-metamorphic sequence. Tight micro-folding, pervasive foliation, shearing features and frequent development of a crenulation cleavage point to multiple, superimposed deformation events. Different generations of quartz and carbonate veinlets (partly) follow micro-folds or crosscut deformation structures (Figs. 10c,d). The unit is marked by locally abundant, relatively large sulphide crystals, which are either associated with quartz and/or carbonate in veins or appear as isolated blasts in the fine-grained matrix (Fig. 10b-d). Pyrite is dominant, arsenopyrite is much less abundant, whereas minor pyrrhotite, chalcopyrite, sphalerite and rare Co-Ni-Fe-As-sulfarsenides and Pb-Fe sulphide have been found as well. Larger porphyroblasts and composite grains of the matrix-type sulphides are often marked by "clean" euhedral to subhedral outer margins and poikilitic cores with internal patterns of minerals inclusions and voids preserving original micro-structures. In other cases, the pyrites show evidence of deformation and have fringes of fibrous quartz and occasionally carbonate in strain shadows. They may be intergrown with disseminated Ca-Fe carbonate and are occasionally rimmed by arsenopyrite grains. Euhedral, up to 0.5 cm-sized pyrites in the veins may be associated with minor arsenopyrite and other sulphides (Fig. 10c) and often contain chalcopyrite as inclusions. The diversity of matrix grain textures and deformation degree of sulphide-bearing veins in the investigated samples suggest a protracted mineralisation history of the pyrites involving pre-, syn- and late to post-kinematic intervals. Secondary Cu-sulphides and oxidised arsenopyrite and pyrrhotite may occur as alteration products.

3.1.3. Phyllite Unit (PhU)

The Phyllite Unit consist of heterogeneous, fine-grained medium to dark grey-greenish rocks with locally distinguishable mm-to-dm thick alternating darker and paler layers that presumably represent original sedimentary bedding (Fig. 10e-g). Where preserved, this stratification is consistent with deposition as a laminated mudstone-siltstone sequence of fine-grained turbidite. Coarser-grained varieties grade into a *meta*-greywacke. The frequent absence or poor distinguishability of stratification at hand-specimen or thin-section scale is largely due to multiple generations of foliation, veining and shearing, signalling a complex deformation history. The rocks are predominantly composed of fine-grained white mica, chlorite, quartz ± albite in variable proportions, apparently determined by the pre-metamorphic sedimentary layering (Figs. 10h,i). Mica and/or chlorite-rich laminae usually define a tightly spaced pervasive parallel foliation, but the platy mineral phases may also form typical S-C fabrics (Fig. 10e) or sets of foliation planes crosscutting each other at high angles. Multiple generations of quartz veinlets (e.g., Fig. 10g) marked by different degrees of deformation (micro-folding, boudinage, fracturing). Individual grains of the main mineral constituents are largely subhedral and equigranular, with largest dimensions reaching ca. 50 μm. When present, elongated crystals or aggregates of opaque minerals (Fe-Ti oxide or sulphide) are usually oriented parallel to the most prominent foliation (Fig. 10f). Subordinate amounts of carbonaceous matter, epidote, biotite, amphibole or carbonate are locally present as well. Minor amounts of sulphide may be associated with carbonate pockets or quartz veinlets. Relatively quartz rich laminae that tend to be slightly coarser usually contain more chlorite than mica and show less pronounced schistosity to virtually isotropic fabrics. The quartz grains are often more angular to subround and are more variable in size (up to ca. 250 μm).

3.1.4. Late quartz veins

Late quartz veins crosscutting the silica body are mostly dark grey black (sometimes bluish), have variable thicknesses up to several centimetres (Supplementary Fig. S3a,b), and are generally devoid of significant sulphides or gold mineralisation. Sulphides were only locally found as traces or in thin layered concentrations at contacts. In drill core, the veins show different orientations relative to core axis or relic foliation/bedding, or constitute a network. Their occurrence is not linked to a specific texture type of chert host.

3.1.5. Rhyolitic dyke (RhD)

The intrusive igneous rock is a subvertical, up to ca. 10 m thick felsic dyke crosscutting the other units generally against sharp contacts. Multiple intervals encountered in some of the drill cores suggest the presence of more than a single intrusion or are an effect of branching at depth. The crystal-rich porphyritic rock appears in various tints of grey with a greenish hue and is whitish yellow in weathered parts. Subhedral plagioclase, often clustered, and subrounded quartz with embayments are the main phenocrysts set in a fine-grained groundmass consisting largely of quartz, chlorite, white mica, clayey and other secondary minerals (Fig. 11a-c). Zircon, apatite, monazite and rutile are accessory phases. Fresh coarse grains of euhedral pyrite, locally fragmented into aggregates of small crystals, are disseminated through the rock (Fig. 11e). Minor pyrrhotite, often altered, occurs in anhedral aggregates and as intergrowths or inclusions in pyrite. Tiny grains of chalcopyrite and galena are occasionally included in pyrite, and Fe-Ca carbonate and Fe-Ti (hydr)oxides represent alteration products. Intervals of the dyke in some of the cores are pervasively hydrothermally altered into an albite-rich assemblage containing white mica, chlorite, carbonate, and pyrrhotite, with quartz phenocrysts left as only unaffected igneous phase (Figs. 11d,f,g).

3.2. Geothermometry

.

3.2.1. Chlorite thermometry

.

3.2.1.1. Chlorite compositions. Chlorite geothermometry has been applied on the phyllitic units, regarding its broad relevance to rocks that underwent hydrothermal alteration, diagenesis or low to medium-grade metamorphism, including Precambrian mineralised lithologies (e.g., Kranidiotis and MacLean, 1987; Frimmel, 1997; Klein and Koppe, 2000; Klein et al., 2007; Dora and Randive, 2015; Pant et al., 2019). Thin sections of five drill core samples from the PhU (true vertical depths between 140 and 250 m) and four samples from the CPhU (true vertical depths between 120 and 190 m) were selected for electron-microprobe analyses to explore the temperature conditions during metamorphism of the Overman sequence. Details on the drill cores from which the samples were taken are given in Supplementary Fig. S1 and Supplementary Table S1. The analytical procedure, chlorite classification details and background on the thermometry are outlined in Supplementary document S1. Averaged results are reported in Table 1 and the complete data set in Supplementary Table S2.

3.2.1.2. Thermometry results. Multiple empirical chlorite geothermometers have been developed from observed relationships between the tetrahedral Al occupancy (Al-IV) or the octahedral vacancy and temperatures derived independently by other methods (see reviews of Yavuz et al., 2015; Bourdelle, 2021). Some of the calibrations require a correction based on the Fe/Mg ratio to account for effects from Fe^{2+}-Mg^{2+} substitutions. A set of twelve empirical thermometers were applied to estimate the formation temperature of the Overman chlorites using the WinCcac routine of Yavuz et al. (2015) and assuming that all iron is present as Fe^{2+}. The chlorites in the samples from both rock units yielded a wide range of temperatures (Supplementary Table S2). For most thermometers, the calculated temperatures for the PhU produced averages between ca. 270 and 420 °C, whereas those for the CPhU yielded averages between ca. 260 and 350 °C (Fig. 12).

Temperatures were also estimated with the semi-empirical thermometers of Inoue et al. (2009), Bourdelle et al. (2013), and the Chl(2)

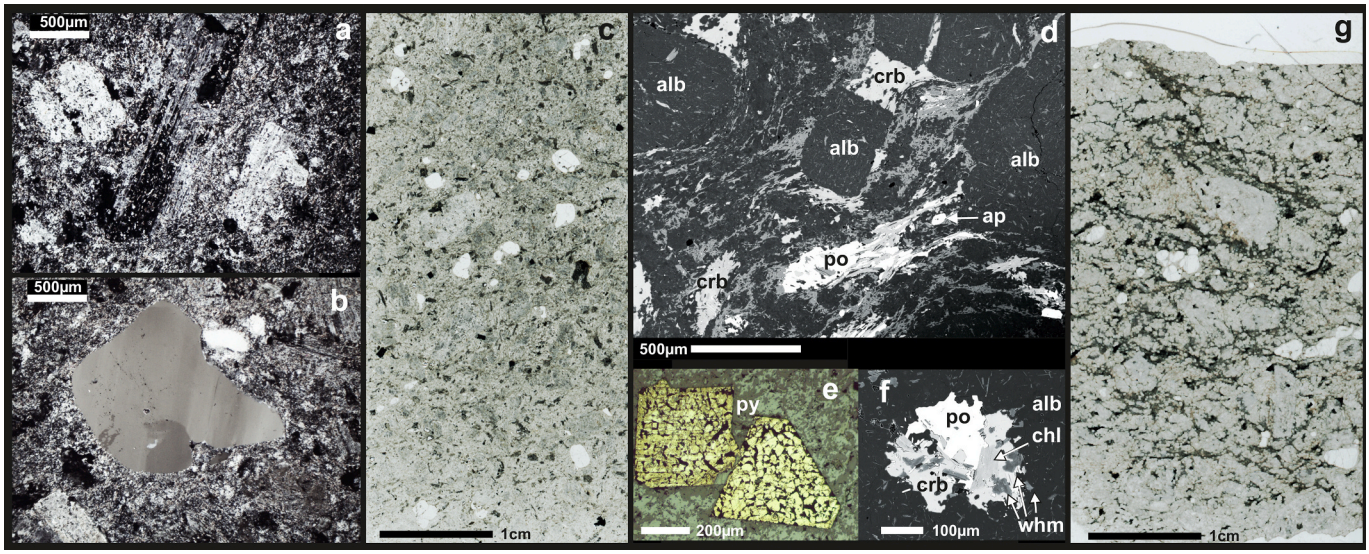

Fig. 11. Textural features of relatively fresh (a, b, c, e) and albitised (d, f, g) portions of the rhyolitic dyke dissecting the Overman structure, shown in optical microscope images in XPL (a, b) and RL (e), thin-section scans in PPL (c, g), and BSE images (d, f); (a) cluster of plagioclase phenocrysts set in a fine-grained altered groundmass; (b) rounded quartz phenocryst with deformation-induced undulose extinction; (c) porphyritic character with abundant plagioclase and rounded quartz phenocrysts (white); many of the opaque grains are disseminated pyrite; (d) hydrothermally altered sample with abundant albite (dark crystals) surrounded by foliated white mica and chlorite; note patches of pyrrhotite (white) with carbonate (lightest grey), and accessorial apatite; (e) euhedral pyrites showing effects of fragmentation and recrystallisation into aggregate of small grains; (f) pyrrhotite-carbonate cluster with white mica and chlorite surrounded by albite; (g) strongly albitised portion of the rhyolitic dyke; note tendency of foliated orientation of chlorite-white mica and original quartz phenocrysts with same appearance as in (c). po = pyrrhotite, other mineral abbreviations as in Fig. 10.

thermometer of Lanari et al. (2014). The latter requires an assumption on the formation pressure, for which an arbitrary value of 2 kb was adopted. A pressure of 5 kb would yield 40–60 °C higher temperatures. Details are given in Supplementary Table S2.

The thermometers of Bourdelle et al. (2013) and Lanari et al. (2014) yielded a broad range of temperatures between 200 and 800 °C, with a maximum frequency around 475 °C for the analysed chlorites of the PhU (Fig. 12). The thermometer of Inoue et al. (2009) produced more uniform results with a similar peak near 500 °C. The temperatures are thus in all three cases substantially higher than those inferred from the empirical thermometers. In contrast, the calculated temperatures for the CPhU chlorites are not in agreement. Unimodal distributions around 275 °C for the Bourdelle et al. (2013) and Lanari et al. (2014) approaches largely correspond to results of the empirical thermometers, whereas the Inoue et al. (2009) thermometer yielded a much higher temperature of ca. 425 °C (Fig. 12).

It must be noted that this latter thermometer may be less suitable for the Overman chlorites, since the authors emphasize that its applicability is restricted to disordered chlorites formed at $T < 250$ °C in diagenetic to very low-grade metamorphic environments, and that the potential presence of Fe^{3+} in the octahedral sites should be taken into account. The two other thermometers assume that all iron in chlorite is in the ferrous state and are considered to be applicable over a wider range of formation conditions, since the Bourdelle et al. (2013) thermometer was calibrated for $T < 350$ °C, $P < 4$ kbar, and the Lanari et al. (2014) thermometer is recommended for sedimentary, hydrothermal and metamorphic chlorites formed at $T = 100–500$ °C and $P = 1–20$ kbar. The considerable difference between results from the empirical and semi-empirical thermometers for the PhU samples is probably due to inherent inaccuracy of the former group, since their applicability is questionable for rocks with other compositions and geological settings than used for the original calibration (e.g., De Caritat, 1993). From these considerations, the semi-empirical thermometers of Bourdelle et al. (2013) and Lanari et al. (2014) probably yield the most accurate estimate for the metamorphic conditions during chlorite formation/equilibration in the Overman *meta*-sediments. Nonetheless, calculated temperatures higher than 600 °C for several spots in the PhU samples are suspicious, as they exceed the upper limit of chlorite stability in *meta*-pelitic rocks (Burnell and Rutherford, 1984) and may represent artefacts, either inherent to limitations of the thermometers or caused by contamination of undetected mineral phases in measured spots.

3.2.2. *Thermometry from the crystallinity of carbonaceous matter*

.

3.2.2.1. Raman spectroscopy. Peak temperatures of metamorphism in the Overman sequence of *meta*-sediments can be inferred from Raman spectroscopy of carbonaceous material (RSCM), since the irreversible transformation of immature organic matter to crystalline graphite is controlled by temperature and is considered to be insensitive to transformation under retrograde conditions (Beyssac et al., 2002). Various RSCM-based methods have demonstrated the validity of this approach to estimate peak metamorphic temperatures for a wide range of rock types and grades of metamorphism, including pelitic and semi-pelitic *meta*-sediments in orogenic belts (e.g., Yui et al., 1996; Nishimura et al., 2000; Rawat and Sharma, 2011; Mori et al., 2019; Kouketsu et al., 2019).

Five CPhU samples from cores to the south of the ore-bearing chert body (see Supplementary Fig. S1) were selected for study. Analytical techniques and procedures are documented in Supplementary document S1. Thin sections from two of the samples did not produce acceptable RSCM temperatures (ca. 110–180 °C) considering the geological setting, which can be attributed to insufficient removal of carbon coating required for electron microprobe analysis. Only the results from three samples (true vertical depth range between 100 and 180 m) are therefore reported here.

3.2.2.2. RSCM thermometry results. The first-order region of Raman spectra of organic matter (CM) comprises a disordered (D) band (at ca. 1340–1360 cm^{-1}) and a graphite (G) band (at ca. 1580 cm^{-1}), following the nomenclature of Henry et al. (2019). Prograde evolution of CM to perfectly ordered graphite is accompanied by a decrease in bands widths and a decrease in D/G intensity ratio, eventually until complete disappearance of the D-band region (Wopenka and Pasteris, 1993). The

Table 1
Average compositions (oxide wt.%) and atomic Fe/(Fe + Mg + Mn) ratios of chlorites in samples from the Phyllite Unit and Carbonaceous Phyllite Unit. Average temperatures (°C) based on the semi-empirical geothermometers of Bourdelle et al. (2013), Inoue et al. (2009) and the Chl(2) geothermometer at 2 Kb of Lanari et al. (2014) were calculated with omission of spots yielding improbable temperatures > 600 °C. Details and a complete data set are given in Supplementary Table S2a-b.

	Carbonaceous Phyllite Unit								**Phyllite Unit**									
Sample	**OVD 93–1**		**OVD 136–142**		**OVD 137**		**OVD 139C**		**OVD 39–185**		**OVD 136–222**		**OVD 137–264**		**OVD 142–266**		**OVD 142–300**	
Number of analysed spots	n = 18		n = 26		n = 40		n = 34		n = 12		n = 21		n = 13		n = 9		n = 21	
	Average	Stdev	Average	Stdev	Average	Stdev	Average	Stdev	Average	Stdev	Average	Stdev	Average	Stdev	Average	Stdev	Average	Stdev
Oxides (wt.%)																		
SiO_2	26.43	0.39	25.44	0.34	26.34	0.63	26.82	0.49	23.82	0.21	23.48	0.16	23.72	0.14	24.19	0.49	23.62	0.28
TiO_2	0.04	0.02	0.04	0.02	0.03	0.02	0.03	0.02	0.1	0.07	0.10	0.06	0.10	0.06	0.04	0.01	0.08	0.03
Al_2O_3	22.21	0.56	22.10	0.48	21.98	0.51	22.73	0.37	22.41	0.30	22.34	0.15	22.45	0.17	22.68	0.40	22.58	0.26
Cr_2O_3	0.01	0.02	0.03	0.03	0.01	0.01	0.03	0.04	0.0	0.02	0.03	0.02	0.04	0.02	0.06	0.02	0.05	0.02
FeO (tot)	16.15	1.37	20.58	0.89	16.51	2.50	16.34	1.53	30.29	0.46	29.61	0.37	28.09	0.17	27.95	0.41	27.95	0.31
MnO	0.12	0.02	0.84	0.12	1.19	0.12	1.07	0.13	0.5	0.03	0.28	0.02	0.55	0.02	0.44	0.03	0.29	0.03
MgO	19.50	1.19	16.42	0.77	18.97	2.05	19.33	1.37	10.33	0.22	10.66	0.15	11.40	0.17	11.49	0.25	11.44	0.19
CaO	0.003	0.004	0.01	0.01	0.02	0.06	0.01	0.01	0.02	0.01	0.004	0.01	0.03	0.02	0.02	0.02	0.01	0.01
Na_2O	0.05	0.03	0.01	0.01	0.004	0.01	0.01	0.02	0.02	0.03	0.003	0.005	0.004	0.01	0.06	0.10	0.01	0.01
K_2O	0.02	0.01	0.04	0.02	0.03	0.03	0.04	0.07	0.04	0.01	0.03	0.02	0.02	0.01	0.06	0.02	0.07	0.08
TOTAL	84.55	0.72	85.49	0.39	85.09	0.67	86.42	0.56	87.55	0.45	86.54	0.41	86.40	0.22	86.99	0.55	86.08	0.44
Cations (O = 14)																		
Si	2.742	0.03	2.689	0.03	2.737	0.042	2.734	0.036	2.593	0.01	2.577	0.01	2.588	0.01	2.613	0.04	2.582	0.02
Al-IV	1.258	0.03	1.311	0.03	1.263	0.042	1.266	0.036	1.407	0.01	1.423	0.01	1.412	0.01	1.387	0.04	1.418	0.02
Σ tet	4.000	–	4.000	–	4.000	–	4.000	–	4.000	–	4.000	–	4.000	–	4.000	–	4.000	–
Al tot	2.715	0.05	2.752	0.06	2.693	0.082	2.731	0.046	2.875	0.03	2.890	0.02	2.887	0.02	2.887	0.04	2.910	0.03
Al-VI	1.458	0.04	1.441	0.04	1.429	0.051	1.465	0.036	1.467	0.02	1.467	0.02	1.475	0.02	1.500	0.03	1.492	0.03
Cr	0.001	0.001	0.002	0.002	0.001	0.001	0.003	0.003	0.002	0.002	0.003	0.002	0.003	0.001	0.005	0.002	0.004	0.002
Ti	0.003	0.002	0.003	0.001	0.002	0.001	0.002	0.001	0.007	0.006	0.008	0.01	0.008	0.01	0.003	0.001	0.007	0.003
Fe(2 +)	1.402	0.13	1.819	0.08	1.437	0.239	1.394	0.138	2.757	0.05	2.717	0.03	2.564	0.02	2.525	0.04	2.556	0.03
Mn	0.011	0.00	0.075	0.01	0.105	0.011	0.092	0.012	0.046	0.003	0.026	0.002	0.051	0.002	0.040	0.002	0.026	0.002
Mg	3.014	0.16	2.586	0.11	2.935	0.291	2.937	0.192	1.675	0.04	1.745	0.02	1.855	0.03	1.851	0.05	1.864	0.03
Σ oct	5.889	0.03	5.927	0.02	5.910	0.025	5.893	0.031	5.954	0.12	5.966	0.01	5.955	0.01	5.925	0.04	5.949	0.03
Oct. vacancy	0.111	0.03	0.073	0.02	0.090	0.025	0.107	0.031	0.046	0.02	0.034	0.01	0.045	0.01	0.075	0.04	0.051	0.03
Ca	0.000	–	0.001	0.001	0.002	0.007	0.001	0.001	0.003	0.002	0.000	–	0.001	–	0.003	0.002	0.000	–
Na	0.010	0.01	0.001	0.002	0.001	0.002	0.002	0.004	0.005	0.006	0.001	0.001	0.001	0.002	0.012	0.02	0.000	–
K	0.003	0.002	0.005	0.002	0.004	0.004	0.005	0.010	0.005	0.002	0.005	0.002	0.003	0.002	0.008	0.003	0.010	0.01
Fe/(Fe + Mg + Mn)	0.317	0.03	0.406	0.02	0.321	0.057	0.315	0.034	0.616	0.008	0.605	0.01	0.574	0.004	0.572	0.006	0.575	0.005
Temperatures from semi-empirical thermometers (°C)																		
Bourdelle et al. (2013)	269	31	332	45	291	40	269	33	463	57	491	41	474	64	387	69	466	86
Inoue et al. (2009)	382	37	443	30	410	38	389	41	495	17	514	9	506	17	457	59	496	36
Chl(2) – Lanari et al. (2014) 2 kb	292	32	356	44	310	39	292	34	492	57	512	36	487	54	429	65	495	80

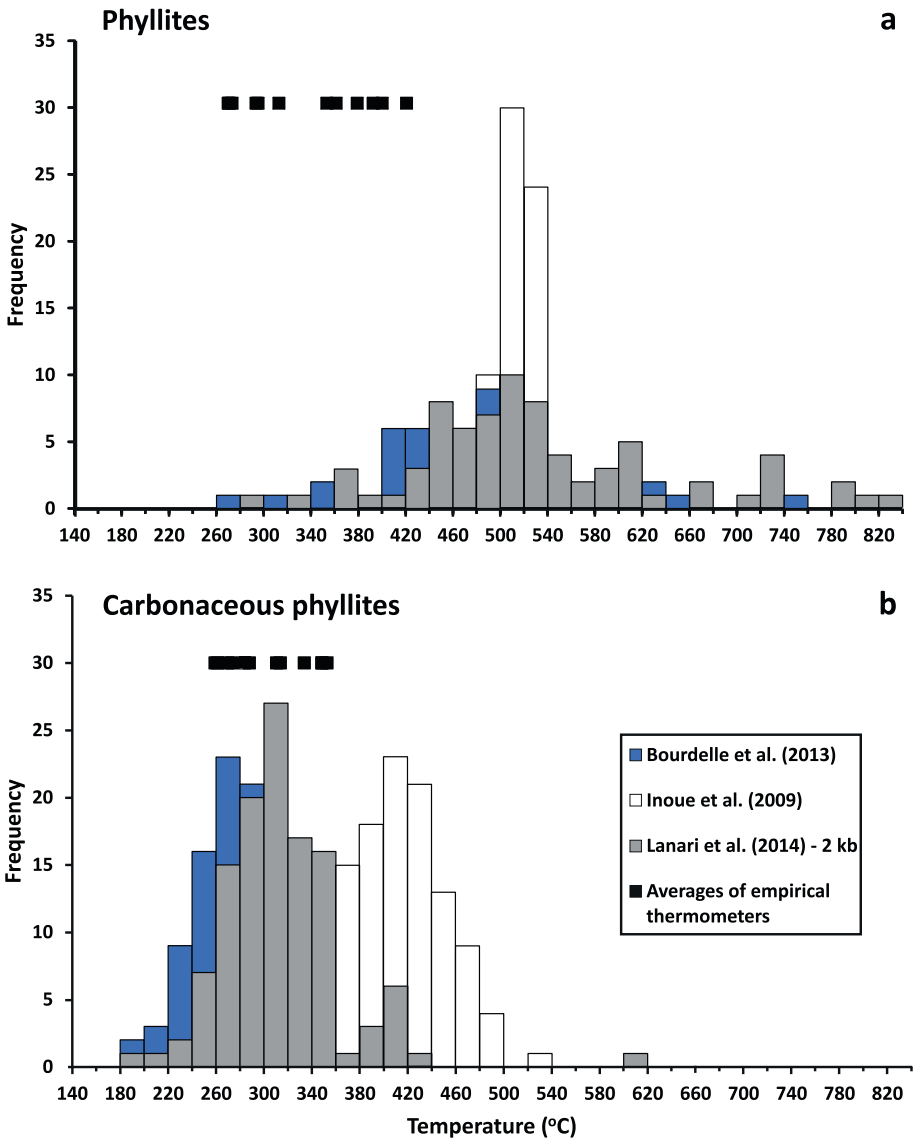

Fig. 12. Frequency histograms of chlorite temperatures estimated from semi-empirical thermometers of Inoue et al. (2009), Bourdelle et al. (2013) and Lanari et al. (2014, version Chl(2) at 2 kb) and averages of results from twelve empirical thermometers (see details in Yavuz et al., 2015). (a) results for 76 spots in five drill core samples of the PhU; (b) results for 118 spots in four drill core samples of the CPhU. Calculations were performed with all iron assumed to be Fe^{2+}. The thermometers of Bourdelle et al. (2013) and Lanari et al. (2014) are considered to be most appropriate for the Overman rocks, although calculated temperatures higher than ca. 600 °C are probably unrealistic.

Raman spectra obtained from the Overman samples generally showed a small D-band region with only the D1-band or sometimes also with very small D3- and D4-bands. Except for several spots in sample OVD-139A, the peak intensity of the D-band region is lower than that of the G-band region, which is also marked by a narrow G-band and a D2-band shoulder visible on the right-side (Supplementary Fig. S6). These features are qualitatively consistent with relatively high temperatures, roughly in the 450°-550 °C range (cf., Buseck and Beyssac, 2014). Despite the high quality of spectra obtained, about half were automatically rejected for curve fitting by the IFORS routine without an obvious explanation. Temperature estimates from the remaining measurements are around 500 °C (Table 2), confirming the evolved stage of graphitisation inferred from the spectra properties.

3.2.2.3. Validity for temperature conditions of metamorphism. Apart from peak-metamorphic temperatures, the evolution and outcome of graphitisation may also depend on other factors such as the duration of heating, lithostatic pressure, fluid activity and shear stress (Bustin et al.,

Table 2
STA-RSCM temperature estimates (UU calibration) for carbonaceous matter in drill core samples of the CPhUs in the Overman deposit. Note that temperature estimates higher than 500 °C are less accurate as the calibration curve is less robust up to 610 °C. Results obtained with the calibration of Lünsdorf et al. (2017) are given for comparison.

Sample	Depth (m)	T (C) UU calibration	1 σ	T (C) calibration Lünsdorf et al. (2017)	1 σ	n
OVD-085–5	128.85–128.95	496	31	450	36	5
OVD-093–1	150.40–150.60	564	31	503	36	3
OVD-139A	213.15–213.30	470	31	429	36	3

1995; Luque et al., 1998; Nakamura et al., 2015). Given the field and petrographic evidence for tight folding and shearing in the CPhU of the Overman deposit, the potential role of deformation is particularly relevant since shear zones may act as pathways for carbon-rich fluids from which high-crystallinity graphite can precipitate. However, the observed textural relationships favour the original presence of disseminated CM in fine-grained sediment rather than secondary introduction mediated by migrating carbon-rich fluid, although some small-scale mobility cannot be excluded, for example in rock domains affected by silicification. Tectonic shearing may also have an effect on the degree of graphitisation of primary CM but its potential role is not fully understood, since cases of an increase as well as a decrease of strain-induced crystallinity have been described in natural metamorphic rocks (e.g., Barzoi, 2015; Nakamura et al., 2015). In absence of compelling indications for a shearing effect or the presence of a local heat source, the RSCM-based results are considered to represent peak temperatures of regional metamorphism.

The limited number of spectra for each of the samples that passed the

Table 3
Averages and ranges of major and trace-element concentrations in whole-rock samples of the lithological units of the Overman prospect. A complete data set is given in Supplementary Table S3. (1): Au values are semi-quantitative due to limited amount of available sample material; (2): Calculated without extreme maximum value > 10000; <value indicates concentration below detection limit; value of 50 % of detection limit adopted for the calculation of an average.

	Chert Unit (ChU)			Carbonaceous phyllite Unit (CPhU)			Phyllite Unit (PhU)			Rhyolitic dyke (RhD)		
	Average	Min	Max	Average	Min	Max	Average	Min	Max	Average	Min	Max
	n = 25			n = 10			n = 6			n = 3		
SiO_2	95.0	85.4	98.3	68.6	57.0	85.2	61.1	56.5	69.5	70.6	69.9	71.8
Al_2O_3	0.20	<0.01	2.08	8.87	4.21	12.90	17.15	10.95	19.85	15.19	14.63	15.58
Fe_2O_3	3.53	1.19	7.57	5.56	1.99	11.60	8.66	6.79	9.94	2.72	2.66	2.82
CaO	0.01	<0.01	0.12	1.32	0.02	9.76	0.71	0.34	1.27	1.43	0.62	1.84
MgO	0.02	<0.01	0.13	1.48	0.36	2.77	3.06	2.67	3.46	0.84	0.73	0.92
Na_2O	0.02	<0.01	0.05	0.37	0.06	1.14	1.74	0.74	2.32	4.89	4.44	5.18
K_2O	0.04	<0.01	0.58	1.43	0.50	2.19	2.25	0.87	2.86	1.98	1.70	2.19
TiO_2	0.02	<0.01	0.08	0.34	0.16	0.49	0.70	0.59	0.74	0.37	0.35	0.38
MnO	0.01	<0.01	0.02	0.11	<0.01	0.42	0.11	0.03	0.17	0.03	0.03	0.04
P_2O_5	0.01	<0.01	0.07	0.04	<0.01	0.09	0.15	0.10	0.26	0.19	0.18	0.19
LOI	1.58	0.15	8.82	11.69	7.04	13.80	3.81	3.55	4.16	1.97	1.65	2.21
Total	100.5	98.5	102.4	99.8	97.3	101.4	99.4	98.2	101.1	100.2	99.5	100.6
C	0.07	0.02	0.38	6.80	4.08	8.80	0.13	0.04	0.34	0.25	0.06	0.35
S	1.46	<0.01	4.91	2.68	0.62	7.92	0.03	0.01	0.09	0.58	0.50	0.65
Ba	27	2.0	236	473	169	780	475	375	601	867	829	930
Ce	5	0.10	20	53	16	78	61	27	81	98	94	105
Cr	15	<10	50	60	30	100	160	50	210	23	20	30
Cs	0.23	<0.01	2.0	11	3.99	15	9.3	7.3	11	8.6	6.9	11
Dy	0.29	<0.05	2.1	5.2	2.9	6.7	4.3	3.2	4.9	2.2	2.1	2.3
Er	0.14	<0.03	0.84	3.2	1.8	4.0	2.5	1.9	3.3	0.75	0.58	0.84
Eu	0.12	<0.03	0.47	1.2	0.34	1.7	1.3	0.95	1.7	1.5	1.4	1.7
Ga	1.5	0.30	3.3	12	6.2	19	26	16	31	22	20	24
Gd	0.50	<0.05	3.4	5.4	2.1	7.6	4.7	3.3	5.4	4.0	3.6	4.3
Hf	0.16	<0.2	0.70	3.3	1.5	4.4	4.1	3.8	4.3	4.7	4.5	5.1
Ho	0.05	<0.01	0.40	1.1	0.63	1.5	0.87	0.61	1.1	0.32	0.29	0.38
La	2.3	0.10	11	28	7.8	41	29	12	39	48	46	51
Lu	0.02	<0.01	0.08	0.43	0.30	0.55	0.39	0.32	0.56	0.14	0.11	0.17
Nb	0.50	<0.2	4.0	6.6	2.6	8.2	8.8	7.2	12	12	7.8	17
Nd	2.2	0.05	7.7	26	7.2	38	26	15	33	38	36	40
Pr	0.54	<0.03	2.3	6.5	2.0	9.6	6.9	3.8	9.1	10	10.0	11
Rb	2.2	<0.2	29	48	17	78	103	29	131	98	80	108
Sm	0.47	<0.03	1.8	4.9	1.6	6.8	5.0	3.7	6.2	6.3	5.9	6.8
Sr	4.8	0.60	19	77	24	126	125	87	181	369	311	435
Ta	0.10	<0.1	0.30	0.46	0.20	0.60	0.63	0.50	0.80	0.83	0.70	1.0
Tb	0.06	<0.01	0.46	0.88	0.42	1.1	0.70	0.51	0.80	0.44	0.42	0.46
Th	0.18	<0.05	1.2	5.0	2.0	7.6	5.6	0.70	7.9	11	11	12
Tm	0.03	<0.01	0.08	0.46	0.32	0.57	0.38	0.29	0.49	0.11	0.09	0.15
U	0.13	<0.05	0.46	3.6	1.4	4.9	1.6	0.82	2.0	4.3	4.1	4.3
V	9.8	<5	55	86	32	131	130	98	154	37	36	37
Y	1.1	0.10	5.5	31	16	43	22	17	32	9.3	8.7	10
Yb	0.10	<0.03	0.47	2.9	1.9	3.6	2.5	2.0	3.5	0.74	0.65	0.88
Zr	5.5	2.0	25	124	51	159	139	132	152	187	171	196
Co	3	<1	20	29	11	72	29	25	32	6	6	7
Cu	13	2.0	52	253	49	737	39	17	61	26	21	35
Ni	7	0.5	54	104	49	188	97	50	120	14	13	15
Pb	3	1.0	17	13	5.0	26	5.3	<2	12	18	14	24
Sc	0.7	<1	2	9.5	5.0	15	19	13	21	4	4	4
Zn	9	1.0	36	185	20	432	104	81	123	67	62	71
	n = 11			n = 6			n = 6			n = 3		
Ag	0.07	0.01	0.26	0.32	0.17	0.67	–	–	–	–	–	–
Au (1)	2.4	<0.02	17	<0.02	<0.02	<0.02	–	–	–	–	–	–
As	898(2)	2.8	>10000	303	108	916	55	3.1	167	10	5.7	17
Bi	0.04	0.02	0.10	0.59	0.31	1.0	0.15	0.02	0.22	0.71	0.2	1.7
Cd	0.02	<0.01	0.07	0.48	0.11	1.0	–	–	–	–	–	–
Mo	0.72	0.14	3.4	4.8	3.0	7.3	–	–	–	–	–	–
Sb	2.2	0.20	7.8	6.4	2.4	18	2.0	0.68	3.1	1.1	0.41	1.6
Se	0.28	0.10	0.6	8.0	3.4	18	0.34	0.3	0.4	0.4	0.2	0.6
Te	0.27	0.03	1.6	1.1	0.36	1.8	0.07	0.04	0.09	0.40	0.08	0.7

software's threshold for processing poses limits to the precision of peak temperatures obtained. Nonetheless, overall relatively high temperatures seem a robust result when considering the data from the three samples collectively. This is a reasonable assumption because (1) the CPhU from which all of the data are derived is a relatively thin interval in the Overman sequence wherein no major gradient in regional metamorphic temperature is to be expected; (2) narrowness and relative sizes of D- and G-bands in the Raman spectra, consistent with relatively high temperatures, are ubiquitous in all three samples, also in the discarded grains; (3) use of the calibration of Lünsdorf et al. (2017) yields similar temperatures, albeit at somewhat lower levels (see Table 2).

3.3. Whole-rock geochemistry

.

3.3.1. Sample selection

Forty-six samples of the main lithological units from 31 drill cores, including two saprolite samples, were analysed for major and trace element contents using procedures given in Supplementary document S1. Cores were selected for sampling based on the presence of representative lithological intervals and to ensure sufficient geographic coverage of the Overman area (see Supplementary Fig. S1 and Supplementary Table S1), with emphasis on adequate representation of the sulphide-bearing units. Results are reported in Table 3 (averages and ranges) and Supplementary Table S3 (complete data set).

3.3.2. Major and trace element compositions

The *Chert Unit* (85.4–98.3 wt% SiO_2, n = 25) is marked by low concentrations of virtually all major and trace elements except for As, Sb, Te, and to a lesser extent S and Fe_2O_3 (Figs. 13 and 14), which tend to be relatively enriched in a substantial number of samples, apparently associated with the abundance of sulphides. Relationships between S and Fe confirm the dominance of pyrite in mineralised rock (Fig. 13b), whereas As enrichment is associated with arsenopyrite content.

Six analysed samples of the *Phyllite Unit* are compositionally fairly coherent (56.5–69.5 wt% SiO_2, Fig. 13a), showing relatively high concentrations of virtually all major oxides (e.g., Al_2O_3, MgO, Fe_2O_3, K_2O, Na_2O), in agreement with the chlorite and muscovite-rich mineral assemblage and absence of significant silicification in these rocks. Concentrations of many trace elements (e.g., Rb, Ga, Sr, LREE, V, Sc, Th, Cr, Ni, Zn) are mostly higher than in the other units, whereas those of C, S and some associated elements (Se, Te) are relatively low. The chemical signature of two samples is clearly distinct (Fig. 13), in agreement with their clayish textural appearance and origin as saprolitic weathering product. Relatively elevated concentrations of Al_2O_3, HFSE (Ti, Hf, Nb, Ta, Th, Zr, Sc) and large-ion-lithophile elements (K, Rb, Ba) likely reflect residual enrichment resulted from weathering rather than the primary composition of the *meta*-sedimentary parent rock.

The compositions of these phyllitic rocks compare well with those of *meta*-sediments elsewhere in the Armina Formation (Daoust, 2016; Naipal and Kroonenberg, 2016), notably the *meta*-siltstone/mudstones and *meta*-greywackes from the nearby north trend of the Rosebel gold deposits. Trace-element patterns show a close match with those of mudstones from the turbiditic sequence in the Koolhoven deposit (Daoust, 2016; see Supplementary Fig. S7d).

The *Carbonaceous Phyllite Unit* shows considerable spread in the contents of all major oxides, in line with the variability in main mineral constituents. The SiO_2 range (57–85 wt%; n = 10; Fig. 13a) reflects variation in the original sediment composition, density of quartz veinlets and degree of silicification. The proportions of white mica and chlorite largely determine the variations in Al_2O_3, K_2O, MgO, Fe_2O_3T contents, whereas CaO concentrations are associated with carbonate (Supplementary Fig. S7a). One deviating sample with abundant carbonate (OVD-139C) is not only anomalously rich in CaO (9.8 wt%), but also has high S, Fe_2O_3T and MnO, as well as low SiO_2, Al_2O_3, K_2O, MgO and total oxide contents.

The presence of carbonaceous matter is marked by relatively high carbon contents (up to 9 wt% C), while LOI and S are also high (up to 13.8 and 7.9 wt%, respectively). The volatiles tend to correlate positively with chalcophile trace elements and U. Plots of ratios of these elements against SiO_2 (not shown) demonstrate that these correlations are not an artefact of variable amounts of quartz. Elevated S and Fe contents are in agreement with the abundance of pyrite and other sulphides (Fig. 13b). Relative to the PhU, the CPhU rocks contain more C, S, LOI-volatiles, U, Y, HREE, Cu, Pb, Zn (few exceptions), Bi, Se, Te, and less Al_2O_3, Fe_2O_3, MgO, K_2O, Na_2O, Cr, TiO_2, P_2O_5, V, Sc, Rb, Ga.

Major and trace-element contents of the PhU samples are close to those of average Proterozoic shale (Condie, 1993), except for notable enrichment in Cr, Co, Ni and depletion in Pb, as illustrated in Supplementary Figs. S7a,b. On the other hand, the CPhU rocks tend to be lower than average Proterozoic shale in most major oxides, except for SiO_2, (variable) CaO, and as well as in Rb, Th, HFSE, Cr contents. Their HREE, Co and Ni contents are relatively high.

Normalised element patterns further highlight the compositional contrast between the CPhU and PhU, apart from the difference in abundance of carbonaceous matter. PAAS-normalised REE patterns (Supplementary Fig. S7c) show relatively flat trends and a small positive Eu anomaly for both units, but LREE tend to be more depleted relative to HREE in the CPhU. Since the discrepancies are difficult to explain by late

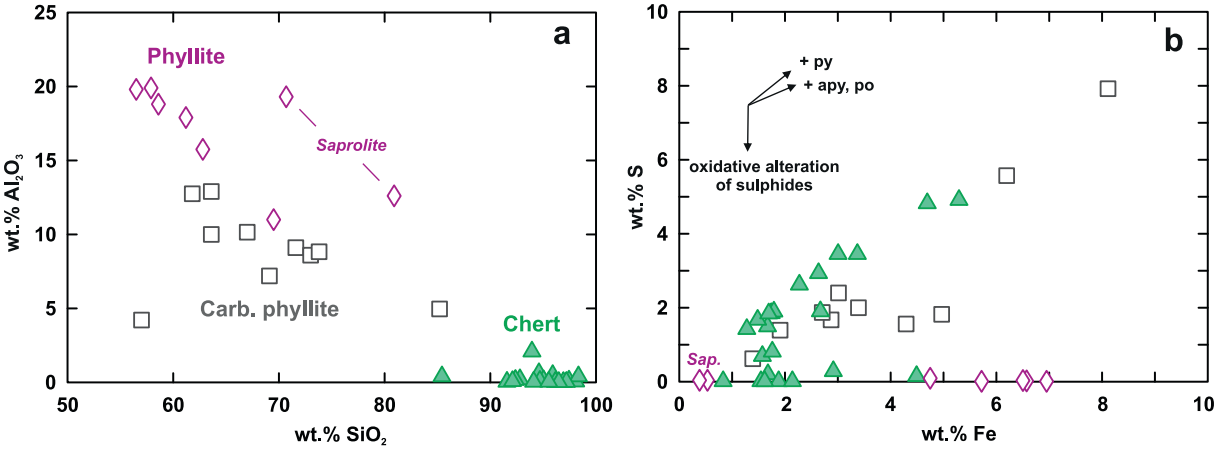

Fig. 13. Compositional signatures of *meta*-sedimentary units at the Overman deposit from drill core samples. (a) SiO_2-Al_2O_3 plot illustrating the quartz-dominant nature of the cherts and variability in unsilicified *meta*-sediments; note the shift towards higher SiO_2 contents in saprolitic phyllites; (b) Fe-S plot demonstrating the control of pyrite (py) and other sulphides (apy = arsenopyrite, po = pyrrhotite) in the cherts and part of the Carbonaceous phyllites.

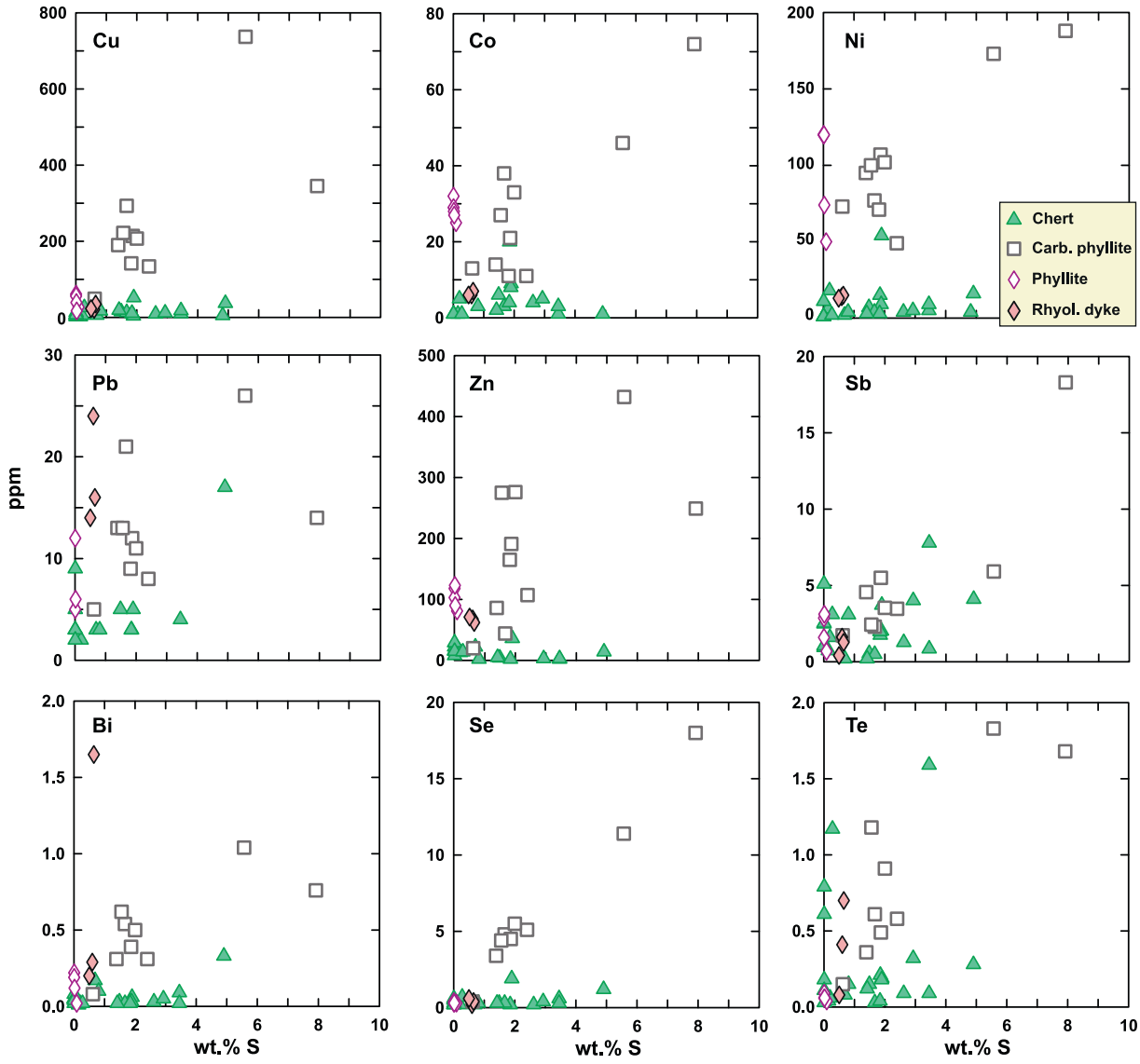

Fig. 14. Bulk-rock concentrations of S and relationships with chalcophile trace elements in main lithological units of the Overman area. Note the overall relatively low concentrations of chalcophile elements in the cherts and positive correlations with S in the carbonaceous phyllites.

hydrothermal quartz and carbonate veining in the CPhU alone, this suggest distinct provenances and/or early chemical modifications of the original sediments.

Three samples of the *Rhyolitic dyke* yielded similar results, suggesting substantial compositional homogeneity. Their signature is distinct from any other lithology in the Overman deposit, in agreement with an independent late emplacement as late crosscutting intrusion. Based on major element composition, the rock classifies as rhyolite in a TAS diagram (Supplementary Fig. S8a). Trace-element characteristics are distinct from those of other rhyolites and rhyolitic tuffs present in the south trend of the Rosebel gold deposits (Roma area, see Daoust et al., 2016). In a chondrite-normalised REE plot (Supplementary Fig. S8b) the Overman rhyolitic dyke shows a much stronger depletion of HREE relative to LREE and no Eu anomaly, whereas the Roma rhyolitic rocks are marked by a relatively flat HREE part and a negative Eu anomaly.

Sulphide mineralisation, as expressed by S content, is more extensive in the ChU and CPhU than in the PhU and RD (Fig. 14). The concentrations of most of the chalcophile elements in the CPhU are overall higher than in the ChU and tend to correlate positively with sulphur. This suggests that mineralisation processes in these two units had different compositional effects at bulk-rock scale, and were therefore probably connected to distinct events. Unlike virtually all chalcophile elements, concentrations of Co, Ni and Zn in the PhU rocks are relatively high despite very low S contents, indicating that these elements are not related to sulphide mineralisation in this unit. Concentrations of chalcophile elements in the rhyolite dyke are mostly low, with the exception of Pb.

3.3.3. *Gold distribution from exploration results*

Exploration data, made available by Rosebel Gold Mines, are based on analysis of more than 13,000 samples from ca. 150 diamond drill cores by fire assay extraction and atomic absorption spectrometry. The results indicate that highest gold grades and abundances in the Overman area are hosted in the cherts (average 0.67 g/t), whereas modest enrichments were also detected in the uppermost part of the weathering profile (laterite) and a few samples from *meta*-sedimentary intervals. Fig. 15 illustrates the spread of concentrations in composite, mostly 1–2 m long core samples for the main lithological units. Note that the subdivision, largely based on customary use by mine geologists, slightly differs from the categories adhered to in this work. Lithologies referred to as *meta*-siltstone/mudstone and undifferentiated sediments both belong to the PhU.

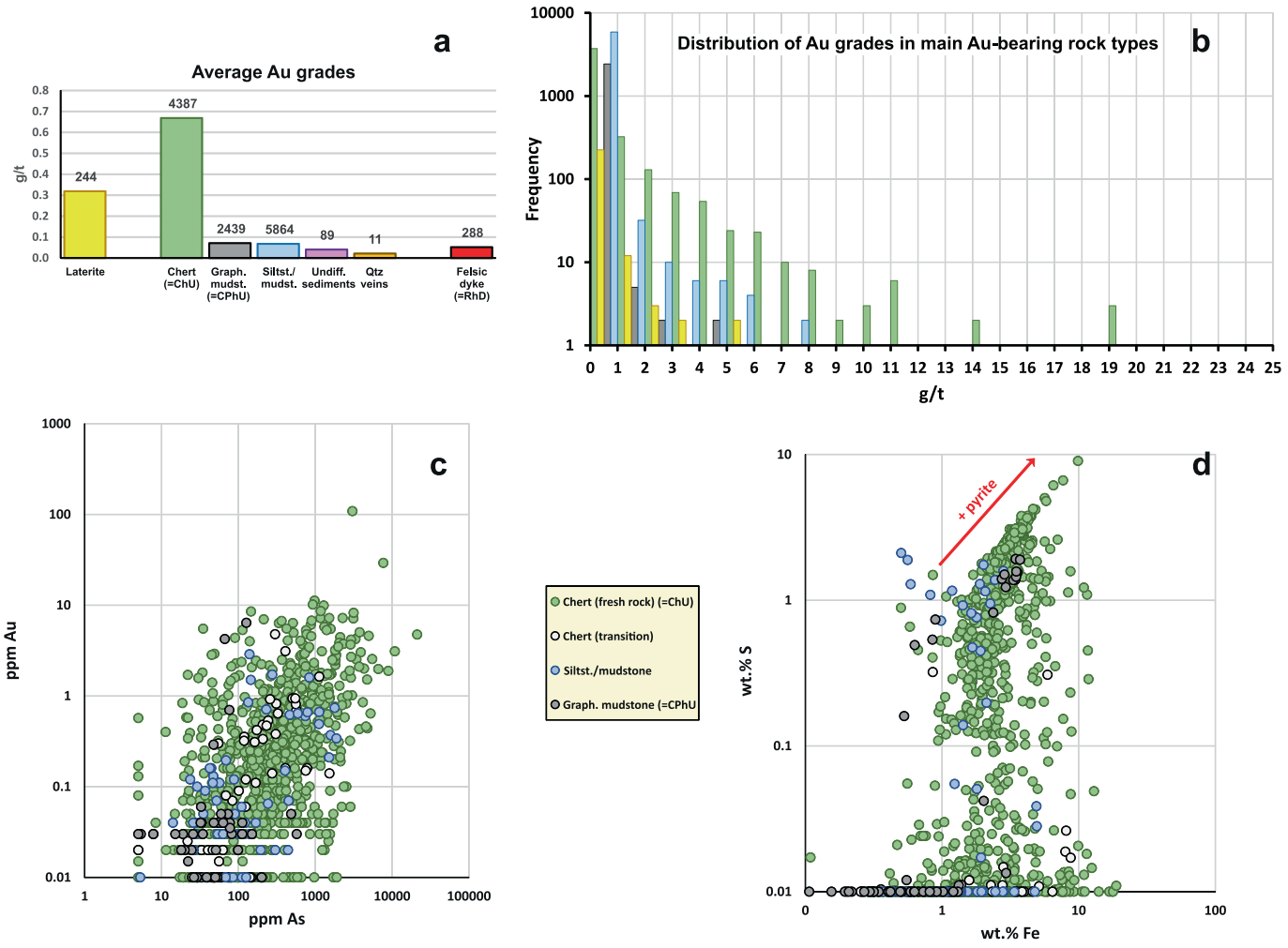

Fig. 15. Exploration results on gold distribution in composite core samples for the main Overman lithologies; rock nomenclature largely follows an original subdivision made by mining geologists. (a) average grades in the distinct lithologies showing marked enrichment in chert and to a lesser extent in laterite; (b) frequency distribution of gold grades; undifferentiated *meta*-sediments, rhyolitic dyke and quartz veins not shown because all grades fall in the 0–1 g/t bin for these rocks; note that the "laterite" label encompasses all lateritic top parts of weathering sequences sampled in the cores, irrespective of the nature of the parent-rock; (c) binary plot showing the crude correlation between Au and As contents; (d) binary plot of Fe versus S illustrating the strong control of pyrite (often accompanied by other sulphides) in fresh mineralised chert and some intervals of the carbonaceous phyllite; variation in S content reflects both the degree of primary mineralisation of the chert and some intervals in the *meta*-siltstone/mudstone and carbonaceous phyllite, as well as the effect of weathering. "Transition chert" refers to the weathering level between fresh rock and undifferentiated laterite.

The gold mineralisation is distributed throughout the cherts of the silica body, unlike the Rosebel deposits, where it is typically associated with quartz veins. Nonetheless, elevated concentrations (>1 g/t) are not homogeneously dispersed but enrichments are confined to intervals with thicknesses from ca. 1 m to several tens of meters. Such Au-rich intervals were encountered in some 70 % of the cores containing (portions of) the silica body. Commonly, the gold grades do not exceed 20 g/t but an exceptional high concentration of 109 g/t was found in a 1-meter interval of an 80 m thick chert sequence at a depth of ca. 60 m. Although gold mineralisation is most pronounced in the ChU, it locally also affected intervals of the CPhU and *meta*-siltstone/mudstone group.

According to multi-element analysis of pulps, performed on a selected set of chert intervals in 42 cores (aqua-regia extraction followed by ICP-AES spectrometry), gold concentrations tend to correlate with As (Fig. 15c), supporting the involvement of arsenopyrite in the mineralisation process. An excellent correlation between Fe and S in the freshest intervals (Fig. 15d) confirms the concomitant association with pyrite in the ore-forming mineral assemblage, as inferred from petrography. Possible relationships with S are somewhat obscured if the complete data set is considered, since the concentrations of this element tend to increase with depth due to the secondary removal during oxidative weathering of sulphides at shallow levels (roughly < 100 m). Absence of concentration-depth relationships for Au and As indicates that these elements were much less susceptible to weathering-induced redistribution. The formation of hematite apparently limited the secondary mobility of iron in the cherts. On the other hand, carbonaceous phyllites at relatively shallow depth may have experienced some iron loss, presumably because oxidation was less effective.

3.4. Zircon u-pb age dating

.

3.4.1. Samples and objective

Zircon U-Pb age dating using LA-ICP-MS was performed on a phyllite sample (OVD-142: 266.33–267.33 m) and on a sample of the late crosscutting rhyolitic dyke (OVD-136: 216–217 m) to obtain a time bracket for the gold mineralisation (see Supplementary Fig. S1 for drill core locations). Sample-preparation and analytical procedures are reported in Supplementary Material S1. Spot measurements were

Table 4
Summary of $^{207}Pb/^{206}Pb$ zircon ages for phyllite sample OVD-142 and rhyolitic dyke sample OVD-136 from the Overman deposit. Youngest seven ages of the phyllite and youngest four ages of the dyke are assumed to be best approximations of the maximum sediment deposition age and igneous intrusion age, respectively.

OVD-142					**OVD-136**				
All results					**All results**				
	spot#	**$^{207}Pb/^{206}Pb$ age**	**1 sigma**	**% disc**		**spot#**	**$^{207}Pb/^{206}Pb$ age**	**1 sigma**	**% disc**
min	2–5	2124	19	−10	min	1-2a	2021	19	−0.6
max	1-2b	2205	19	6	max	1-39b	2472	20	30
w. mean	**n**		**SE**	**MSWD**		**n**		**SE**	**MSWD**
	40/40	2171	3	1.0	w. mean	114/114	2145	2	7
95–105 % concordant					**95–105 % concordant**				
	spot#	**$^{207}Pb/^{206}Pb$ age**	**1 sigma**	**% disc**		**spot#**	**$^{207}Pb/^{206}Pb$ age**	**1 sigma**	**% disc**
min	1-3b	2149	18	−0.1	min	1-2a	2021	19	−0.6
max	2–8	2199	20	4	max	1-20b	2336	18	2
	n		**SE**	**MSWD**		**n**		**SE**	**MSWD**
w. mean	29/40	2172	3	0.5	w. mean	44/114	2099	3	4
95–105 % concordant − 7 youngest only					**95–105 % concordant − 4 youngest only**				
	n		**SE**	**MSWD**		**n**		**SE**	**MSWD**
w. mean	7/7	2157	7	0.04	w. mean	4/4	2033	10	0.3

preceded by careful inspection of cathodoluminescence (CL) images. A summary of age results is given in Table 4 and the complete set of analytical data in Supplementary Table S4.

3.4.2. *Dating results*

.

3.4.2.1. Rhyolitic dyke (RD). Separated zircons from RD sample OVD-136 are short to long prismatic (50–100 μm wide; 600–800 μm long) mostly euhedral crystals with a light pink colour. A few grains have smaller sizes (ca. 30–40 μm) and more rounded outlines. The CL images reveal the common existence of concentric, oscillatory and banded zoning as well as grains with superimposed sector zoning (Fig. 16).

A total of 120 spots were analysed. Obviously erroneous results for six of these are associated with visible inclusions or multiple cracks and were therefore discarded. Of the remaining 114 spots (in 72 grains) only 11 % (n = 12) yielded (near-) concordant (within 1 %) U-Pb ages, whereas the majority (57 %) shows substantial discordance (≤ −5% or

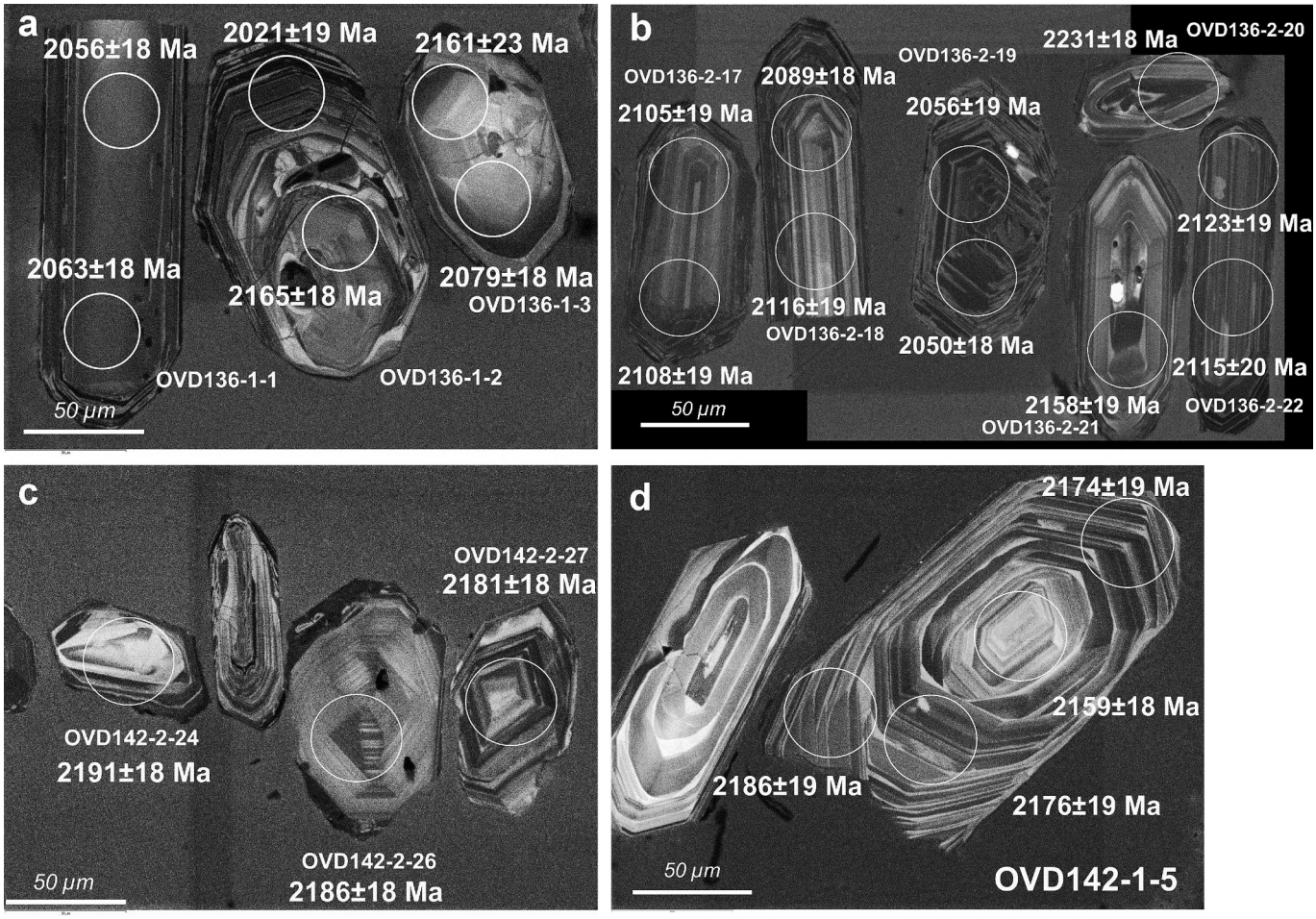

Fig. 16. Selected CL images of zircons from rhyolitic dyke sample OVD-136 (a-b) and phyllite sample OVD-142 (c-d). Indicated locations of spot measurements are 40 μm in diameter.

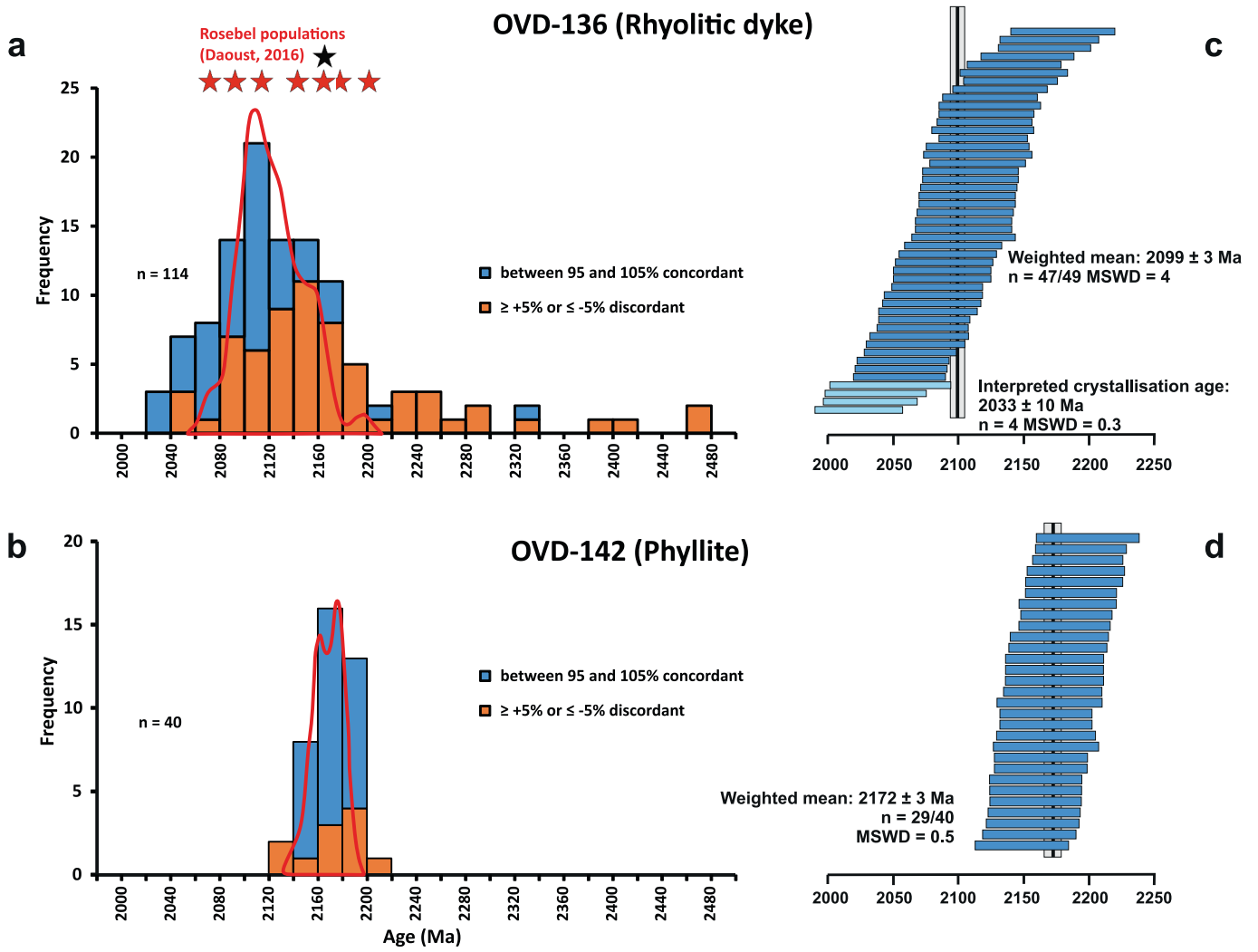

Fig. 17. Distribution of single-spot $^{207}Pb/^{206}Pb$ ages in rhyolitic dyke sample OVD-136 and phyllite sample OVD-142. a-b: Histograms (20 Ma bin width) with separate colouring for 95–105 % concordant and more discordant ages, based on the relative age difference (%) between the $^{206}Pb/^{238}U$ and $^{207}Pb/^{206}Pb$ ages. Data from the Rosebel area (Daoust, 2016), shown for comparison, include zircon age populations of *meta*-sediments (red stars) and igneous rocks (black star), as well as probability curves (red) for a *meta*-conglomerate sample from the Koolhoven deposit (in a) and a *meta*-arenite sample (in b). c-d: Age-ranked single-spot ages (95–105 % concordance only) for the group younger than 2220 Ma in the rhyolitic dyke sample (c) and the phyllite sample (d). Note that the weighted mean age of 2099 ± 3 Ma (SE) for OVD-136 does not correspond to a single geological event, since the ages are overdispersed with respect to analytical uncertainties at the MSWD value of 4. Box length represents 1σ analytical uncertainty.

≥ +5%). Significant zoning in Pb/U isotope ratios is common.

The set of $^{207}Pb/^{206}Pb$ ages with limited discordance (between −5 and + 5 %) ranges between 2021 ± 19 and 2336 ± 18 Ma, whereas ages of more discordant spots (up to 30 %) extend to 2472 ± 20 Ma (Fig. 17). The distribution of all ages younger than 2220 Ma shows a unimodal peak at ca. 2111 Ma. When ignoring the results outside 95–105 % concordance, the weighted mean of this group is 2099 ± 3 Ma (1σ, SE; n = 44/114), which is unlikely to represent a single population in view of the high MSWD value of 4 (Fig. 17). Instead, the spread in ages and the composite internal structures of many of the zircons, occasionally with rounded core parts (Fig. 16), point to non-uniform, complex crystallisation histories of individual grains. The group of 15 spots with (predominantly discordant) $^{207}Pb/^{206}Pb$ ages older than ca. 2220 Ma is considered to be derived from (parts of) grain cores that represent inherited zircons or xenocrysts, possibly entrained from rock units traversed by the rhyolitic magma. Calculated Th/U ratios are 1.0 ± 0.5 (1σ, SD, n = 106), consistent with a magmatic origin of the zircons.

3.4.2.2. Phyllite (PhU). The detrital zircons in PhU sample OVD-142 are subhedral, slightly rounded, stubby to short prismatic, light pink crystals. Largest dimensions are mostly 40–60 μm but some reach 80–120 μm. Some of the separated grains suggest to be fragments of originally larger crystals. The CL images (Fig. 16) show ubiquitous concentric oscillatory and banded zoning, mostly following euhedral shape patterns but sometimes with boundaries suggesting resorption. Of the 40 spots, analysed in 33 zircons, 11 are near-concordant (within ± 1 %). The results of only one spot exceed −5%, whereas four exceed + 8 % discordance. The weighted mean $^{207}Pb/^{206}Pb$ age of 95–105 % concordant spots is 2172 ± 3 Ma (1σ, SE; MSWD = 0.5; n = 29/40), consistent with the peak in the histogram of Fig. 17. Calculated Th/U ratios are in the range 0.38–0.73, with an average of 0.54 ± 0.08 (1σ, SD, n = 36), suggesting that the zircons are originally magmatic.

3.4.3. Regional comparison and significance

The dominant ages obtained for the zircons from both samples roughly fall in the 2.18–2.13 Ga period of tonalitic magmatism and formation of the regionally associated greenstone belt in French Guiana, i.e. in the D_1-part of the main Trans-Amazonian event of the Guiana Shield (Delor et al., 2003a,b). They are consistent with available zircon U-Pb ages from *meta*-volcanics, tonalites and *meta*-sediments of the

nearby Rosebel mining area. Investigated *meta*-arenites and *meta*-conglomerates from this area collectively define multiple Paleoproterozoic age populations between 2074 and 2202 Ma, apart from the presence of inherited Archean ages, whereas a tonalite from south of the Royal Hill deposit and a rhyolite from the Mayo deposit yielded indistinguishable upper-intercept discordia ages of 2165.3 (+2.5/-1.8) and 2164.6 (+1.5/-1.4) Ma, respectively (Daoust, 2016).

The dominant ages of the zircons from phyllite sample OVD-142 correspond both with those from these igneous rocks and with the older populations from the *meta*-sediments in the Rosebel area (Fig. 17). Given the detrital nature of the zircons, their relatively narrow age distribution points to derivation from a single homogeneous source, possibly similar igneous products exposed near the sediment basin. Considering the robustness of zircon to metamorphic resetting under greenschist-facies conditions (Pidgeon et al., 1966; Peucat et al., 1985; Mezger and Krogstad, 1997), the values obtained permit to estimate the maximum age of sedimentation (see Discussion below).

The broad range of ages found in rhyolitic dyke sample OVD-136 encompasses virtually all of the Paleoproterozoic populations of the Rosebel area. The distribution of ages younger than 2220 Ma compares well with that of a *meta*-conglomerate in the Koolhoven deposit (Daoust, 2016) and is difficult to reconcile with a single solidification event. It is assumed that only the youngest zircons provide the closest approximation of the crystallisation age (see Discussion below). Despite this limitation, the overall age relationships suggest that intrusion of the dyke occurred considerably later than emplacement of the Mayo rhyolite.

4. Discussion

4.1. Depositional environment and provenance of host sediments

Field studies in the Marowijne Greenstone Belt have interpreted the folded rhythmic alternations of metamorphic mudstones, siltstones and graded greywackes of the Armina Fmt as turbiditic (flysch-like) sedimentary sequences (Bosma et al., 1984; Gibbs and Barron, 1993; Daoust et al., 2011; Naipal and Kroonenberg, 2016). The rocks occur in close spatial association with the arenitic Rosebel Fmt in a relatively narrow E-W trending zone of depressions extending into French Guiana along the northern margin of the Guyana Shield (Ledru et al., 1994; Vanderhaeghe et al., 1998). These have been considered as pull-apart basins bordered by major faults that were affected by sinistral strike-slip movements (Ledru et al., 1991; Egal et al., 1992). According to lithostratigraphic, geochemical and age constraints, the sediments of the Armina Fmt are erosion products derived from calc-alkaline volcanics of the underlying Paramaka Formation (Bosma et al., 1984; Vanderhaeghe et al., 1998; Daoust et al., 2011), although TTG plutonic rocks and other sources locally contributed as well (Naipal and Kroonenberg, 2016). Meta-sediments with properties similar to the Armina Fmt have also been found in the greenstone region of the Karouni gold deposit in Guyana (Tedeschi et al., 2018a).

The stratigraphic relationship between the Armina and Rosebel Fmts in Suriname has long been subject to debate (Bosma et al., 1983; De Vletter, 1984). In NE Suriname, the bottom-to-top stratigraphic sequence of the volcanic-sedimentary greenstone belt is traditionally considered to be Paramaka Fmt – Armina Fmt – Rosebel Fmt (Bosma et al., 1983, 1984; De Vletter, 1984; Gibbs and Barron, 1993; Daoust et al., 2011; Kroonenberg et al., 2016). The Armina and Rosebel Fmts both unconformably overly the folded *meta*-volcanics and associated lithologies of the Paramaka Fmt, and presumably share elevated domains of these rocks as main source of the sediments. Bosma et al. (1984) interpreted the Armina-Rosebel boundary as a major unconformity despite the lack of direct field evidence, since contacts between the formations are nowhere exposed and a strict lithological distinction is problematic (Naipal and Kroonenberg, 2016; Daoust, 2016). The presence of phyllite pebbles in Rosebel conglomerates could be taken to support an intervening period of uplift and metamorphism (Bosma et al., 1983), but these may well be derived from the Paramaka Fmt (Gibbs and Barron, 1993), given an increase in phyllitic intercalations towards its top (Kroonenberg et al., 2016). Other circumstantial indications come from schistosity patterns suggesting distinct deformation histories, the hypothesis of the Rosebel Fmt as a molasse-type sequence (Bosma et al., 1983), local features in areas with thick accumulations of volcaniclastic products (Gibbs and Barron, 1993) or inferences on sediment maturity and provenance from major-element compositions (Naipal and Kroonenberg, 2016).

From the absence of field evidence for an unconformity in the Rosebel gold mining district (RGM), drill-core petrography, sedimentological observations, general geological constraints and age dating on detrital zircons (see below), Daoust (2016) inferred that the sediments of both formations were deposited in a single basin, showing a gradual lateral facies transition from terrestrial and shallow marine environments (alluvial-fluviatile-littoral-deltaic) in the South to deep marine environments (hemipelagic, turbiditic) in the North (Fig. 18). This change in depositional environment is expressed by a shift from predominant medium to course-grained arenites and conglomerates (Rosebel Fmt) to finer-grained greywackes, siltstones and mudstones (Armina Fmt) in the same direction. Other petrographic and geochemical considerations also favour a gradual rather than sharp transition in the RGM (Naipal and Kroonenberg, 2016).

The Koolhoven and J-Zone gold deposits in the northernmost mineralised trend of the RGM (Fig. 2) are hosted in a sequence largely consisting of alternating siltstone, mudstone and greywacke beds, typical for a relatively deep marine, turbiditic environment (Daoust et al., 2011; Daoust, 2016). The phyllitic units of the Overman area, situated some 16 km further north, fit into this depositional facies scheme, as the predominantly fine-grained nature of the original sediments corresponds to that of distal members of turbidite beds deposited in deep parts of the marine basin. The intervals with abundant organic matter were likely deposited in secluded low-energy environments or during periods of repose in turbidite sedimentation.

According to petrographic analysis, the turbiditic wackes and conglomerate clasts from this northern RGM trend are typically arc related and derived from mafic to felsic volcanic sources (Watson, 2008). Geochemical signatures of the entire package of clastic sediments in the RGM confirm a subduction-related setting, showing no significant differences between turbiditic (Armina Fmt-type) and arenitic (Rosebel Fmt-type) sequences (Daoust et al., 2011). Trace-element signatures of the Overman phyllitic units are not only similar to those of the northern trend (Supplementary Fig. S7d) but also to the arenites, greywackes and mudstones in the RGM in general, as primitive-mantle normalised trace-element patterns illustrate (Fig. 19). In addition, there is a remarkable correspondence with the intermediate and felsic volcanic rocks, which show the typical compositional features (e.g., negative Nb and Ta anomalies) of subduction-related, calc-alkaline magmatism. These chemical similarities suggest that predominantly intermediate-felsic volcanics, generated at a convergent plate boundary, were a common source of all the clastic sediments in the Overman-Rosebel area, which lends further support for the hypothesis that the Armina and Rosebel formations represent complementary distal-proximal sediment facies deposited in the same basin.

This single-basin interpretation contrasts with prevailing concepts for French Guiana where fluvio-deltaic (Rosebel-like) sediments are thought to overly flyschoïd (Armina-like) units (Ledru et al., 1994). It should be noted, however, that lateral stratigraphic correlations with Surinamese equivalents are problematic (e.g., Ledru et al., 1991) due to variability of sediments and intercalated *meta*-volcanics within both Armina-type and Rosebel-type sequences, the frequently tectonised nature of contacts, and ill-defined distinction from other lithologies such as phyllites of the Paramaka Fmt. Facies differences and provenance variations across the Armina Fmt in NE Suriname (Naipal and Kroonenberg, 2016) hamper correlation attempts. Further studies are necessary to solve this issue.

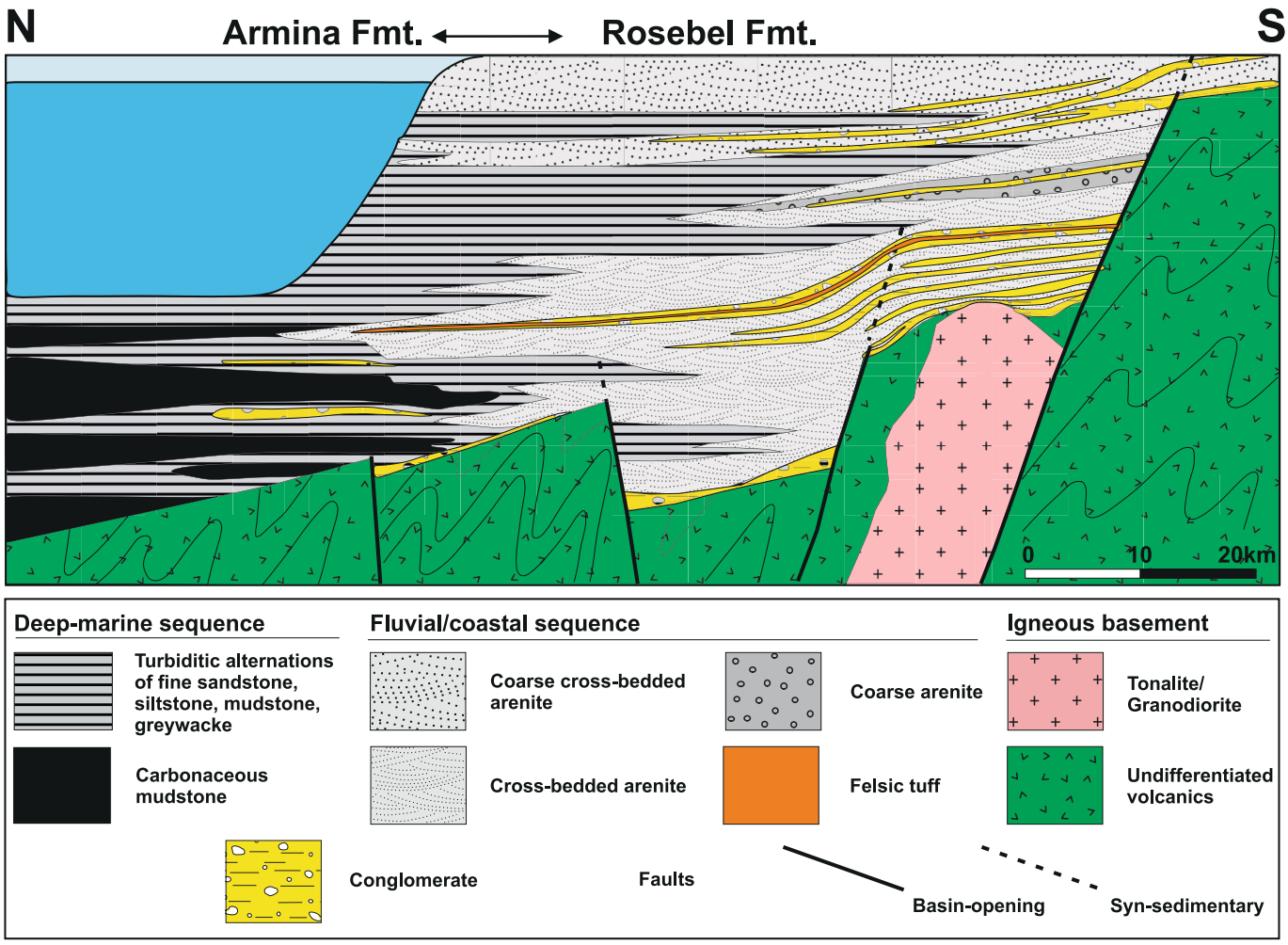

Fig. 18. Schematic illustration of the Paleoproterozoic *meta*-sediments in the Rosebel-Overman area, depicting the boundary between the Armina and Rosebel formations as lateral facies transition from terrestrial to deep marine depositional environments prior to deformation and metamorphism (largely after Daoust, 2016). Vertical dimensions not to scale. Note that according to earlier interpretations the formations (and their equivalents in French Guiana) are separated by an unconformity (e.g., Bosma et al., 1984; Milési et al., 1995; Delor et al., 2003a,b).

The Overman gold deposit is part of a package of metamorphic distal turbidites associated with *meta*-sediments rich in carbonaceous matter, is marked by enrichment in arsenic, and is situated in a stratigraphic domain affected by shearing. Hence, if the collective set of criteria is applied, it can be categorised as a turbidite-hosted orogenic deposit (cf. Berge, 2011). Gold deposits of the Merian district that also reside in the Armina Fmt (Ribeiro et al., 2009; Kioe-A-Sen et al., 2016) equally classify as turbidite hosted. However, a conspicuous atypical feature at Overman is that mineralisation is centred in the intercalated, tectonised chert body, which facilitated pathways for gold-bearing fluid.

4.2. Zircon U-Pb constraints on the deposition age of host sediments and regional Trans-Amazonian orogenetic framework

The youngest detrital zircons in phyllite sample OVD-142 provide an estimate of the maximum deposition age of the turbiditic Armina sediments at the Overman location. When considering only $^{207}Pb/^{206}Pb$ ages within 95–105 % concordance limits (n = 29/40, see Fig. 17), the single youngest zircon yields an age of 2149 ± 18 Ma. The mean of seven youngest zircons (ranging between 2149 ± 18 and 2159 ± 18 Ma) gives 2157 ± 7 Ma (1SE, MSWD = 0.04; Table 4). From these results, an approximate maximum deposition age of 2.15 Ga is adopted for the OVD-142 sediment. Detrital zircons from a *meta*-conglomerate in the nearby Koolhoven gold deposit (Fig. 2), also thought to be part of the turbidite sequence, show a large age overlap with the phyllite zircons but extend towards considerably younger values (Fig. 17). The average of 2094 ± 9 Ga for a group of six youngest zircons (90–110 % conc.) is interpreted as maximum deposition age for this layer (Daoust, 2016). The age range of zircons in four samples of *meta*-arenite and *meta*-conglomerate from the adjacent arenitic sequence in the RGM (Rosebel Fmt) is fairly similar to that of the Koolhoven conglomerate (Fig. 17). From the youngest zircons, a value of 2076 ± 6 Ma has been accepted as maximum deposition age of these sediments (Daoust, 2016).

The widespread in zircon $^{207}Pb/^{206}Pb$ ages between 2021 ± 19 and 2180 ± 20 Ma (95–105 % concordance; n = 47/114, excluding two isolated older ages) from rhyolitic-dyke sample OVD-136 implies that many of the analysed zircons were inherited from the partially molten protolith and/or were entrained from *meta*-sedimentary wall-rock. Hence, only the youngest zircons and overgrown margins are taken to approximate the crystallisation age. A mean value of 2033 ± 10 Ma (1SE, MSWD = 0.3) from the subgroup of four youngest zircons (ranging between 2021 ± 19 and 2048 ± 24 Ma; Table 4, Fig. 17c) is adopted here. Given the crosscutting relationship with the host rock, this age is considered to represent the minimum deposition age of the Armina sediments at the Overman deposit.

Fig. 20 shows the evolution of the auriferous Overman-Rosebel sediments in the timeline of the Trans-Amazonian orogenetic stages, which follows a slightly modified version of the schemes of Delor et al.

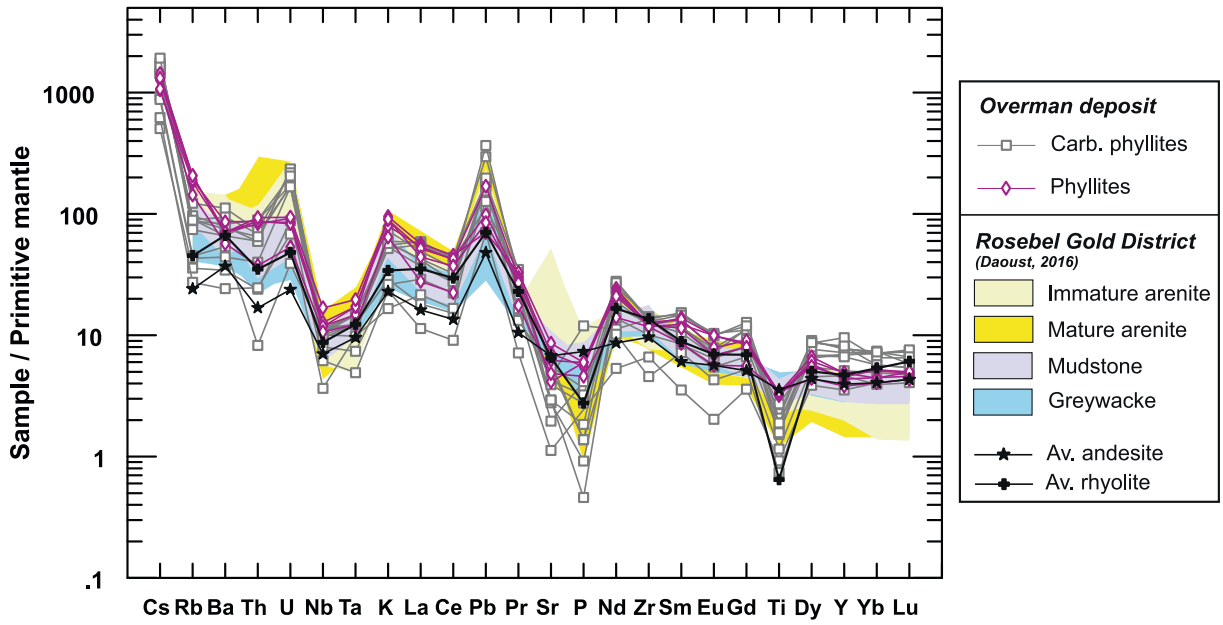

Fig. 19. Primitive mantle normalised trace-element patterns (Sun and McDonough, 1989) patterns of phyllitic host rocks of the Overman deposit in comparison with those of *meta*-sediments and *meta*-volcanic rocks of the adjacent Rosebel Gold District (Daoust, 2016). The overall correspondence and shape of the trends suggest that all the clastic sediments were derived from a common calc-alkaline volcanic source in a subduction setting.

(2003b) and Daoust (2016) for Rhyacian events, largely derived from an interpretation of U-Pb zircon ages of igneous and sedimentary rocks in French Guiana (FG) and the RGM, respectively, and a compilation of zircon ages from Surinamese igneous rocks (Kroonenberg et al., 2016) for Orosirian events. A recent summary of the chronology of events during the Trans-Amazonian orogenic evolution of the Guiana Shield, based on a compilation of published U-Pb zircon age dates, is given in Tedeschi et al. (2020).

Deposition of predominantly terrestrial sediments of the Upper Detrital Unit (UDU, largely equivalent to the Rosebel Fmt in Suriname) is thought to have occurred in a string of pull-apart basins running roughly E-W in the northern parts of French Guiana and Suriname (Ledru et al., 1991; Egal et al., 1992). The basin-opening tectonics demarcate the D_{2a} stage of the Trans-Amazonian orogeny and are inferred to have been accompanied by granitoid plutonism. Zircon dating of intrusions in west and south FG has been used to derive an approximate time window of 2.11–2.08 Ga for this stage (Delor et al., 2003a). Youngest reworked zircons from UDU sediments suggest a maximum deposition age of ca. 2.12 Ga (Ledru et al., 1991 in Milési et al., 1995; Delor et al., 2003a), whereas a minimum limit of ca. 2.08–2.06 Ga has been inferred from zircon-dated granitoids showing a thermo-metamorphic imprint or a crosscutting relationship (Milési et al., 1995; Delor et al., 2003a). The deposition interval in FG thus has a much earlier maximum boundary than that inferred for the Rosebel Fmt in the RGM area where the youngest detrital zircons are some 40 Ma younger.

The deposition age of the Armina Fmt is poorly constrained. According to a widely held view, the Armina Fmt in FG is tightly related to Paramaka (Paramaca) rocks, forming greenstone-belt sequences with a common history of deformation and metamorphism during the Trans-Amazonian D_1 phase (e.g., Milési et al., 1995; Vanderhaege et al., 1998; Delors et at., 2003a,b). The flysch-type sequences are considered to unconformably overly and thus be younger than the Paramaka Fmt of which acid to intermediate extrusive rocks in the northern and southern greenstone belts have been dated between 2.14 and 2.16 Ga (Lafrance et al., 1999; Delor et al., 2003a; Enjolvy, 2008). From zircon ages of a crosscutting granite and pegmatite in the Yaou area (southern belt in FG), Milési et al. (1995) proposed a minimum age of ca. 2.13 Ga for the Paramaka Fmt, in agreement with the youngest zircon age (Pb evaporation) of 2137 ± 6 Ma obtained on a *meta*-andesite in central FG (Delor et al., 2003a). This maximum age limit for the deposition interval of Armina-type sediments in FG is thus not in conflict with the (older) minimum age (2149 ± 18 Ma) of detrital zircons in the Overman phyllite, but those from the Koolhoven conglomerate in the RGM area suggest that sedimentation started here not earlier than 2.09 Ga (Daoust, 2016). Preliminary dating results for detrital zircons from other Armina locations in NE Suriname (e.g., Armina Falls, see Naipal and Kroonenberg, 2016) show youngest ages of ca. 2.09 Ga, which would support this late start of sedimentation (Mason et al., 2022). Dated igneous intrusions provide a minimum age limit but available data are scarce. The Petit Saut monzogranite in northern FG, intruded in Armina-like *meta*-pelite, yielded a zircon U-P discordia age of 2060.0 ± 4.1 Ma (2σ, ion probe; Delor et al., 2003a), whereas preliminary LA-ICPMS zircon ages of crosscutting syn- to post-collisional two-mica granites in NE Suriname suggests a minimum age around 2.06–2.04 Ga (unpublished data Utrecht Univ.). These dating results for granitoid intrusions would imply a slightly older minimum limit for the deposition of Armina sediments than the ca. 2.03 Ga intrusion age of the Overman rhyolitic dyke.

Taking uncertainties in these intrusion ages into account, the minimum deposition ages of Armina and Rosebel Fmts in Suriname and their analogues in French Guiana are approximately similar and fall in the D_{2b} stage (Fig. 20), whereas maximum age limits are insufficiently constrained for a reliable comparison.

4.3. Conditions of metamorphism

The RSCM temperatures obtained for the Overman carbonaceous phyllites are some 200 °C higher than the temperatures inferred from chlorite thermometry, based on the semi-empirical approaches of Bourdelle et al. (2013) and Lanari et al. (2014). Such considerable discrepancies between RSCM- and chlorite-based geothermometry are not exceptional, and signal that co-existing mineral phases do not necessarily record the same metamorphic conditions or event (Barzoi, 2015; Grosch, 2019; Pérez-Cáceres et al., 2020). Higher RSCM temperatures than inferred from chlorite thermometry are common (e.g., Pérez-Cáceres et al., 2020) since carbonaceous matter usually tends to retain the maximum temperature, whereas chlorite is susceptible to re-equilibration during retrogression (e.g., Bourdelle et al., 2013). On the

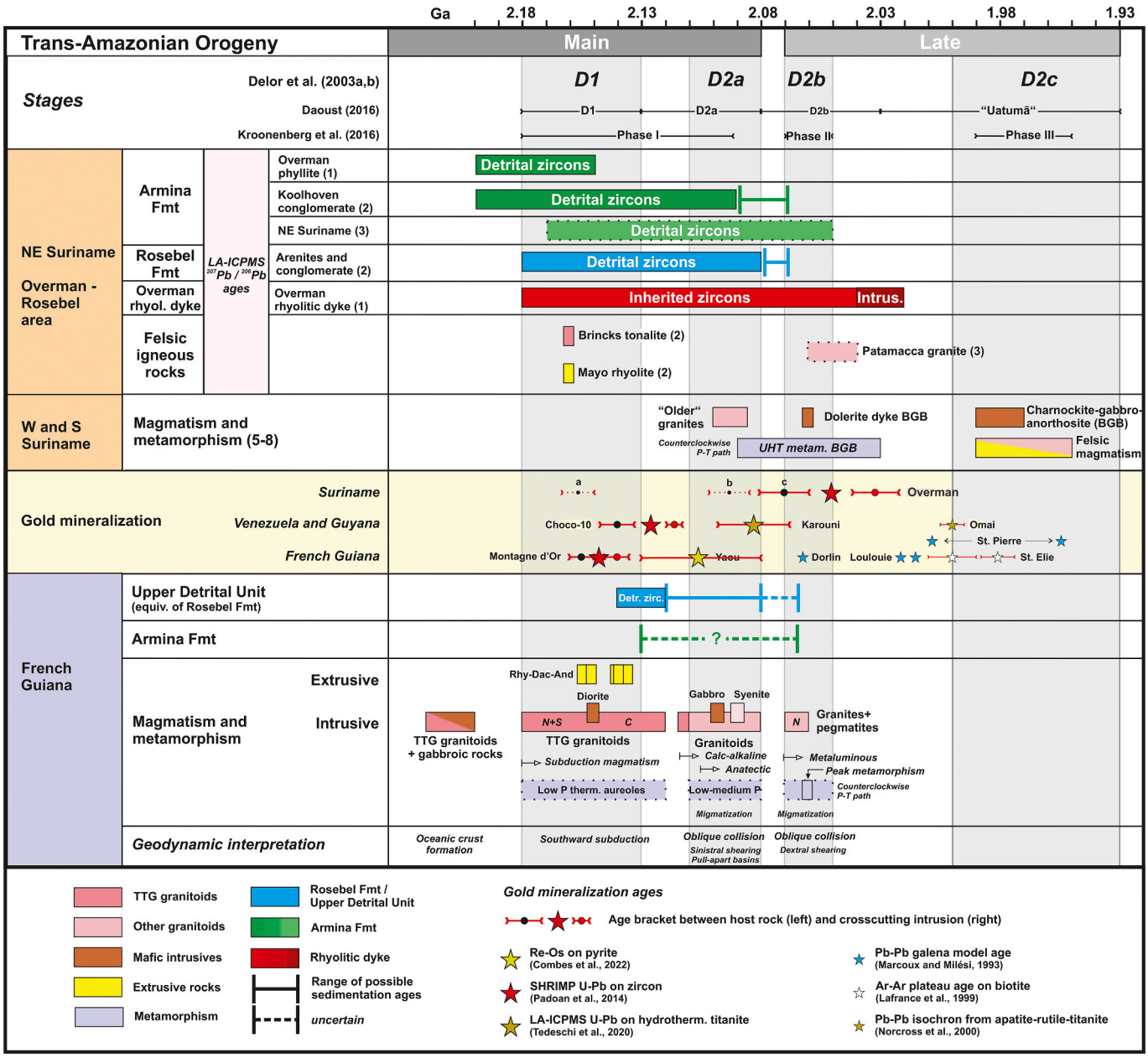

Fig. 20. Schematic timeline for main geological events (deposition of host sediments, metamorphism, magmatism and gold mineralisation) in the Overman-Rosebel area and north-east Suriname at large during the Trans-Amazonian orogeny, together with radiometrically dated magmatic activity and metamorphism in west and south Suriname, the largely corresponding sequence of events in French Guiana, and mineralisation ages of gold deposits in the Guiana Shield. Stage subdivision for the Trans-Amazonian orogeny largely according to Delor et al. (2003a,b). Gold mineralisation ages indicated with large symbols are considered to be more reliable than those with small symbols. Maximum age brackets shown for the Overman deposit based on maximum deposition age of host sediment as defined by zircon U-Pb ages for (a) local phyllite sample (this work), (b) Armina *meta*-sediments in NE Suriname (Mason et al., 2022), and (c) Rosebel-Armina *meta*-sediments in the adjacent Rosebel mining area (Daoust, 2016). Sources of data not mentioned in the legend: (1) this work; (2) Daoust (2016); (3) Mason et al., (2022); W and S Suriname – De Roever et al., (2015, 2019); Klaver et al. (2015a,b); Kroonenberg et al. (2016) and references therein; French Guiana – Ledru et al. (1994); Milési et al. (1995); Vanderhaeghe et al. (1998); Delor et al. (2003a,b).

other hand, inconsistencies could also result from the influence of strain on the crystallinity of graphitic carbonaceous matter (Barzoi, 2015; Nakamura et al., 2015).

The RCSM estimate of ca. 500 °C for the phyllites of the CPhU likely records the maximum temperature in the metamorphic history of the rock unit, since it is grossly consistent with the conditions inferred for the adjacent PhU, for which chlorite temperatures centre on 475 °C. The lower chlorite temperature of ca. 300 °C can be attributed to re-equilibration during the subsequent shearing event (see below), a well-established phenomenon in retrograde greenschist-facies ductile shear zones (e.g., Wallis et al., 2015; McAleer et al., 2017). Conceivably, this is associated with *syn*-kinematic ingress of fluids that produced the observed veinlets of quartz and/or carbonate together with one of the sulphide generations. Given the relative scarcity of these features in the Phyllite Unit, this may have escaped significant retrogression due to more limited permeability. Nonetheless, the large scatter in chlorite temperatures obtained from samples of this unit (Fig. 12) may well reflect some re-equilibration in response to small-scale localisation of shear strain (e.g., Steffen and Selverstone, 2006).

The maximum temperature of ca. 500 °C recorded in the CPhU is in

agreement with the metamorphic evolution inferred for the northern part of the Guiana Shield. Metamorphic conditions in the greenstone belts of Suriname and French Guiana during D_1 and D_2 range from the greenschist facies (muscovite-chlorite assemblage) to the medium amphibolite facies (biotite ± garnet) at low to medium pressures (Delor et al., 2003a,b). The relatively high grades have been linked to the emplacement of abundant TTG and granitic intrusions throughout the D_1-D_2 period (Milési et al., 1995; Delor et al., 2003a).

The metamorphic assemblages of the folded *meta*-greywackes and phyllites of the turbiditic *Armina Fmt* in NE Suriname are mainly composed of chlorite-muscovite ± biotite ± garnet or chloritoid (Bosma et al., 1983, 1984; Kroonenberg et al., 2016). Staurolite-garnet-mica schists (Taffra Fmt) with occasional kyanite, andalusite or fibrolite, forming an envelope around muscovite-biotite granites (Patamacca), are considered to be higher-grade thermo-metamorphic equivalents of the Armina Fmt (Bosma et al., 1983), in line with observations in adjoining FG (Delor et al., 2003a), but stratigraphic relationships are ambiguous (Kroonenberg et al., 2016). Peak metamorphic conditions of staurolite-garnet bearing micaschist on the FG side of the Marowijne River have recently been determined at 600 ± 50 °C and 0.48 ± 0.1 GPa (Plunder et al., 2022).

Greenschist-facies metamorphism of the *meta*-arenites and conglomerates of the *Rosebel Fmt* is consistent with assemblages of sericite-chlorite-(clino)zoisite and locally chloritoid observed in intercalated phyllitic *meta*-siltstones and slates (Bosma et al., 1984). The occasional presence of andalusite, kyanite or chloritoid has been reported from various locations of the corresponding Upper Detrital Unit in FG (Milési et al., 1995).

A counter-clockwise evolution P-T path during the D_2 event has been interpreted for the *meta*-sedimentary formations, based on kyanite post-dating andalusite (Vanderhaeghe et al., 1998; Delor et al., 2003a). The latter authors proposed a prograde P-T trajectory into the stability field of andalusite up to some 550 °C and 0.4 GPa during burial of the UDU in northern FG during D_{2a}, followed by isobaric cooling towards the kyanite stability field during D_{2b}. Approximately similar maximum conditions have been inferred from staurolite-bearing kyanite quartzites in a narrow schist–quartzite zone of the Paramaka Fmt between the Rosebel Fmt and Taffra schists in NE Suriname (Bijnaar et al., 2016). Rosebel Fmt rocks along the FG side of the Marowijne River also record comparable peak metamorphic conditions of 500 ± 50 °C and 0.4 ± 0.1 GPa (Plunder et al., 2022).

4.4. Deformation history

The structural framework and micro-textures within the lithological units provide insight into the role of deformation as important control of mineralisation at Overman. The WNW-ESE striking stratigraphic units and dominant structures with an overall sub-vertical to steeply SSW dipping orientation at deposit scale, together with the repetition of the Paramaka *meta*-volcanics and Armina *meta*-sediments (Fig. 2) and sub-parallel axial planar foliation and shear faults, are consistent with a cycle involving initial folding in a compressional regime, followed by the formation of shear zones under transpressional conditions, as inferred for the adjacent northern domain in the RGM (Daoust, 2016). The discernible structures suggests that bedding and dominant foliation of the phyllitic units were transposed into the main regional penetrative fabric. Dextral strike-slip components tend to prevail in the late shear zones. Daoust et al. (2011) interpreted the structural architecture of the RGM in terms of a dextral Riedel system formed during a simple-shear event.

Microtextures in core samples of the phyllitic units at the Overman deposit (Fig. 21a-f, see also Fig. 10) agree with a succession of two different styles of deformation: an early folding phase (D_{1OV}), followed by a phase of ductile shearing (D_{2OV}) that overprinted the pre-existing structures. The folding phase, typically marked by alignments of chlorite and white mica, was complex, since re-folding of an early foliation (S_{1OV}), often oriented approximately parallel to primary stratigraphic lamination, produced tight micro-folds locally associated with a crenulation cleavage (S_{2OV}). Folds in more competent layers, generally rich in quartz, tend to have a more open character.

Structures belonging to this early folding phase (D_{1OV}) are preserved best in domains affected by little or no shear strain, since the overprinting shearing phase (D_{2OV}) also created folds by drag (Fig. 21f) or through instabilities in newly-formed, shear-related foliation planes (cf., Carreras et al., 2005). This complication is most apparent in the CPhU where micro-scale rheological heterogeneity is prominent due to the localised presence of quartz in thin layers, veins and silicified areas. Domains wherein laminae of carbonaceous matter show tight micro-folds and crenulation foliation despite being surrounded by abundant re-crystallised micro-quartz (Fig. 21a-d), suggest that previously existing, ductily deformed phyllosilicates were entirely silicified after the main folding phase. Anastomosing micro-shear planes are often lined by (graphitised) carbonaceous matter, apparently mobilised from originally stratiform laminae, which further promoted ductile shearing (Oohashi et al., 2013; Kaneki and Hirono, 2019).

Structures in the chert body are predominantly related to the D_{2OV} shearing phase as testified by fracturing, foliation development and flattening of clasts at drill core scale (e.g., Fig. 6). Variations in the intensity of foliation reflect gradients in the distribution of strain. Microstructures in thin sections show abundant evidence of shear-induced dynamic recrystallisation of micro-quartz such as parallel orientation of elongated recrystallised grains, grain-size reduction (often down to < 50 μm), bulging grain-boundaries and formation of subgrains (Fig. 21 k-q). These features are consistent with a deformation regime operating at a temperature between ca. 300 and 400 °C (e.g., Stipp et al., 2002), in agreement with the post-peak metamorphic conditions discussed above.

4.5. Microscopic evidence for the timing of sulphide and gold mineralisation relative to deformation

In the *Chert Unit*, the distribution of sulphides at thin-section scale, both randomly disseminated and aligned along trails, suggests *syn*-shear introduction of the mineralising fluids along boundaries of dynamically re-crystallizing quartz grains, as well as along networks of straight to curvilinear micro-fissures and shear planes (Figs. 6-8, 21k-q). Uneven sulphide distributions in different sample domains are often associated with heterogeneity in the quartz fabric, apparently determined by the original mineralogy and texture prior to silicification, the presence of veinlets and spatial variations in shear-induced strain. The dominant habit of pyrite in anhedral microcrystalline aggregates is attributable to recrystallisation and grain-size reduction of precursor grains during continued D_{2OV} deformation. Post-mineralisation shearing resulted in elongated arrangements of small pyrite crystals and aggregates in trails, whereas deformation effects on crystals in low-strain domains seem to be limited to in-situ fracturing only (Fig. 21 k-n). Strain shadows with fibrous quartz, grown perpendicular to euhedral crystal faces of pyrite, are also indicative of mineralisation before deformation had ended (Fig. 21p). In rare cases, euhedral pyrite with no optical signs of deformation appear to have overgrown aggregates of earlier fractured and recrystallised crystals (Fig. 21q), thus representing a subordinate post-shear population.

In the *Carbonaceous Phyllite Unit*, pyrite and associated sulphides (arsenopyrite, chalcopyrite, sphalerite, pyrrhotite) are mostly associated with folded or boudinaged domains of recrystallised quartz (veins, lenses, silicified layers). Textures favour a structural relationship with the late crosscutting shear-related foliation. The formation of matrix pyrite post-dated the main D_{1OV} folding phase as well, as suggested by crenulated inclusion trails preserved in core parts of porphyroblasts and by absence of an obvious relationship with the S_{1OV} or S_{2OV} foliation (Figs. 10a-d, 21a-f).

Curving of shear foliation around large sulphide porphyroblasts and frequent occurrence of strain shadows consisting of quartz and/or

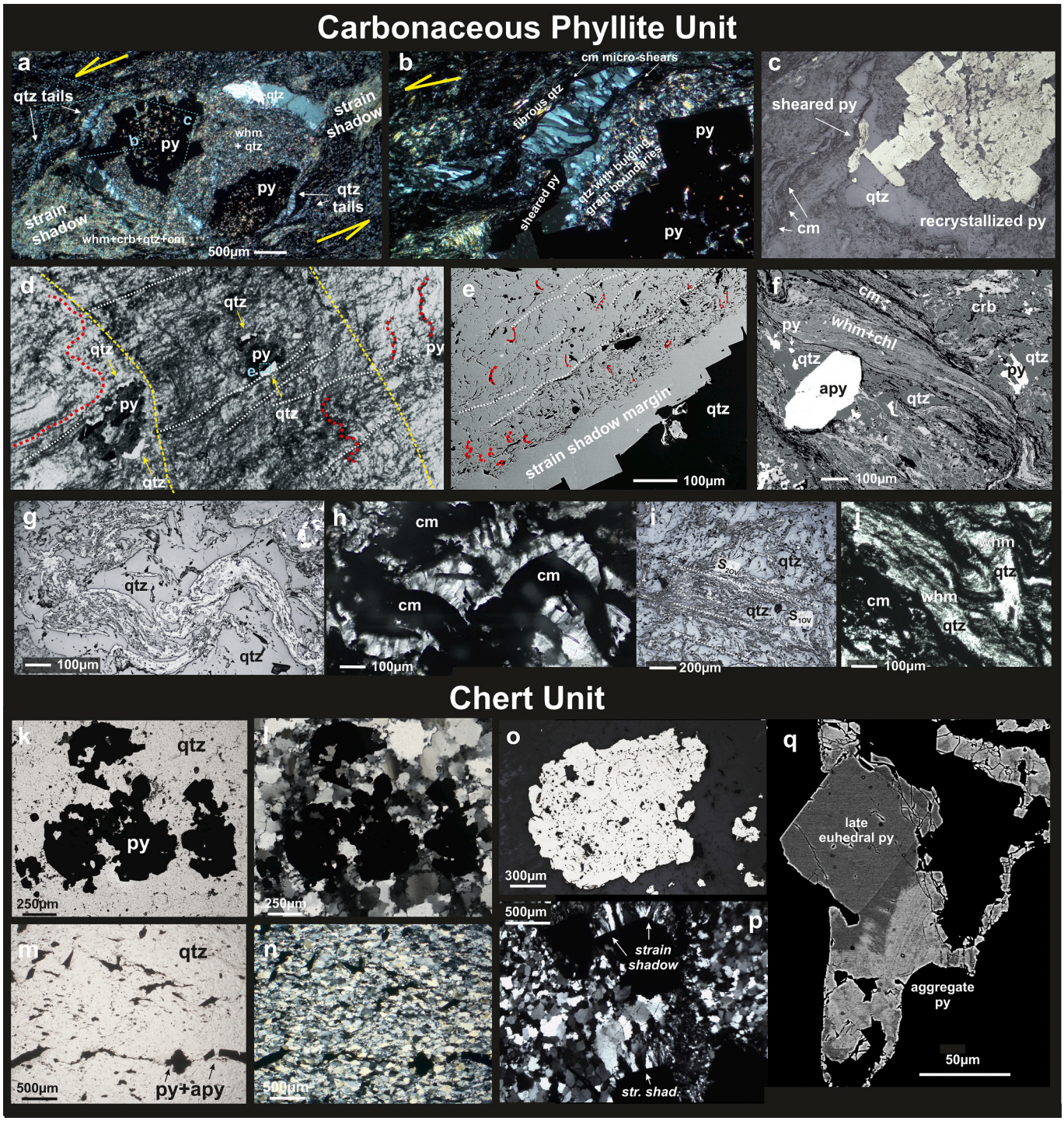

(caption on next page)

Fig. 21. Microtextural expressions of chronological relationships between sulphide mineralisation, deformation, metamorphism and silicification in CPhU and ChU samples, shown in optical microscope images in XPL (a, b, h, l, n, p), PPL (j, k, m) and RL (c, g, i, o), thin-section scan in PPL (d) and BSE images (e, f, q); (a) porphyroblastic assembly of pyrite, which acted as a stiff object during ductile shear of the matrix (whm-chl-cm-minor qtz); strain-shadow domains consist of whm + qtz between the pyrites, a qtz-only zone and whm + crb + qtz + cm in the external wedge; bifurcating shadow tails on opposite sides of the assembly consist of fibrous qtz; (b) detail of (a) showing fibrous tail-quartz grown on micro-shears of cm; S-shape is attributed to inward growth from the curving surfaces of bordering micro-shears; note the not-elongate qtz grains with bulging boundaries in the adjacent more internal zone; (c) deformation effects on pyrite textures in detail of (a): bulging grain boundaries in inclusion-rich internal parts suggest annealing/recrystallisation of pre-existing pyrite that underwent brittle fracturing and grain-size reduction, whereas euhedral outlines of inclusion-free margins point to late outgrowth; elongate sheared grain attest to a relatively early start of sulphide mineralisation; (d) interference between earlier folding phase (red dotted lines) and later shearing concentrated in a broad band (yellow hyphened lines) rich in cm (dark); white hyphened lines trace the orientation of tightly-spaced axial planar foliation; clusters of recrystallised pyrite have strain shadows with qtz on opposite sides, presumably controlled by the overriding shearing phase; (e) detail of pyrite in (d) showing microfolds (red dotted lines) and crenulation foliation (white hyphened lines) preserved in the central part; late-grown inclusion-free margin and qtz (see d) on the same sides of the clusters represent shear-related strain shadows; (f) shear foliation bending around apy porphyroblast with qtz-rich strain shadows; micro-shear zones are lined with cm (black); note the presence of py and crb in qtz-rich domains. (g-h) silicified domains in CPhU rock; interstitial elongated micro-qtz, grown perpendicular to the surfaces of folded cm laminae, replaced pre-existing phyllosilicates; (i) microfolded cm laminae with crenulation foliation (white hyphened lines) surrounded by micro-qtz as in (g); (j) micro-fold with partly silicified whm domains between cm laminae; (k-n) textural differences between sulphides in domains that underwent little (k-l) and significant (m-n) shear-induced deformation; note the bulging boundaries of equidimensional qtz grains in l and the aligned orientation of elongate qtz grains in (n); (o) pyrite showing internal fracturing, recrystallisation and formation of sub-grains induced by moderate deformation; (p) pyrite with fibrous qtz in strain shadow, indicating that deformation continued after the sulphides had formed; (q) late, euhedral and undeformed pyrite grain overgrown onto an older fractured and recrystallised aggregate of strongly deformed pyrite. Mineral abbreviations as in Fig. 10.

carbonate and/or white mica, locally in the form of fibrous crystals (Fig. 21a-f), indicate that the shear-related D_{2Ov} deformation continued after mineralisation had started. Unlike most of the pyrites in the Chert Unit, the crystals show euhedral outlines and deformation effects are limited to recrystallisation, fracturing and in-situ formation of aggregates, presumably because much of the shear stress was accommodated by ductile deformation of surrounding phyllosilicates. Annealing and regrowth may have been promoted by repeated influx of mineralising fluid as suggested by the frequent presence of inclusion-free margins with euhedral outlines in shear-strain shadows (cf., Craig et al., 1998).

Micro-textures of the main sulphide-bearing units thus provide compelling evidence for introduction of mineralising hydrothermal fluids before the D_{2Ov} shearing phase terminated. Sulphide mineralisation is clearly coeval with shearing in the Chert Unit and was only locally followed by recrystallisation under strain-free conditions (Fig. 21q). Sulphides In the carbonaceous phyllites were also affected by shearing but textures alone are inconclusive as to how much of the sulphide population represents an earlier mineralisation history. However, dissimilar sulphide assemblages and associated chemical signatures of the two units favour distinct phases of mineralisation in view of the different concentration relationships between S and chalcophile elements (e.g., Co, Cu, Pb, Zn, Se, Bi) in bulk samples (Fig. 14), together with more diversity in sulphide minerals and larger abundance of chalcopyrite, sphalerite and galena in the carbonaceous phyllites. A protracted multiphase mineralisation history is further supported by the distinctive enrichment of gold in the chert interval, and by texturally zoned appearances of individual sulphide grains in both units.

The association of gold and arsenic, seen in bulk-rock compositions (Fig. 15c), and the presence of As-bearing sulphides indicate that primary gold enrichment occurred through an influx of As-rich mineralising fluid. The presence of visible gold in late-stage fractures of arsenopyrite, in assemblages of recrystallised As-poor pyrite or as isolated grains in quartz domains (Fig. 9) points to remobilisation of gold that was structurally bound in the sulphides, presumably in response to recurrent shearing. Similar features of remobilisation have been documented for other Paleoproterozoic shear-zone associated gold deposits in the Guiana Shield (see Fig. 1), such as El Callao in the Guasipati-El Callao greenstone belt of Venezuela (Velásquez et al., 2014), the Boulanger deposit in *meta*-volcanics of the Paramaca Fmt within the Northern Guiana Trough (Lacroix et al., 2024) and the Yaou deposit at the contact between the Southern Paramaca Greenstone Belt and the central TTG complex (Combes et al., 2022), both in French Guiana. The Obuasi deposit and Bogosu-Prestea mining district are equivalent examples in the Ashanti Gold Belt of Ghana (e.g., Mumin et al., 1994; Fougerouse et al., 2017).

4.6. Hydrothermal alteration and veining

Massive silicification is the only obvious type of alteration of the gold-hosting unit. Ghost structures suggest that silicification proceeded through replacement of *meta*-sediments (S-chert in the terminology of Van den Boorn et al., 2007), producing a major elongated lensoid body and subordinate parallel sheets with largely stratiform orientations. Contacts in outcrop (Supplementary Fig. S2e) and drill cores indicate that intervals in the CPhU were mostly affected, but additional involvement of the PhU cannot be excluded. Silicification was pervasive, involving effective removal of all constituents of the silica phases (mostly white mica and chlorite) other than Si, presumably with exception of pre-existing quartz. This also applies to commonly "immobile" elements such as Zr, Ti other HFSE and REE, which are either undetected or much lower in concentrations than in both phyllitic units (Table 3), in agreement with the virtual absence of host minerals (e.g., zircon, rutile). This type of rock alteration requires interaction with a chemically aggressive fluid, possibly a low-pH, halogen-rich solution (e.g., Van Hinsberg et al., 2010). Preservation of foliated graphitic matter in samples of incompletely silicified carbonaceous phyllite (Fig. 21 g-j) indicates that carbon was relatively resistant to the silicification process. It also shows that the silicification event post-dated the folding phases (S_{1Ov}-S_{2Ov}).

Other types of alteration are of limited extent and intensity, and are restricted to the phyllitic rocks at thin-section scale. In the carbonaceous rocks the alteration features include small, relatively strain-free pockets of chlorite or pyrrhotite-carbonate-quartz and epidote-carbonate domains. Carbonate is predominantly siderite, locally in solid solution with magnesite (±Ca ± Mn). Lining of micro-shear zones by graphitic material (e.g., Fig. 10a-d) is probably a result of in-situ transposition rather than carbonitisation involving an external source, given the generally stratiform distribution of carbonaceous matter. Fibrous quartz, white mica and carbonate also occur in *syn*-shear pressure shadows around disseminated pyrite porphyroblasts in carbonaceous phyllites. The PhU locally contains chlorite-only veinlets, whereas albitisation affected portions of the rhyolitic dyke.

This overall poor development of wall-rock alteration seen at Overman tends to be a general feature for turbidite-hosted gold deposits, although evidence for a more widespread and pervasive effects of fluid-mediated exchanges have been documented as well (Bierlein et al., 1998 and references therein). Local systematics follow this pattern, since in the adjacent North domain of the RGM, where the proportion of fine-grained turbiditic *meta*-sediment is considerably lower, alteration is more intense and depends both on the vicinity of the mineralised shear zone and on the nature of the host rock (Daoust et al., 2011). The alteration assemblage near the shear zone consists of chlorite + sericite

+ plagioclase + hematite + carbonate ± pyrite. Chlorite and calcite are dominant alteration products in volcanic rocks and greywacke, whereas sericite is more common in arenites.

Multiple generations of quartz veinlets, ubiquitous in the phyllitic units at Overman, show a wide array of deformation phenomena, indicating that (micro-)veining was virtually continuous throughout the protracted tectonic history from initial folding to superimposed ductile shearing. Shear-induced recrystallisation and grain-size reduction are a widespread feature. Carbonate is often associated with quartz in vein-type domains hosting the sulphides that were introduced probably in the early stages of the D_{2OV} shearing phase. Quartz veins also occur in the ChU. Differences in grain size of recrystallised quartz with that of the matrix suggests that this veining was simultaneous with or later than the silicification event. It is unclear if the late-stage, post-mineralisation veins (Supplementary Fig. S3a-b) belong to the shearing phase or a later event.

Age constraints on gold mineralisation

4.7. Inferences from zircon ages

The zircon ages of the Overman rocks provide brackets on the timing of gold mineralisation in the area. The deposition interval of the host sediments determines the maximum age, whereas the felsic dyke intrusion marks the minimum age limit. The rationale is that the dyke (1) crosscuts the entire metamorphosed and deformed sequence, (2) was not affected by the same mineralisation as the chert, as it does not show any enrichment in gold (Fig. 15) despite the presence of sulphides and its likely permeability for gold-bearing fluids, and (3) was emplaced around the end or after the shearing episode, as the evidence for only minor deformation at outcrop, drill-core and thin-section scale indicates.

These considerations yield a time window for gold mineralisation in the Overman deposit between 2.16 and 2.03 Ga if the youngest detrital of only the local *meta*-sediment sample would determine the maximum deposition age of the host sediment. It narrows to a 2.08–2.03 Ga interval if the entire sequence of detrital sediments in the Overman-Rosebel area is taken into account. Gold mineralisation must have taken place towards the end of this interval, given the time needed to complete the regional tectono-metamorphic cycle before intrusion of the rhyolitic dyke, as well as the evidence for ore emplacement late in the post-peak shearing history.

4.8. Inferences from the tectono-metamorphic history in the Rosebel gold mining district

Since the micro-textural evidence on the timing of mineralisation relative to the deformation history is largely derived from non-oriented drill-core samples, a detailed kinematic reconstruction of the Overman deposit is not feasible. However, considering the regional tectonic fabric, structural continuation at map scale (Fig. 4) and apparent similarity in the sequence of deformation events, the area in all likelihood experienced largely the same kinematic evolution as the neighbouring RGM, especially its northern domain. The following sequence of tectonic events has been inferred here (Daoust, 2016):

Formation of pull-apart basins through a system of sinistral strike-slip and normal faults in a NE-SW to ENE-WSW transtensional regime; progressive faulting partly coincided with deposition of the turbiditic Armina and arenitic Rosebel sediments.

Onset of deformation in the sediment sequence with folding and thrusting in a NNE-SSW compressional regime; development of folds and foliation under greenschist metamorphic conditions.

Possible steepening of the thrust faults, reactivation of existing structures in dextral strike-slip faults (shear zones) and local reverse faulting in an N-S transpressional regime; mineralisation towards the end of this phase, thus late in the deformation history.

This complexity of the deformation history was confirmed in a recent field-based structural analysis of the RGM (Gapais et al., 2021), which demonstrated the importance of horizontal shortening and vertical stretch.

In a revised version of the chronology of geological events proposed previously (Daoust et al., 2011), Daoust (2016) envisaged that the entire sequence of basin formation, sedimentation, compressional deformation, metamorphism and transpressional deformation accompanied by strike-slip faulting and mineralisation (i.e., phases I to III) proceeded in a period after 2.08 Ga. Gold mineralisation in the RGM, following the compression-transpression transition, would not be older than ca. 2.00 Ga but a precise age is lacking. The zircon ages obtained for the Overman deposit, where the sequence of geological events is analogous, suggests that the entire cycle, including the late stage gold mineralisation, took place before ca. 2.03 Ga.

4.9. Conceptual genetic scenario

Fig. 22 summarises the crystallisation of minerals in a sequence of events relative to the ore formation. The observations from deposit to microscopic scale, in combination with existing hypotheses for the geodynamic evolution the northern Guiana Shield (Vanderhaeghe et al., 1998; Delor et al., 2003a,b; Milési et al., 2003, and references therein) suggest that shear-related gold mineralisation at Overman fits largely in a framework of a collision-induced termination of plate convergence, as schematically illustrated in Fig. 23.

Following their deposition as continentally-derived erosion products in a fore-arc (pull apart) basin, which presumably formed in response to oblique subduction (Ledru et al., 1991, 1994; Milési et al., 1995; Vanderhaeghe et al., 1998), the host sediments were folded and metamorphosed under greenschist-facies conditions during accretion along an active subduction margin. The clastic turbiditic nature of the Armina Fmt, the metamorphic grade and style of deformation are consistent with off-scraping and piling up of sediments from the down-going plate, analogous to a present-day accretionary-wedge type setting (Von Huene and Scholl, 1991; Angiboust et al., 2021). Fault-bounded alternations of the Armina Fmt and stratigraphically underlying Paramaka Fmt in steeply dipping stacks (Fig. 2) are further suggestive of an origin as tectonically dismembered slivers at the front of an accretionary orogen (Figs. 23b,c).

Silicification during the transition towards a collision regime was a crucial prelude to ore formation in the Overman area, as the more competent mechanical properties of the newly formed chert interval permitted the creation of pathways for mineralising fluids rising along steeply dipping fault zones. Shear-induced recrystallisation of the quartz-rich matrix under semi-ductile strain conditions led to preferential enhancement of permeability in silicified layers of the *meta*-sediment, which explains the restriction of major gold enrichment to the Chert Unit only.

The sulphide and gold mineralisation occurred during a protracted period of ductile shearing at crustal scale, associated with the formation of the North Suriname Shear Zone (Voicu et al., 2001) during tectonic accretion and collision of continental blocks, as proposed for the late Trans-Amazonian geodynamic evolution of French Guiana (Vanderhaeghe et al., 1998; Delor et al., 2003a,b; Milési et al., 2003, and references therein). Mineralisation in the Antino orogenic gold system in SE Suriname (Fig. 1) also occurred during an extended sequence of ductile and localised brittle deformation (Combes et al., 2025). The inferred deformational control of focussed fluid migration and gold mineralisation at Overman, which likely took place in multiple pulses, is consistent with generalised models for the origin of shear-related orogenic gold deposits at mid-crustal levels in accretionary-collisional systems (e.g., Bonnemaison and Marcoux, 1990; Groves et al., 1998; Cox, 1999; Goldfarb et al., 2001; Bierlein et al., 2009; Goldfarb and Groves, 2015). The specific Au-As type of orogenic gold deposit as identified here for Overman is relatively rare in the Guiana Shield and has so far only been documented in a comparable setting at Camp Caïman in northern French Guiana (Milési et al., 2003; Bardoux et al.,

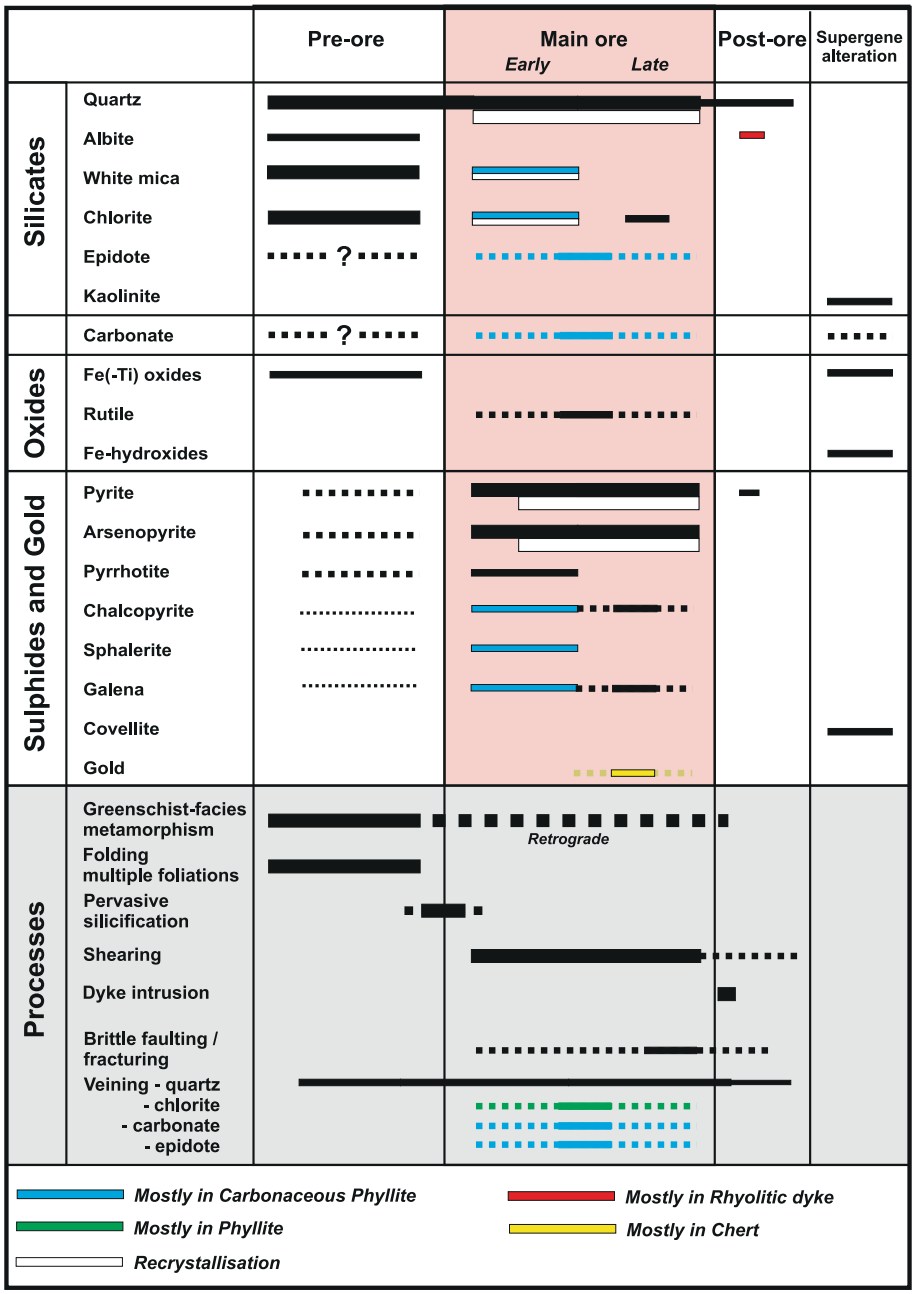

Fig. 22. Schematic paragenetic sequence for ore-related and gangue minerals, and relationship with local metamorphic, tectonic, magmatic and hydrothermal processes inferred for the Overman deposit. A schematic illustration of the proposed associated geodynamic evolution at larger scale is shown in Fig. 23. Thickness of mineral bars indicates relative abundance; dotted lines suggest uncertainty.

2018).

It is conceivable that collision was associated with low angle underthrusting of the thin leading edge of a continental block and that the crust became detached from underlying lithosphere when thicker portions entered the subduction zone (Fig. 23c). This process may be a common feature of continental subduction during hot Proterozoic orogenesis, as recently proposed by Van Hinsbergen et al. (2025). In the Late Trans-Amazonian orogen of northern Suriname, this decoupling from mantle lithosphere may well have promoted pervasive shearing in the subducted crust and overlying domain. Accompanying upward influx of hot asthenosphere could have provided heat for metamorphism, mobilisation of the mineralising fluids and the formation of felsic magma feeding intrusions such as the rhyolitic dyke at Overman and the late two-mica Patamacca granite (see Fig. 20).

Disregarding the details of metallogenic controls, the regional tectonostratigraphic architecture and terminal orogenic setting point to conspicuous similarities with gold belts in the Archean Yilgarn and Superior cratons (e.g., Hagemann and Cassidy, 2000; Robert et al., 2005; Hastie et al., 2023), the Paleoproterozoic orogenic belts of the Birimian (Milési et al., 1992) and Trans-Hudson (Lawley et al., 2023), and the Mesozoic West Qinling orogenic belt (Deng and Wang, 2016; Hu et al., 2022).

4.10. Comparison in the regional context of the Guiana Shield

In terms of timing and setting, the Overman and adjacent Rosebel deposits fit into the Paleoproterozoic episode of orogenic gold mineralisation in greenstone-sedimentary rock sequences recognised at a global scale (Groves et al., 1998; Goldfarb et al., 2001 and references therein). Other primary gold occurrences in the Marowijne greenstone

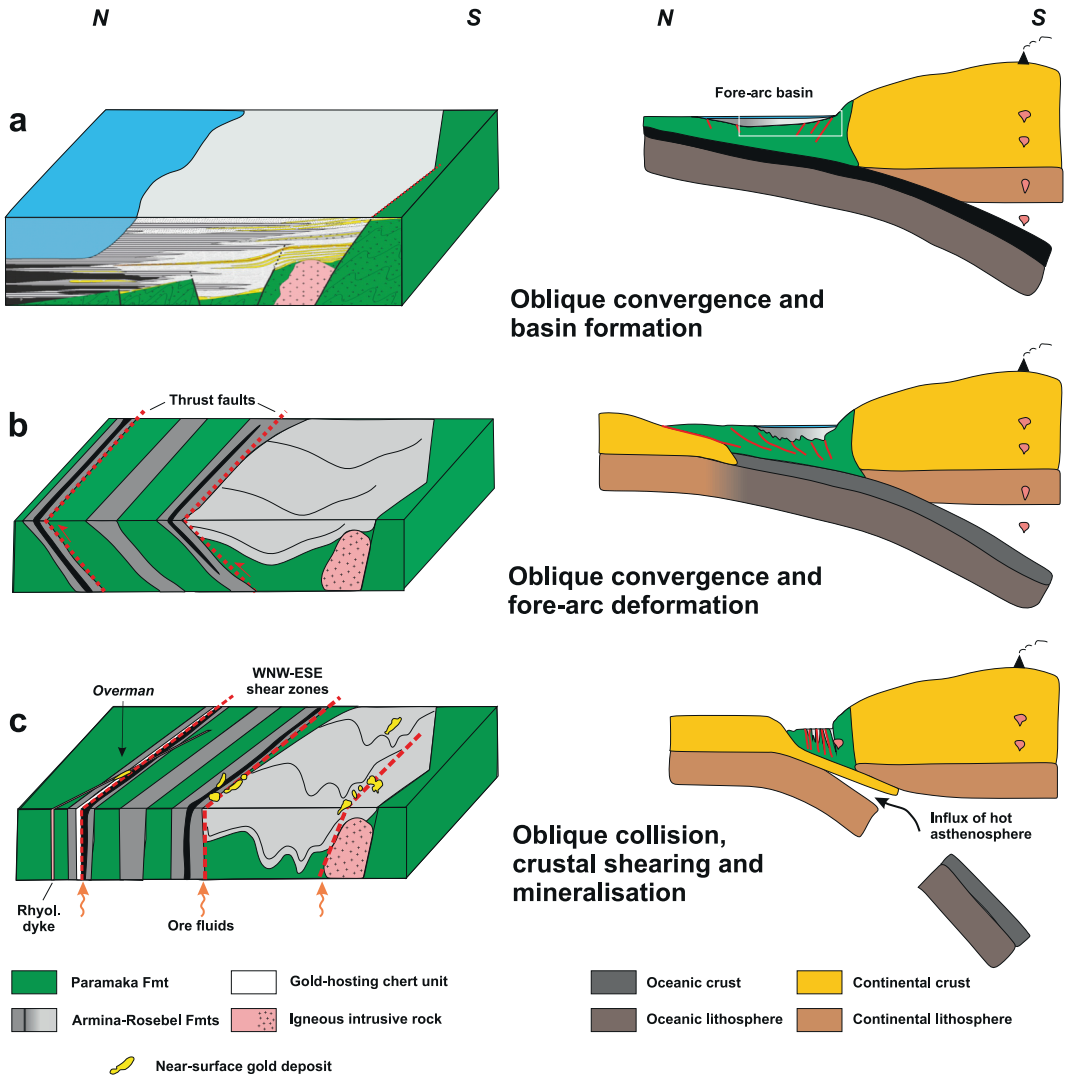

Fig. 23. Conceptual framework for the geological setting of the Overman gold deposit. Block diagrams on the left: depositional environment and deformation history of host sediments; the proposed stratigraphic relationship of the Armina and Rosebel Fmts (inspired by Daoust, 2016; cf., Fig. 18) in a fore-arc (pull-apart) basin is illustrated in (a). 2-D cross sections on the right: geodynamic scenario at larger scale showing a possible sequence of oblique convergence and collision consistent with the association of orogenic gold and crustal shear systems in north-east Suriname; rectangle in (a) indicates the position of the block diagrams. A hypothetical separation between crust and lithosphere with concomitant influx of asthenosphere, as proposed for "hot" continental subduction in accretionary orogens (Van Hinsbergen et al., 2025), may have contributed to a thermal anomaly associated with gold mineralisation. Vertical dimensions are not to scale and Indicated orientations are tentative only.

belt (e.g., Voicu et al., 2001; Kioe-A-Sen et al., 2016; Combes et al., 2024) and elsewhere in the Guiana shield fall into the same category but mineralisation ages of individual deposits, estimated from a variety of absolute dating approaches, suggest a large range between ca. 2.15 and 1.98 Ga (see Fig. 20).

4.10.1. Timing of gold mineralisation events

When considering only the most reliable age constraints thus far available for deposits across the Guiana Shield, gold deposition occurred in different events in the 2.15–2.08 Ga interval, i.e. during the Trans-Amazonian D_1 and D_{2a} stages of Delor et al. (2003b). SHRIMP U-Pb zircon ages of 2143 ± 6 Ma and 2145 ± 5 Ma for acidic calc-alkaline volcaniclastics, 2142 ± 2 Ma for a tholeiitic *meta*-gabbro, and 2117 ± 3 Ma for a crosscutting trondhjemitic plutonic body with calc-alkaline affinity brackets the timing of the main gold mineralisation event at Choco-10 (Padoan et al., 2014). LA-ICP-MS U-Pb zircon ages of ca. 2152–2130 Ma for the bimodal tholeiitic and calc-alkaline volcanic-intrusive host rocks, and 2117.6 ± 5.1 Ma for a crosscutting porphyry intrusion constrains the age of the Montagne d'Or deposit, making it the oldest known in the Guiana Shield. A U-Pb LA-ICP-MS date of 2084 ± 14 Ma for hydrothermal titanite from the hydrothermal alteration zone associated with Au-bearing veins, and supported by 2092 ± 7 and 2089 ± 11 Ma SHRIMP zircon ages of intrusive host rocks, determines the timing of gold mineralisation at Karouni (Tedeschi et al., 2020). Re–Os dating of Au-bearing pyrite from the Yaou deposit in French Guiana yielded 2105 ± 25 Ma (Combes et al., 2022).

The validity of reported ages younger than ca. 2.01 Ga as gold mineralisation dates is questionable as discussed in Tedeschi et al. (2020), since these are based on Pb-Pb model ages obtained on galenas with unknown relationships to the ore deposition (Dorlin, Saint Pierre, Loulouie; Marcoux and Milési, 1993), a Pb-Pb isochron obtained from titanite, rutile and apatite grains with little or no significance with the gold deposition event (Omai; Norcross et al., 2000), or Ar-Ar plateau ages on hydrothermal biotite (St. Elie; Lafrance et al., 1999 in Tedeschi et al., 2020).

4.10.2. Shear-zone relationships of gold deposits

Major gold deposits and occurrences in the Northern Guiana Shield

are spatially associated with craton-scale shear zones (Milési et al., 1995, 2003; Voicu et al., 2001; Tedeschi et al., 2018a,b), most of which run roughly parallel to the Atlantic coast (Fig. 1). In Suriname, the geographic distribution of large-scale and artisanal mining activities and prospective gold appears to follow roughly two major zones in the Marowijne Greenstone Belt (Kioe-A-Sen et al., 2016): the E-W oriented Northern Suriname Shear Zone (NSSZ), which in East Suriname bends southwards and connects to the NW-SE to NNW-SSE trending Marowijne (Maroni) shear system (MS), possibly a splay of the Central Guiana Shear Zone (CGZC; Voicu et al., 2001). The Overman-Rosebel area is situated near the NSSZ, as are the Maripaston, Saramacca and Sabajo Hills deposits and the Merian mining area, the latter at a position close to the inferred bend. Deposits in proximity of the MS include Sara Creek, Lely Mountains and Benzdorp but actual shear-zone relationships remain to be assessed. In contrast, the recently studied Brothers Project near the border with French Guiana (Fig. 1) is likely connected to the MS system (Combes et al., 2024). Here, quartz-vein associated gold accumulated in shear zones hosted in a Rhyacian biotite-tonalite batholite complex, referred to as TTG-like, which experienced a polyphase deformation history (Combes et al., 2024). Gold enrichment occurred in two main events, related to syn- and post-shearing pyritisation, and was presumably controlled by zones of high permeability for mineralising fluids near intersections of shear segments with younger NNW-striking brittle structures running parallel to the Marowijne splay (Combes et al., 2024). In addition, high-grade, structurally controlled gold mineralisation in volcanic-sedimentary sequences of the Paramaka Fmt. and tonalitic intrusions in the Antino area, near the connection of the craton-scale Central Guiana Shear Zone and the Marowijne splay (Fig. 1), is also typical for occurrences where the ore formation was associated with shear (Fleming, 2006; Kaneki and Hirono, 2019; Raffle and Lefrançois, 2022).

In French Guiana, the vast majority of gold-bearing conglomerate type and mesothermal-orogenic type occurrences are associated with the D_2 transcurrent tectonic event expressed by E-W to NW-SE sinistral strike-slip faults mapped across the country (Ledru et al., 1991; Egal et al., 1992; Milési et al., 1995, 2003; Vanderhaeghe et al., 1998; Delor et al., 2003a,b). Their spatial distribution has a clear relationship with the regional-scale shear zones of the Northern Guiana Trough and the Central Guiana Shear Zone (NGT and CGSZ in Fig. 1), where the conglomerate-type gold is generally hosted in the Upper Detrital Unit, and the mesothermal-orogenic type in *meta*-sediments and *meta*-volcanics of the Paramaca Formation or in *syn*-D_2 granitoids (Milési et al., 2003; Lacroix et al., 2024).

In Guyana, a series of gold deposits is located in the vicinity of the regional NW-SE trending Makapa-Kuribrong shear zone (Voicu et al., 2001). The Karouni gold deposit, hosted in greenschist-facies mafic volcanic rocks and felsic intrusions of the Barama-Mazaruni Supergroup is associated with a second-order splay. Mineralisation is inferred to have taken place late in a deformation sequence, involving early folding in a compressional regime and accompanying peak metamorphism, followed by a transpression-induced formation of E-W trending sinistral shear zones, and ending with dextral shearing upon an anticlockwise shift of the far-field stress, and simultaneous gold emplacement (Tedeschi et al., 2018b).

Mineralisation in the El Callao gold mining district (Venezuela) is related to a similar structural evolution accompanying the transition from subduction to collision and development of shear zones associated with a lithospheric-scale fault zone (Velásquez et al. 2014, 2018). Textural and fluid-inclusion evidence from a complex network of intersecting veins in the exhumed El Callao transpressional shear zone points to a protracted fluid circulation history during the transition from a purely ductile to a near-brittle regime, whereby gold was initially incorporated in invisible form in pyrite and was eventually liberated and precipitated in pores and fractures.

4.11. Overman, an ashanti-like deposit in the Guiana Shield

The characteristics of gold mineralisation at Overman fulfil the criteria of mesothermal orogenic systems since ore formation occurred in a fluid-localizing shear zone as part of a larger crustal-scale structure during deformation at temperatures between ca. 300 and 500 °C (e.g., Cox, 1999).

The Overman deposit is an exceptional case of orogenic Au-As deposits identified in the Guiana Shield till date. In French Guiana, mesothermal orogenic gold is dominated by Au-Fe-Cu type deposits related to brittle-fault zones, whereas an Au-As type, such as at Camp Caïman in the northern greenstone belt, is rare (Milési et al., 2003). Hosted in Armina sedimentary rocks, gold is here associated with pyrite and arsenopyrite, occurring both in disseminated form and in D_2-related quartz veins in shear-zone settings, with quartz, chlorite and muscovite as main gangue minerals. An Au-As relationship seems also applicable to the Yaou occurrence, situated at the contact between the Southern Paramaca Greenstone Belt and the central TTG complex, where Combes et al. (2021) documented a polyphase mineralisation and deformation history, involving early formation of stratabound sediment-hosted As-bearing pyrite with invisible gold, possibly diagenetic in origin, which was followed by several other deformation-related gold events. The main phase, when visible gold was produced in fractures and inclusion of intrusion-hosted pyrite, is associated with Ag-Te-Bi enrichment and was structurally controlled by sinistral shearing, presumably related to the regional D_{2b} event of Delor et al. (2003b). The relative importance of gold remobilisation versus fresh input is unclear (Combes et al., 2021). Nonetheless, there are noticeable parallels with the Overman deposit considering the As affinity, regional shear-related setting, complexity and longevity of mineralisation, as well as the timing late in the Trans-Amazonian orogenic evolution.

Similarities in the Paleoproterozoic geological evolution and gold metallogeny of the Guiana Shield and the more extensively studied West African Shield have long been recognised (e.g., Ledru et al., 1991, 1994; Milési et al., 1995, 2003). The correspondence pertains to the nature and timing of events within the geodynamic cycle of the Trans-Amazonian and Eburnian orogens, involving magmatic accretion of juvenile crust, plate convergence followed by collision and transcurrent tectonics, accompanying magmatism and stratigraphic architecture, as well as the extended history of multi-style gold mineralisation, with the most proliferous endowments often related to major fault zones.

Overman shares a remarkable set of common features with deposits in the Ashanti gold belt (Ghana), such as the giant Obuasi deposit. Ashanti mesothermal gold ores are also hosted in shear zones in greenschist-facies metamorphosed carbonaceous phyllites and greywackes of a turbiditic deep-water sequence (Kumasi Group), at or near contacts with mafic volcanics (Sefwi Group) or shallow-water to subaerial phyllites, sandstones and conglomerates (Tarkwa Group) (e.g., Allibone et al., 2002a,b; Oliver et al., 2020; Thébaud et al., 2020, and references therein). The stratigraphic-structural framework is largely similar to that of the Overman-Rosebel area, as are successive stages of deformation fitting in a late orogenic accretion-collision tectonic context (transition from thrusting during orthogonal subduction to shearing during oblique collision accompanied by crustal reworking), the conditions of metamorphism, and the post-peak metamorphic signature and timing of the gold mineralisation late in the Eburnian orogenic cycle at ca. 2.1–2.0 Ga (Feybesse et al., 2006; Perrouty et al., 2012; Goldfarb et al., 2017; Grenholm et al., 2019; Oliver et al., 2020; Thébaud et al., 2020; Masurel et al., 2022, and references therein). The Ashanti gold belt hosts As-rich ores in an Fe-As-S-Au assemblage, expressed in the presence of disseminated gold-bearing arsenopyrite and As-bearing pyrite, similar to the arsenopyrite-pyrite assemblage in the Overman chert, whereas a second, spatially associated Pb-Sb-Cu-S-Au-Ag ore assemblage comprises native gold in micro-cracks in major quartz veins (Milési et al., 1992; Mumin et al., 1994; Oberthür et al., 1997; Fougerouse et al., 2017; Oliver et al., 2020). Redistribution of refractory gold,

involving remobilisation from the sulphide lattice at grain scale and beyond (Mumin et al., 1994; Fougerouse et al., 2017) is also seen in the textural evidence for gold liberation from originally auriferous arsenopyrite and arsenian pyrite in the Overman chert (Fig. 9).

Different opinions have been put forward as to whether co-existing refractory gold and visible gold were produced during a single progressive event or represent distinct episodes of mineralisation under different conditions. For the Bogosu-Prestea mining district, Mumin et al. (1994) used distribution patterns of visible and invisible gold in (arsenian) pyrite and arsenopyrite to infer that redistribution of gold commenced immediately after deposition and continued throughout the post-depositional history, and suggested increasing hydrothermal/metamorphic grade, deformation and recrystallisation of host minerals, as well as decreasing grain size and refractory properties of host minerals as potential driving mechanisms. For the giant Obuasi deposit, where the two types are hosted in spatially separated domains, Fougerouse et al. (2016a,b) inferred that they formed distinct episodes of mineralisation under different structural controls, whereby gold was mobilised from early-grown auriferous arsenopyrite during a later dissolution-reprecipitation process driven by interaction with newly infiltrated fluid. On the other hand, Oberthür et al. (1997) argued that redistribution of gold was insignificant, pointing to the preservation of gold in specific growth zones of sulphides, which they attributed to multiple episodes of fluid infiltration, fluid flow and mineral deposition during a single main phase of ore formation. They explained the distinct sulphide assemblages by a chemical gradient between host rocks and mineralising fluids.

At Overman, both visible and refractory varieties of gold are hosted in a single lithological unit of pervasively silicified *meta*-sediments affected by a protracted history of shearing. Textural and mineralogical evidence suggests that infiltration of As-rich mineralising fluids, growth of auriferous As-rich sulphides as well as redistribution all took place within this deformation interval. Internal variability in gold grade and relative proportions of arsenopyrite and pyrite, together with occasional preservation of complexly-zoned arsenian pyrites next to strongly deformed/re-crystallised sulphides, is consistent with differential strain and development of shear bands or networks under a relatively ductile regime (e.g., Fossen and Cavalcante, 2017; Roy et al., 2022), which channelled mineralising fluids that probably infiltrated in multiple pulses.

Considering these observations, a plausible a metallogenic model is that of long-term fluid circulation associated with the formation and exhumation of a crustal-scale shear zone and passage of the brittle-ductile transition, as also proposed for the El Callao gold district in Venezuela (Velásquez et al., 2018). Mineralised shear zones are likely related to reactivation of older structures, such as faults that supposedly bordered the original sediment basin, as suggested for the neighbouring RGM (Daoust et al., 2011).

The pre-shear silicification event in the Overman sequence was probably essential for gold mineralisation, as it produced the relatively competent quartz-rich interval that enabled the formation of a focused pathway for auriferous fluids under a (semi-)ductile to brittle deformation regime. A possible genetic relationship with sulphide mineralisation in the Au-poor phyllitic units adjacent to the chert-hosted deposit remains to be assessed. Also, despite a corresponding structural evolution with the Rosebel gold district, a possible metallogenic connection requires further study, particularly since the style of mineralisation differs. The ore assemblage at Rosebel is typically hosted in arrays of quartz-carbonate veins along pre-existing structural heterogeneities and lacks an As-rich signature (Daoust et al., 2011).

5. Conclusions

The Overman prospect in the Armina Fmt of the Rhyacian Marowijne Greenstone Belt is a mesothermal shear-zone related occurrence of orogenic gold, deposited in an interval of pervasively silicified *meta*-sediments within a strongly deformed turbiditic sequence locally rich in carbonaceous matter.

Geological evidence is consistent with deposition of the gold-hosting Armina and Rosebel Formations in a single basin, which represent a transition from deep-marine to terrestrial/shallow marine facies along a convergent plate boundary as proposed earlier by Daoust (2016).

Greenschist-facies metamorphism reached peak metamorphic temperatures around 500 °C based on RSCM and chlorite thermometry on samples from adjacent phyllites. Gold mineralisation occurred in a retrograde trajectory.

Polyphase deformation involved early multiple folding in a compressional regime and a late episode of transpressional shearing. A silicification event at the transition was essential for the ore formation.

Gold mineralization is connected with As enrichment, expressed in the common presence of arsenopyrite. Deposit-scale variations in gold-grade and sulphide abundance are assumed to reflect *syn*-shear formation of localised pathways for mineralizing fluids under semi-ductile to brittle conditions. Protracted shearing likely promoted secondary mobilisation of gold.

Ore formation occurred late in the Trans-Amazonian orogenic cycle, i.e. in the D_{2b} stage of Delor et al. (2003a,b), based on the youngest detrital zircons of the host formation and the zircon U-Pb intrusion age of a crosscutting rhyolitic dyke (2.033 ± 10 Ga); the main ore event probably occurred towards the end of the resulting 2.08–2.03 Ga time bracket.

The array of major gold occurrences within the North Suriname Shear Zone corridor underscores the importance of crustal-scale collision-related shear systems for ore formation in the Guiana Shield. Evident analogies between Overman and the mesothermal shear-hosted orogenic gold deposits of the Ashanti belt (Ghana) include the stratigraphic-structural framework in a late orogenic accretion-collision tectonic context, the apparent association with carbonaceous matter, prominence of early refractory gold in As-rich sulphides, and evidence for late-stage remobilisation.

Declaration of competing interest

The authors declare the following financial interests/personal relationships which may be considered as potential competing interests: N.M.E. Kioe-A-Sen reports financial support was provided by Rosebel Goldmines N.V. (Iamgold Corporation). If there are other authors, they declare that they have no known competing financial interests or personal relationships that could have appeared to influence the work reported in this paper.

Acknowledgement

This research is part of the PhD study of the first author at Utrecht University, made possible by generous funding from Rosebel Goldmines N.V.–Iamgold. Special gratitude goes to Dr. Gabriel Voicu for facilitating the start of the project at RGM, and to the staff of Mine Exploration and the Legal Department, in particular Sharmila Jadnansing and Nalini Mahabir, for continuous support and trust. Analytical work at the Geosciences Laboratory of UU would not have been possible without the expert service of Tilly Bouten, Eric Hellebrand, Helen de Waard, Otto Stiekema and Leonard Bik. Ton Markus kindly took care of the graphic design of maps. Constructive comments by two anonymous reviewers are gratefully acknowledged.

Appendix A. Supplementary data

Supplementary data to this article can be found online at https://doi.org/10.1016/j.oregeorev.2025.106892.

Data availability

I have shared the link to my data at the attach file step

References

Allibone, A.H., Campbell Mc Cuaig, T., Harris, D., Etheridge, M., Munroe, S., Byrne, D., Amanor, J., Gyapong, W., 2002a. Structural Controls on Gold Mineralization at the Ashanti Deposit, Obuasi, Ghana. Integrated Methods for Discovery: Global Exploration in the Twenty-First Century, 9 (Special Publications of the Society of Economic Geologists). https://doi.org/10.5382/SP.09.

Allibone, A., Teasdale, J., Cameron, G., Etheridge, M., Uttley, P., Soboh, A., Appiah-Kubi, J., Adanu, A., Arthur, R., Mamphey, J., Odoom, B., Zuta, J., Tsikata, A., Pataye, F., Famiyeh, S., 2002b. Timing and Structural Controls on Gold Mineralization at the Bogoso Gold Mine, Ghana, West Africa. Econ. Geol. 97, 949–969.

Anandbahadoer-Mahabier, R., De Roever, E.W.F., 2019. The Caicara-Dalbana Belt, a Belt of Felsic and Intermediate Metavolcanics of 1.99 Ga in the Guiana Shield, and Probably Across, in the Guapore Shield. Extended Abstract. In: Proceedings 11th Inter-Guiana Geol. Conf. Feb. 2019, Paramaribo, Suriname, Mededeling Geol. Mijnb. Dienst Suriname, 29, 7–11.

Angiboust, S., Munoz-Montecinos, J., Cambeses, A., Raimondo, T., Deldicque, D., Garcia-Casco, A., 2021. Jolts in the Jade factory: a route for subduction fluids and their implications for mantle wedge seismicity. Earth Sci. Rev. 220.

Bardoux, M., Moroney, M., Robert, F., 2018. Gold mineralization in the Guiana Shield, Guiana and Suriname, South America: A field trip to the 14th biennial Society for Geology Applied to Mineral Deposits (SGA) meeting (8351; p. 8351). https://doi.org/10.4095/306546.

Barzoi, S.C., 2015. Shear stress in the graphitization of carbonaceous matter during the low-grade metamorphism from the northern Parang Mountains (South Carpathians)—Implications to graphite geothermometry. Int. J. Coal Geol. 146, 179–187. https://doi.org/10.1016/j.coal.2015.05.008.

Beek, S.K., 2019. Basalt-hosted gold in the Paleoproterozoic Marowijne greenstone belt (Suriname): Insights into volcanic setting and alteration style of the. Anton de Kom University of Suriname. Saramacca deposit [MSc thesis].

Berge, J., 2011. Paleoproterozoic, turbidite-hosted, gold deposits of the Ashanti gold belt (Ghana, West Africa): Comparative analysis of turbidite-hosted gold deposits and an updated genetic model. Ore Geol. Rev. 39 (1–2), 91–100. https://doi.org/10.1016/j.oregeorev.2010.12.001.

Beunk, F.F., De Roever, E.W.F., Yi, K., Brouwer, F.M., 2021. Structural and tectonothermal evolution of the ultrahigh-temperature Bakhuis Granulite Belt, Guiana Shield, Surinam: Palaeoproterozoic to recent. Geosci. Front. 12 (2), 677–692. https://doi.org/10.1016/j.gsf.2020.05.021.

Beyssac, O., Goffé, B., Chopin, C., Rouzaud, J.N., 2002. Raman spectra of carbonaceous material in metasediments: a new geothermometer. J. Metam. Geol. 20 (9), 859–871. https://doi.org/10.1046/j.1525-1314.2002.00408.x.

Bierlein, F.P., Fuller, T., Stüwe, K., Arne, D.C., Keays, R.R., 1998. Wallrock alteration associated with turbidite-hosted gold deposits. examples from the Palaeozoic Lachlan Fold Belt in central Victoria, Australia. Ore Geol. Rev. 13 (1–5), 345–380. https://doi.org/10.1016/S0169-1368(97)00026-7.

Bierlein, F.P., Groves, D.I., Cawood, P.A., 2009. Metallogeny of accretionary orogens — the connection between lithospheric processes and metal endowment. Ore Geol. Rev. 36 (4), 282–292. https://doi.org/10.1016/j.oregeorev.2009.04.002.

Bijnaar, G., Van Bergen, M.J., Wong, T.E., 2016. The kyanite quartzite of Bosland (Suriname): evidence for a Precambrian metamorphosed alteration system. Netherlands Journal of Geosciences - Geologie En Mijnbouw 95 (4), 447–465. https://doi.org/10.1017/njg.2016.38.

Bonnemaison, M., Marcoux, E., 1990. Auriferous mineralization in some shear-zones: a three-stage model of metallogenesis. Miner. Deposita 25 (2). https://doi.org/10.1007/BF00208851.

Bosma, W., Kroonenberg, S.B., Maas, K., De Roever, E.W.F., 1983. Igneous and metamorphic complexes of the Guiana Shield in Suriname. Geol. Mijnb. 62, 241–254.

Bosma, W., Kroonenberg, S.B., van Lissa, R., Maas, K., De Roever, E.W.F., 1984. An explanation to the geology of Suriname. Mededelingen Geologisch Mijnbouwkundige Dienst Van Suriname 27, 31–82.

Bourdelle, F., 2021. Low-Temperature Chlorite Geothermometry and Related recent Analytical advances: a Review. Minerals 11 (2), 130. https://doi.org/10.3390/min11020130.

Bourdelle, F., Parra, T., Chopin, C., Beyssac, O., 2013. A new chlorite geothermometer for diagenetic to low-grade metamorphic conditions. Contrib. Miner. Petrol. 165 (4), 723–735. https://doi.org/10.1007/s00410-012-0832-7.

Burnell, J.R., Rutherford, M.J., 1984. An experimental investigation of the chlorite terminal equilibrium in pelitic rocks. Am. Mineral. 69, 1015–1024.

Buseck, P.R., Beyssac, O., 2014. From Organic Matter to Graphite: Graphitization. Elements 10 (6), 421–426. https://doi.org/10.2113/gselements.10.6.421.

Bustin, R.M., Ross, J.V., Rouzaud, J.N., 1995. Mechanisms of graphite formation from kerogen: Experimental evidence. Int. J. Coal Geol. 28, 1–36.

Carreras, J., Druguet, E., Griera, A., 2005. Shear zone-related folds. J. Struct. Geol. 27 (7), 1229–1251. https://doi.org/10.1016/j.jsg.2004.08.004.

Combes, V., Eglinger, A., André-Mayer, A., Teitler, Y., Heuret, A., Gibert, P., Béziat, D., 2021. Polyphase gold mineralization at the Yaou deposit, French Guiana. Geol. Soc. Lond. Spec. Publ. 516, 177–210. https://doi.org/10.1144/SP516-2020-29.

Combes, V., Eglinger, A., André-Mayer, A.-S., Teitler, Y., Jessell, M., Zeh, A., Reisberg, L., Heuret, A., Gibert, P., 2022. Integrated geological-geophysical investigation of gold-hosting Rhyacian intrusions (Yaou, French Guiana), from deposit-to district-scale. J. S. Am. Earth Sci. 114, 103708. https://doi.org/10.1016/j.jsames.2021.103708.

Combes, V., Eglinger, A., Bhoelan, R., LaPoint, D., 2024. Batholith-hosted polyphase gold mineralization at the Brothers project, eastern Suriname. J. S. Am. Earth Sci. 133, 104740. https://doi.org/10.1016/j.jsames.2023.104740.

Combes, V., Eglinger, A., Voegeli, P., Bhoelan, R., Bertoni, C., Padget, C., André-Mayer, A.-S., 2025. District to mineral-scale geometry of the world-class Antino orogenic gold system, southeastern Suriname (Guiana shield). Ore Geol. Rev. 180, 106575. https://doi.org/10.1016/j.oregeorev.2025.106575.

Condie, K.C., 1993. Chemical composition and evolution of the upper continental crust: Contrasting results from surface samples and shales. Chem. Geol. 104 (1–4), 1–37. https://doi.org/10.1016/0009-2541(93)90140-E.

Cox, S.F., 1999. Deformational controls on the dynamics of fluid flow in mesothermal gold systems. Geol. Soc. Lond. Spec. Publ. 155 (1), 123–140. https://doi.org/10.1144/GSL.SP.1999.155.01.10.

Craig, J.R., Vokes, F.M., Solberg, T.N., 1998. Pyrite: Physical and chemical textures. Miner. Deposita 34 (1), 82–101. https://doi.org/10.1007/s001260050187.

Daoust, C., 2016. Caractérisation stratigraphique, structurale et géochimique du district minéralisé de Rosebel (Suriname) dans le Cadre de l'évolution géodynamique de Bouclier Guyanais. Université du Québec à Montréal [PhD Thesis].

Daoust, C., Voicu, G., Brisson, H., Gauthier, M., 2011. Geological setting of the Paleoproterozoic Rosebel gold district, Guiana Shield, Suriname. J. S. Am. Earth Sci. 32 (3), 222–245. https://doi.org/10.1016/j.jsames.2011.07.001.

De Caritat, P., 1993. Chlorite Geothermometry: a Review. Clay Clay Miner. 41 (2), 219–239. https://doi.org/10.1346/CCMN.1993.0410210.

De Roever, E., Lafon, J.-M., Delor, C., Cocherie, A., Rossi, P., 2003. The Bakhuis ultrahigh-temperature granulite belt (Suriname): I. petrological and geochronological evidence for a counterclockwise P-T path at 2.07-2.05 Ga. Geologie De La France 2003, 175–205.

De Roever, Delor, C., Cocherie, A., Guerrot, C., 2015. Contribuições à Geologia Da Amazônia, 9, 359–372.

De Roever, E.W.F., Beunk, F.F., Yi, K., de Groot, K., Klaver, M., Nanne, J.A.M., van de Steeg, W., Thijssen, A.C.D., Uunk, B., Vos, H., Brouwer, F.M., Davies, G.R., 2019. The Bakhuis Granulite Belt in W Suriname, its development and exhumation. Extended Abstract. In: Proceedings 11th Inter-Guiana Geol. Conf. Feb. 2019, Paramaribo, Suriname, Mededeling Geol. Mijnb. Dienst Suriname, 29, 53–58.

De Roever, E.W.F., Harley, S.L., Huizenga, J.M., 2023. Primary cordierite with > 2.5 wt % CO2 from the UHT Bakhuis Granulite Belt, Surinam: CO2 fluid phase saturation during ultrahigh-temperature metamorphism. Contrib. Miner. Petrol. 178 (4), 26. https://doi.org/10.1007/s00410-023-02003-1.

De Vletter, D. R. (1984). Synthesis of the Precambrian of Suriname and review of some outstanding problems. In: De Vletter, D.R. (Ed.): Geology of Suriname 8. Mededelingen Geologisch Mijnbouwkundige Dienst Suriname, 27, 11–30.

Deckart, K., Féraud, G., Bertrand, H., 1997. Age of Jurassic continental tholeiites of French Guyana, Surinam and Guinea: Implications for the initial opening of the Central Atlantic Ocean. Earth Planet. Sci. Lett. 150 (3–4), 205–220. https://doi.org/10.1016/S0012-821X(97)00102-7.

Delor, C., Lahondère, D., Egal, E., Lafon, J.-M., Cocherie, A., Guerrot, C., Rossi, P., Truffert, C., Théveniaut, H., Phillips, D., de AVELAR, V.G., 2003a. Transamazonian crustal growth and reworking as revealed. Géologie de La France, 2-3–4, 5–57.

Delor, C., De Roever, E.W.F., Lafon, J.-M., Lahondère, D., Rossi, P., Cocherie, A., Guerrot, C., Potrel, A., 2003b. The Bakhuis ultrahigh-temperature granulite belt (Suriname): II. implications for late Transamazonian crustal stretching in a revised Guiana Shield framework. Géologie De La France 2–3–4, 207–230.

Deng, J., Wang, Q., 2016. Gold mineralization in China: Metallogenic provinces, deposit types and tectonic framework. Gondw. Res. 36, 219–274. https://doi.org/10.1016/j.gr.2015.10.003.

Dora, M.L., Randive, K.R., 2015. Chloritisation along the Thanewasna shear zone, Western Bastar Craton, Central India: its genetic linkage to Cu–Au mineralisation. Ore Geol. Rev. 70, 151–172. https://doi.org/10.1016/j.oregeorev.2015.03.018.

Egal, E., Mercier, D., Itard, Y., Mounié, F., 1992. L'ouverture de bassins en pull-apart au Protérozoïque inférieur: Nouveaux arguments dans le nord du craton guyanais. C.R. Acad. Sci. Paris, t. 314. Série II, 1499–1506.

Enjolvy, R. (2008). Processus d'accrétion crustale et régimes thermiques dans le bouclier des Guyanes: Signatures géochimiques et thermochronologiques au transamazonien (2250-1950Ma) [Géochimie.]. Université Montpellier II-Sciences et Techniques du Languedoc.

Feybesse, J.-L., Billa, M., Guerrot, C., Duguey, E., Lescuyer, J.-L., Milesi, J.-P., Bouchot, V., 2006. The paleoproterozoic Ghanaian province: Geodynamic model and ore controls, including regional stress modeling. Precambr. Res. 149 (3–4), 149–196. https://doi.org/10.1016/j.precamres.2006.06.003.

Fleming A., 2006. Technical report Antino Gold project Suriname, South America, Prepared for New Sleeper Gold Corporation, unpublished report.

Fossen, H., Cavalcante, G.C.G., 2017. Shear zones – a review. Earth Sci. Rev. 171, 434–455. https://doi.org/10.1016/j.earscirev.2017.05.002.

Fougerouse, D., Micklethwaite, S., Halfpenny, A., Reddy, S.M., Cliff, J.B., Martin, L.A.J., Kilburn, M., Guagliardo, P., Ulrich, S., 2016a. The golden ark: Arsenopyrite crystal plasticity and the retention of gold through high strain and metamorphism. Terra Nova 28 (3), 181–187. https://doi.org/10.1111/ter.12206.

Fougerouse, D., Micklethwaite, S., Tomkins, A.G., Mei, Y., Kilburn, M., Guagliardo, P., Fisher, L.A., Halfpenny, A., Gee, M., Paterson, D., Howard, D.L., 2016b. Gold remobilisation and formation of high grade ore shoots driven by dissolution-reprecipitation replacement and Ni substitution into auriferous arsenopyrite.

Geochim. Cosmochim. Acta 178, 143–159. https://doi.org/10.1016/j.gca.2016.01.040.
Fougerouse, D., Micklethwaite, S., Ulrich, S., Miller, J., Godel, B., Adams, D.T., McCuaig, T.C., 2017. Evidence for two Stages of Mineralization in West Africa's Largest Gold Deposit: Obuasi, Ghana. Economic Geology 112 (1), 3–22. https://doi.org/10.2113/econgeo.112.1.3.
Fraga, L.M., Reis, N.J., Dall'Agnol, R., Armstrong, R., 2008. Cauarane—Coeroeni Belt—The tectonic southern limit of the preserved Rhyacian crustal domain in the Guyana Shield, northern Amazonian craton. In: International Geological Congress, 33. Oslo, Norway. Abstract, [CD-ROM].
Fraga, L.M., Macambira, M.J.B., Dall'Agnol, R., Costa, J.B.S., 2009. 1.94–1.93 Ga charnockitic magmatism from the central part of the Guyana Shield, Roraima, Brazil: Single-zircon evaporation data and tectonic implications. J. S. Am. Earth Sci. 27 (4), 247–257. https://doi.org/10.1016/j.jsames.2009.02.007.
Fraga, L.M., Cordani, U., Kroonenberg, S., Roever, E.D., Nadeau, S., Maurer, V.C., 2017. U–Pb SHRIMP: new data on the high-grade supracrustal rocks of the Cauarane–Coeroeni Belt – insights on the tectonic Eo-Orosirian evolution of the Guiana Shield. Presented at Simpósio De Geologia Da Amazônia 15, Belém.
Fraga, L.M., Cordani, U., 2019. Early Orosirian tectonic evolution of the Central Guiana Shield: Insights from new U-Pb SHRIMP data. Extended Abstract, in: Proceedings 11th Inter-Guiana Geol. Conf. Feb. 2019, Paramaribo, Suriname, Mededeling Geol. Mijnb. Dienst Suriname, 29, 59–62.
Fraga, L.M., Cordani, U., Maria Dreher, A., Sato, K., Joaquim Reis, N., Nadeau, S., De Roever, E., Kroonenberg, S., Camara Maurer, V., 2024. Early Orosirian belts of the central Guiana Shield, northern amazonian Craton: U-Pb geochronology and tectonic implications. Precambr. Res. 407, 107362. https://doi.org/10.1016/j.precamres.2024.107362.
Frimmel, H.E., 1997. Chlorite Thermometry in the Witwatersrand Basin: Constraints on the Paleoproterozoic Geotherm in the Kaapvaal Craton, South Africa. the Journal of Geology 105 (5), 601–616. https://doi.org/10.1086/515962.
Gapais, D., Alimoenadi, G., Balraadjsing, N., Poupeau, B., 2021. The Rosebel gold mining district (Trans-amazonian belt, Suriname), a new structural framework. BSGF - Earth Sciences Bulletin 192, 32. https://doi.org/10.1051/bsgf/2021021.
Geological Mining Service of Suriname, 1955. Jaarboek 1955 (pp. 15, 23–24).
Gibbs, A.K., Barron, C.N., 1993. The geology of the Guiana Shield. Oxford University Press (Oxford).
Goldfarb, R.J., Groves, D.I., Gardoll, S., 2001. Orogenic gold and geologic time: a global synthesis. Ore Geol. Rev. 18 (1–2), 1–75. https://doi.org/10.1016/S0169-1368(01)00016-6.
Goldfarb, R.J., Groves, D.I., 2015. Orogenic gold: Common or evolving fluid and metal sources through time. Lithos 233, 2–26. https://doi.org/10.1016/j.lithos.2015.07.011.
Goldfarb, R.J., André-Mayer, A.-S., Jowitt, S.M., Mudd, G.M., 2017. West Africa: the World's Premier Paleoproterozoic Gold Province. Econ. Geol. 112 (1), 123–143. https://doi.org/10.2113/econgeo.112.1.123.
Grenholm, M., Jessell, M., Thébaud, N., 2019. A geodynamic model for the Paleoproterozoic (ca. 2.27–1.96 Ga) Birimian Orogen of the southern West African Craton – Insights into an evolving accretionary-collisional orogenic system. Earth Sci. Rev. 192, 138–193. https://doi.org/10.1016/j.earscirev.2019.02.006.
Grosch, E.G., 2019. Metamorphic processes preserved in early Archean supracrustal rocks of the Barberton Greenstone Belt, South Africa. Geol. Soc. Lond. Spec. Publ. 478 (1), 315–334. https://doi.org/10.1144/SP478.15.
Groves, D.I., Goldfarb, R.J., Gebre-Mariam, M., Hagemann, S.G., Robert, F., 1998. Orogenic gold deposits: a proposed classification in the context of their crustal distribution and relationship to other gold deposit types. Ore Geol. Rev. 13 (1–5), 7–27. https://doi.org/10.1016/S0169-1368(97)00012-7.
Guiraud, J., Tremblay, A., Jébrak, M., Ross, P.-S., Lefrançois, R., 2020. Stratigraphic setting and timing of the Montagne d'Or deposit, a unique Rhyacian Au-rich VMS deposit of the Guiana Shield, French Guiana. Precambrian Research 337, 105551. https://doi.org/10.1016/j.precamres.2019.105551.
Hagemann, S.G., Cassidy, K.F., 2000. Archean Orogenic Lode Gold Deposits. SEG Reviews 13, 9–68.
Hastie, E.C.G., Kontak, D.J., Lafrance, B., Petrus, J.A., Sharpe, R., Fayek, M., 2023. Evaluating Geochemical Discriminants in Archean Gold deposits: a Superior Province Perspective with an Emphasis on the Abitibi Greenstone Belt. Econ. Geol. 118 (1), 123–155. https://doi.org/10.5382/econgeo.4979.
Henry, D.G., Jarvis, I., Gillmore, G., Stephenson, M., 2019. Raman spectroscopy as a tool to determine the thermal maturity of organic matter: Application to sedimentary, metamorphic and structural geology. Earth Sci. Rev. 198, 102936. https://doi.org/10.1016/j.earscirev.2019.102936.
Hu, X., Ding, Z., Gong, Y., Li, K., He, M., 2022. Sediment-hosted disseminated gold deposits in orogenic belts: an example from the giant Jiagantan gold deposit in the West Qinling orogeny, China. Ore Geology Reviews 146, 104950. https://doi.org/10.1016/j.oregeorev.2022.104950.
Iamgold Corporation. (2017). Technical Report NI43-101 on the Rosebel Gold Mine.
Iamgold Corporation. (2022). Technical Report on the Rosebel Gold Mine (p. 444).
Inoue, A., Meunier, A., Patrier-Mas, P., Rigault, C., Beaufort, D., Vieillard, P., 2009. Application of chemical geothermometry to low-temperature trioctahedral chlorites. Clay Clay Miner. 57 (3), 371–382. https://doi.org/10.1346/CCMN.2009.0570309.
Johansson, Å., 2009. Baltica, Amazonia and the SAMBA connection—1000 million years of neighbourhood during the Proterozoic? Precambr. Res. 175 (1–4), 221–234. https://doi.org/10.1016/j.precamres.2009.09.011.
Kaneki, S., Hirono, T., 2019. Diagenetic and shear-induced transitions of frictional strength of carbon-bearing faults and their implications for earthquake rupture dynamics in subduction zones. Sci. Rep. 9 (1), 7884. https://doi.org/10.1038/s41598-019-44307-y.
Kioe-A-Sen, N.M.E., Van Bergen, M.J., Wong, T.E., Kroonenberg, S.B., 2016. Gold deposits of Suriname: Geological context, production and economic significance. Netherlands Journal of Geosciences - Geologie En Mijnbouw 95 (4), 429–445. https://doi.org/10.1017/njg.2016.40.
Klaver, M., De Roever, E.W.F., Nanne, J.A.M., Mason, P.R.D., Davies, G.R., 2015a. Charnockites and UHT metamorphism in the Bakhuis Granulite Belt, western Suriname: evidence for two separate UHT events. Precambr. Res. 262, 1–19. https://doi.org/10.1016/j.precamres.2015.02.014.
Klaver, M., De Roever, E.W.F., Thijssen, A.C.D., Bleeker, W., Söderlund, U., Chamberlain, K., Ernst, R., Berndt, J., Zeh, A., 2015b. Mafic magmatism in the Bakhuis Granulite Belt (western Suriname): Relationship with charnockite magmatism and UHT metamorphism. GFF 138 (1), 203–218. https://doi.org/10.1080/11035897.2015.1061591.
Klein, E.L., Koppe, J.C., 2000. Chlorite geothermometry and physicochemical conditions of gold mineralization in the Paleoproterozoic Caxias deposit, São Luis Craton, Northern Brazil. Geochimica Brasiliensis 14 (2), 219–232.
Klein, E.L., Harris, C., Giret, A., Moura, C.A.V., 2007. The Cipoeiro gold deposit, Gurupi Belt, Brazil: Geology, chlorite geochemistry, and stable isotope study. J. S. Am. Earth Sci. 23 (2–3), 242–255. https://doi.org/10.1016/j.jsames.2006.09.002.
Kouketsu, Y., Tsai, C.-H., Enami, M., 2019. Discovery of unusual metamorphic temperatures in the Yuli belt, eastern Taiwan: New interpretation of data by Raman carbonaceous material geothermometry. Geology 47 (6), 522–526. https://doi.org/10.1130/G45934.1.
Kranidiotis, P., MacLean, W.H., 1987. Systematics of chlorite alteration at the Phelps Dodge massive sulfide deposit, Matagami, Quebec. Economic Geology 82 (7), 1898–1911. https://doi.org/10.2113/gsecongeo.82.7.1898.
Kroonenberg, S.B., De Roever, E.W.F., Fraga, L.M., Reis, N.J., Faraco, T., Lafon, J.-M., Cordani, U., Wong, T.E., 2016. Paleoproterozoic evolution of the Guiana Shield in Suriname: a revised model. Netherlands Journal of Geosciences - Geologie En Mijnbouw 95 (4), 491–522. https://doi.org/10.1017/njg.2016.10.
Lacroix, B., Lahondes, D., Hainque, P.-J., Le Goff, E., Fournier, D., Hauteville, A., Gourcerol, B., Eglinger, A., Andre-Mayer, A.-S., 2024. Gold concentration during polyphase deformation: Insights from Boulanger Project, French Guiana. J. S. Am. Earth Sci. 146, 105074. https://doi.org/10.1016/j.jsames.2024.105074.
Lafrance, J., Bardoux, M., Voicu, G., Stevenson, R., Machao, N., 1999. Geological and metallogenic environments of gold deposits of the Guiana Shield. a comparative study between St-Elie (French Guiana) and Omai (Guyana). Explor. Min. Geol. 8 (1–2), 117–135.
Lanari, P., Wagner, T., Vidal, O., 2014. A thermodynamic model for di-trioctahedral chlorite from experimental and natural data in the system MgO–FeO–Al2O3–SiO2–H2O: applications to P–T sections and geothermometry. Contrib. Miner. Petrol. 167, 968–987.
Lawley, C.J.M., Schneider, D.A., Camacho, A., McFarlane, C.R.M., Davis, W.J., Yang, X.-M., 2023. Post-orogenic exhumation triggers gold mineralization in the Trans-Hudson orogen: New geochronology results from the Lynn Lake greenstone belt, Manitoba, Canada. Precambrian Research 395, 107127. https://doi.org/10.1016/j.precamres.2023.107127.
Ledru, P., Pons, J., Milesi, J.P., Feybesse, J.L., Johan, V., 1991. Transcurrent tectonics and polycyclic evolution in the lower proterozoic of Senegal-Mali. Precambr. Res. 50 (3–4), 337–354. https://doi.org/10.1016/0301-9268(91)90028-9.
Ledru, P., Johan, V., Milési, J.P., Tegyey, M., 1994. Markers of the last stages of the Palaeoproterozoic collision: evidence for a 2 Ga continent involving circum-South Atlantic provinces. Precambr. Res. 69 (1–4), 169–191. https://doi.org/10.1016/0301-9268(94)90085-X.
Lünsdorf, N.K., Dunkl, I., Schmidt, B.C., Rantitsch, G., Von Eynatten, H., 2017. Towards a Higher Comparability of Geothermometric Data Obtained by Raman Spectroscopy of Carbonaceous Material. Part 2: a revised Geothermometer. Geostand. Geoanal. Res. 41 (4), 593–612. https://doi.org/10.1111/ggr.12178.
Luque, F.J., Pasteris, J.D., Wopenka, B., Rodas, M., 1998. Natural fluid-deposited graphite: mineralogical characteristics and mechanisms of formation. Am. J. Sci. 298, 471–498.
Marcoux, E., Milési, J.P., 1993. Lead Isotope Signature of Early Proterozoic Ore Deposits in Western Africa: Comparison with Gold Deposits in French Guiana. Econ. Geol. 88, 1862–1879.
Mason, P. R. D., Van Bergen, M. J., Kriegsman, L. M., & Kroonenberg, S. B. (2022). Age constraints on Early Proterozoic sedimentation during Transamazonian continental convergence in Suriname. Extended Abstract Presented at SAXI - XII InterGuiana Geological Conference, Georgetown, Guyana, 111–112.
Masurel, Q., Eglinger, A., Thébaud, N., Allibone, A., André-Mayer, A.-S., McFarlane, H., Miller, J., Jessell, M., Aillères, L., Vanderhaeghe, O., Salvi, S., Baratoux, L., Perrouty, S., Begg, G., Fougerouse, D., Hayman, P., Wane, O., Tshibubudze, A., Parra-Avila, L., Amponsah, P.O., 2022. Paleoproterozoic gold events in the southern West African Craton: Review and synopsis. Miner. Deposita 57 (4), 513–537. https://doi.org/10.1007/s00126-021-01052-5.
McAleer, R.J., Bish, D.L., Kunk, M.J., Sicard, K.R., Valley, P.M., Walsh, G.J., Wathen, B. A., Wintsch, R.P., 2017. Reaction softening by dissolution–precipitation creep in a retrograde greenschist facies ductile shear zone, New Hampshire, USA. J. Metam. Geol. 35 (1), 95–119. https://doi.org/10.1111/jmg.12222.
Mezger, K., Krogstad, E.J., 1997. Interpretation of discordant U-Pb zircon ages: an evaluation. J. Metam. Geol. 15 (1), 127–140. https://doi.org/10.1111/j.1525-1314.1997.00008.x.
Milési, J.-P., Ledru, P., Feybesse, J.-L., Dommanget, A., Marcoux, E., 1992. Early proterozoic ore deposits and tectonics of the Birimian orogenic belt, West Africa. Precambrian Research 58 (1–4), 305–344. https://doi.org/10.1016/0301-9268(92)90123-6.

Milési, J.-P., Egal, E., Ledru, P., Vernhet, Y., Thiéblemont, D., Cocherie, A., Tegyey, M., Martel-Jantin, B., Lagny, P., 1995. Les minéralisations du Nord de la Guyane française dans leur cadre géologique. Chronicle of Mineral Research & Exploration 5–58.

Milési, J.-P., Lerouge, C., Delor, C., Ledru, P., Lahondère, D., Lasserre, J.-L., Marot, A., Martel-Jantin, B., Rossi, P., Tegyey, M., Théveniaut, H., Thiéblemont, D., Vanderhaeghe, O., 2003. Gold deposits (gold-bearing tourmalinites, gold-bearing conglomerates, and mesothermal lodes), markers of the geological evolution of French Guiana: Geology, metallogeny, and stable-isotope constraints. Géologie De La France 2–3–4, 257–290.

Mori, Y., Shigeno, M., Miyazaki, K., Nishiyama, T., 2019. Peak metamorphic temperature of the Nishisonogi unit of the Nagasaki Metamorphic Rocks, western Kyushu, Japan. J. Mineral. Petrol. Sci. 114 (4), 170–177. https://doi.org/10.2465/jmps.190423.

Mumin, A.H., Fleet, M.E., Chryssoulis, S.L., 1994. Gold mineralization in As-rich mesothermal gold ores of the Bogosu-Prestea mining district of the Ashanti Gold Belt, Ghana: Remobilization of 'invisible' gold. Miner. Deposita 29, 445–460.

Naipal, R., Kroonenberg, S.B., 2016. Provenance signals in metaturbidites of the Paleoproterozoic greenstone belt of the Guiana Shield in Suriname. Netherlands Journal of Geosciences - Geologie En Mijnbouw 95 (4), 467–489. https://doi.org/10.1017/njg.2016.9.

Nakamura, Y., Oohashi, K., Toyoshima, T., Satish-Kumar, M., Akai, J., 2015. Strain-induced amorphization of graphite in fault zones of the Hidaka metamorphic belt, Hokkaido, Japan. J. Struct. Geol. 72, 142–161. https://doi.org/10.1016/j.jsg.2014.10.012.

Nanne, J.A.M., De Roever, E.W.F., De Groot, K., Davies, G.R., Brouwer, F.M., 2020. Regional UHT metamorphism with widespread, primary CO2-rich cordierite in the Bakhuis Granulite Belt, Surinam: a feldspar thermometry study. Precambr. Res. 350, 105894. https://doi.org/10.1016/j.precamres.2020.105894.

Neves, B.B.D.B., 2011. The Paleoproterozoic in the South-American continent: Diversity in the geologic time. J. S. Am. Earth Sci. 32 (4), 270–286. https://doi.org/10.1016/j.jsames.2011.02.004.

Newmont. (2024). Newmont Press release. https://www.newmont.com/investors/news-release/news-details/2024/Newmont-Announces-2023-Mineral-Reserves-for-Integrated-Company-of-136-Million-Gold-Ounces-with-Robust-Copper-Optionality-of-30-Billion-Pounds/default.aspx.

Nishimura, Y., Coombs, D.S., Landis, C.A., Itaya, T., 2000. Continuous metamorphic gradient documented by graphitization and K-Ar age, southeast Otago, New Zealand. American Mineralogist 85 (11–12), 1625–1636. https://doi.org/10.2138/am-2000-11-1206.

Nomade, S., Théveniaut, H., Chen, Y., Pouclet, A., Rigollet, C., 2000. Paleomagnetic study of French Guyana Early Jurassic dolerites: Hypothesis of a multistage magmatic event. Earth Planet. Sci. Lett. 184 (1), 155–168. https://doi.org/10.1016/S0012-821X(00)00305-8.

Nomade, S., Pouclet, A., Chen, Y., 2002. The French Guyana doleritic dykes: Geochemical evidence of three populations and new data for the Jurassic Central Atlantic Magmatic Province. J. Geodyn. 34 (5), 595–614. https://doi.org/10.1016/S0264-3707(02)00034-0.

Nomade, S., Chen, Y., Pouclet, A., Féraud, G., Théveniaut, H., Daouda, B.Y., Vidal, M., Rigolet, C., 2003. The Guiana and the West African Shield Palaeoproterozoic grouping: New palaeomagnetic data for French Guiana and the Ivory Coast. Geophys. J. Int. 154 (3), 677–694. https://doi.org/10.1046/j.1365-246X.2003.01972.x.

Norcross, C., Davis, D.W., Spooner, E.T.C., Rust, A., 2000. U-Pb and Pb-Pb age constraints on Paleoproterozoic magmatism, deformation and gold mineralization in the Omai area, Guyana Shield. Precambrian Research 102 (1–2), 69–86. https://doi.org/10.1016/S0301-9268(99)00102-3.

Oberthür, T., Weiser, T., Amanor, J.A., Chryssoulis, S.L., 1997. Mineralogical siting and distribution of gold in quartz veins and sulfide ores of the Ashanti mine and other deposits in the Ashanti belt of Ghana: Genetic implications. Miner. Deposita 32 (1), 2–15. https://doi.org/10.1007/s001260050068.

Oliver, N. H. S., Thomson, B., Freitas-Silva, F. H., & Holcombe, R. J. (2020). Chapter 5: The Low-Grade, Neoproterozoic, Vein-Style, Carbonaceous Phyllite-Hosted Paracatu Gold Deposit, Minas Gerais, Brazil. In R. H. Sillitoe, R. J. Goldfarb, F. Robert, & S. F. Simmons (Eds.), Geology of the World's Major Gold Deposits and Provinces (pp. 101–120). Society of Economic Geologists. doi:10.5382/SP.23.05.

Oohashi, K., Hirose, T., Shimamoto, T., 2013. Graphite as a lubricating agent in fault zones: an insight from low- to high-velocity friction experiments on a mixed graphite-quartz gouge. J. Geophys. Res. Solid Earth 118 (5), 2067–2084. https://doi.org/10.1002/jgrb.50175.

Padoan, M., Rossetti, P., Rubatto, D., 2014. The Choco 10 gold deposit (El Callao, Bolivar State, Venezuela): Petrography, geochemistry and U–Pb geochronology. Precambr. Res. 252, 22–38. https://doi.org/10.1016/j.precamres.2014.06.024.

Pant, S., Singh, S., Sahoo, P.R., Kumar, A., Saravanan, B., Venkatesh, A.S., Yadav, G.S., Kumar, P., 2019. Mineral chemistry and geothermometry of chlorites in relation to physico-chemical conditions of uranium mineralization in the central part of the Singhbhum Shear Zone, eastern India. Ore Geol. Rev. 112, 102997. https://doi.org/10.1016/j.oregeorev.2019.102997.

Pérez-Cáceres, I., Martínez Poyatos, D.J., Vidal, O., Beyssac, O., Nieto, F., Simancas, J.F., Azor, A., Bourdelle, F., 2020. Deciphering the metamorphic evolution of the Pulo do Lobo metasedimentary domain (SW Iberian Variscides). Solid Earth 11 (2), 469–488. https://doi.org/10.5194/se-11-469-2020.

Perrouty, S., Aillères, L., Jessell, M.W., Baratoux, L., Bourassa, Y., Crawford, B., 2012. Revised Eburnean geodynamic evolution of the gold-rich southern Ashanti Belt, Ghana, with new field and geophysical evidence of pre-Tarkwaian deformations. Precambr. Res. 204–205, 12–39. https://doi.org/10.1016/j.precamres.2012.01.003.

Peucat, J.J., Tisserant, D., Caby, R., Clauer, N., 1985. Resistance of zircons to U-Pb resetting in a prograde metamorphic sequence of Caledonian age in East Greenland. Can. J. Earth Sci. 22, 330–338.

Pidgeon, R.T., O'Neil, J.R., Silver, L.T., 1966. Uranium and Lead Isotopic Stability in a Metamict Zircon under Experimental Hydrothermal Conditions. Science 154 (3756), 1538–1540. https://doi.org/10.1126/science.154.3756.1538.

Plunder, A., Aergeerts, G., Suire, H., Lahfid, A., Heuret, A., & Casanova, A. (2022). Tectono-metamorphic framework of the Rosebel and Armina unit, French Guiana. Extended Abstract Presented at SAXI - XII InterGuiana Geological Conference, Georgetown, Guyana, 123–127.

Raffle, K., Lefrançois, R., 2022. Technical Report – Antino Project; Suriname, South America.

Rawat, R., Sharma, R., 2011. Features and characterization of graphite in Almora Crystallines and their implication for the graphite formation in Lesser Himalaya, India. Journal of Asian Earth Sciences 42 (1–2), 51–64. https://doi.org/10.1016/j.jseaes.2011.03.015.

Reis, N.J., Teixeira, W., D'Agrella-Filho, M.S., Bettencourt, J.S., Ernst, R.E., Goulart, L.E.A., 2021. Large igneous provinces of the amazonian Craton and their metallogenic potential in Proterozoic times. Geol. Soc. Lond. Spec. Publ. 518 (1), 493–529. https://doi.org/10.1144/SP518-2021-7.

Ribeiro, J. W. A., Schmidt, K., Radjkoemar, S., & Anderson, S. (2009). Orogenic Gold Deposits of the Merian Trend Suriname, South America. Extended Abstract Presented at 6th International Congress of Prospectors and Explorers-Proexplo 2009, 1–9.

Robert, F., Poulsen, K. H., Cassidy, K. F., & Hodgson, C. J. (2005). Gold Metallogeny of the Superior and Yilgarn Cratons. *Economic Geology*, *100th Anniversary Volume*, 1001–1033.

Roy, N., Roy, A., Saha, P., Mandal, N., 2022. On the origin of shear-band network patterns in ductile shear zones. Proceedings of the Royal Society a: Mathematical, Physical and Engineering Sciences 478 (2264), 20220146. https://doi.org/10.1098/rspa.2022.0146.

Santos, J.O.S., Potter, P.E., Reis, N.J., Hartmann, L.A., Fletcher, I.R., McNaughton, N.J., 2003. Age, source, and regional stratigraphy of the Roraima Supergroup and Roraimalike outliers in northern South America based on U-Pb geochronology. GSA Bull. 115 (3), 331–348.

Soares, G.A.R., Lobato, L.M., Lucena, R.A., Lana, C.C., 2025. Geologic setting and Hydrothermal Alteration at the Tucano Gold Deposit in Northern Brazil: evidence for a Hypozonal Orogenic Gold System in the Guiana Shield. Econ. Geol. 120 (2), 275–306.

Steffen, K.J., Selverstone, J., 2006. Retrieval of P–T information from shear zones: Thermobarometric consequences of changes in plagioclase deformation mechanisms. Contrib. Miner. Petrol. 151 (5), 600–614. https://doi.org/10.1007/s00410-006-0073-8.

Stipp, M., Stünitz, H., Heilbronner, R., Schmid, S.M., 2002. The eastern Tonale fault zone: a 'natural laboratory' for crystal plastic deformation of quartz over a temperature range from 250 to 700°C. J. Struct. Geol. 24 (12), 1861–1884. https://doi.org/10.1016/S0191-8141(02)00035-4.

Sun, S., & McDonough, W. F. (1989). Chemical and isotopic systematics of oceanic basalts: Implications for mantle composition and processes. Magmatism in the ocean basins (pp. 313–345).

Tedeschi, M., Hagemann, S.G., Davis, J., 2018a. The Karouni Gold Deposit, Guyana, South America: Part I. Stratigraphic setting and Structural Controls on Mineralization. Econ. Geol. 113 (8), 1679–1704. https://doi.org/10.5382/econgeo.2018.4609.

Tedeschi, M., Hagemann, S.G., Roberts, M.P., Evans, N.J., 2018b. The Karouni Gold Deposit, Guyana, South America: Part II. Hydrothermal Alteration and Mineralization. Economic Geology 113 (8), 1705–1732. https://doi.org/10.5382/econgeo.2018.4610.

Tedeschi, M.T., Hagemann, S.G., Kemp, A.I.S., Kirkland, C.L., Ireland, T.R., 2020. Geochronological constrains on the timing of magmatism, deformation and mineralization at the Karouni orogenic gold deposit: Guyana, South America. Precambrian Research 337, 105329. https://doi.org/10.1016/j.precamres.2019.04.015.

Thébaud, N., Allibone, A., Masurel, Q., Eglinger, A., Davis, J., André-Mayer, A.-S., Miller, J., François Ouedrago, M., & Jessell, M. (2020). Chapter 34: The Paleoproterozoic (Rhyacian) Gold Deposits of West Africa. In R. H. Sillitoe, R. J. Goldfarb, F. Robert, & S. F. Simmons (Eds.), Geology of the World's Major Gold Deposits and Provinces (pp. 735–752). Society of Economic Geologists. doi:10.5382/SP.23.34.

Van den Boorn, S.H.J.M., Van Bergen, M.J., Nijman, W., Vroon, P.Z., 2007. Dual role of seawater and hydrothermal fluids in Early Archean chert formation: evidence from silicon isotopes. Geology 35 (10), 939. https://doi.org/10.1130/G24096A.1.

Van Hinsberg, V., Berlo, K., Van Bergen, M., Williams-Jones, A., 2010. Extreme alteration by hyperacidic brines at Kawah Ijen volcano, East Java, Indonesia: I. Textural and mineralogical imprint. J. Volcanol. Geoth. Res. 198 (1–2), 253–263. https://doi.org/10.1016/j.jvolgeores.2010.09.002.

Van Hinsbergen, D.J.J., Lamont, T.N., Guilmette, C., 2025. Lithospheric Unzipping explaining Hot Orogenesis during Continental Subduction. Tectonics 44 (7), e2025TC008993. https://doi.org/10.1029/2025TC008993.

Van Maastrigt, P. J. M. (2009a). Report on the mapping of the Charlemagne hill and surroundings. IAMGOLD Corporation, Suriname.

Van Maastrigt, P. J. M. (2009b). Annual Report, Suriname, 2008 Charmagne and Left concessions.

Vanderhaeghe, O., Ledru, P., Thieblemont, D., Egal, E., Cocherie, A., Tegyey, M., Milesi, J.-P., 1998. Contrasting mechanism of crustal growth Geodynamic evolution of the Paleoproterozoic granite–greenstone belts of French Guiana. Precambr. Res. 92, 165–193.

Velásquez, G., Béziat, D., Salvi, S., Tosiani, T., Debat, P., 2011. First occurrence of Paleoproterozoic oceanic plateau in the Guiana Shield: the gold-bearing El Callao Formation, Venezuela. Precambrian Research 186 (1–4), 181–192. https://doi.org/10.1016/j.precamres.2011.01.016.

Velásquez, G., Beziat, D., Salvi, S., Siebenaller, L., Borisova, A.Y., Pokrovski, G.S., De Parseval, P., 2014. Formation and Deformation of Pyrite and Implications for Gold Mineralization in the El Callao District. Venezuela. Economic Geology 109 (2), 457–486. https://doi.org/10.2113/econgeo.109.2.457.

Velásquez, G., Salvi, S., Siebenaller, L., Béziat, D., Carrizo, D., 2018. Control of Shear-Zone-Induced pressure Fluctuations on Gold Endowment: the Giant El Callao District, Guiana Shield. Venezuela. Minerals 8 (10), 430. https://doi.org/10.3390/min8100430.

Voicu, G., Bardoux, M., Jebrak, M., Crepeau, R., 1999. Structural, mineralogical and geochemical studies of the Paleoproterozoic Omai gold deposit. Guyana. Economic Geology 94 (8), 1277–1303. https://doi.org/10.2113/gsecongeo.94.8.1277.

Voicu, G., Bardoux, M., Stevenson, R., 2001. Lithostratigraphy, geochronology and gold metallogeny in the northern Guiana Shield, South America: a review. Ore Geol. Rev. 18 (3–4), 211–236. https://doi.org/10.1016/S0169-1368(01)00030-0.

Von Huene, R., Scholl, D.W., 1991. Observations at convergent margins concerning sediment subduction, subduction erosion, and the growth of continental crust. Rev. Geophys. 29 (3), 279–316. https://doi.org/10.1029/91RG00969.

Wallis, D., Lloyd, G.E., Phillips, R.J., Parsons, A.J., Walshaw, R.D., 2015. Low effective fault strength due to frictional-viscous flow in phyllonites, Karakoram Fault Zone, NW India. J. Struct. Geol. 77, 45–61. https://doi.org/10.1016/j.jsg.2015.05.010.

Watson, T., 2008. Volcanism and Sedimentation: New Insight into Arc-Related Volcanism and Sediment Deposition in a Synkinematic Paleoproterozoic Basin: Rosebel Gold Mine. University of North Carolina at Chapel Hill. Northeastern Suriname [MSc thesis].

Wopenka, B., Pasteris, J.D., 1993. Structural characterization of kerogens to granulite-facies graphite: Applicability of Raman microprobe spectroscopy. Am. Mineral. 78 (5–6), 553–557.

Yavuz, F., Kumral, M., Karakaya, N., Karakaya, M.Ç., Yıldırım, D.K., 2015. A Windows program for chlorite calculation and classification. Comput. Geosci. 81, 101–113. https://doi.org/10.1016/j.cageo.2015.04.011.

Yui, T.-F., Huang, E., Xu, J., 1996. Raman spectrum of carbonaceous material: a possible metamorphic grade indicator for low-grade metamorphic rocks. J. Metam. Geol. 14 (2), 115–124. https://doi.org/10.1046/j.1525-1314.1996.05792.x.